Federal University of ABC
Center of Natural Sciences and Humanities
Graduate Program in Nanoscience and Advanced Materials

Hollow magnetic and semiconductor micro/nanostructures: synthesis, physical properties and application

César Augusto Díaz Pomar

Santo André, 2018

Federal University of ABC
Center of Natural Sciences and Humanities
Graduate Program in Nanoscience and Advanced Materials

Hollow magnetic and semiconductor micro/nanostructures: synthesis, physical properties and application

César Augusto Díaz Pomar

Thesis presented to the Nanosciences and Advanced Materials
Graduate Program of the Federal University of
ABC as partial requirement to obtain the title of Doctor
of Nanosciences and Advanced Materials
under the supervision of Prof. Dr. José Antonio Souza

Santo André, 2018

Sistema de Bibliotecas da Universidade Federal do ABC
Elaborada pelo Sistema de Geração de Ficha Catalográfica da UFABC
com os dados fornecidos pelo(a) autor(a).

Díaz Pomar, César Augusto
Hollow magnetic and semiconductor micro/nanostructures : synthesis, physical properties and application / César Augusto Díaz Pomar. — 2018.

79 fls. : il.

Orientador: José Antonio Souza

Tese (Doutorado) — Universidade Federal do ABC, Programa de Pós Graduação em Nanociências e Materiais Avançados, Santo André, 2018.

1. Nanoscience. 2. Nanotechnology. 3. Nanomagnetism. 4. Semiconductors. 5. Photodegradation. I. Souza, José Antonio. II. Programa de Pós-Graduação em Nanociências e Materiais Avançados, 2018. III. Título.

Este exemplar foi revisado e alterado em relação à versão original, de acordo com as observações levantadas pela banca no dia da defesa, sob responsabilidade única do autor e com a anuência de seu orientador.

Santo André, 29 de Junho de 2018

Assinatura do autor: _____

Assinatura do orientador: _____

MINISTÉRIO DA EDUCAÇÃO
Fundação Universidade Federal do ABC
Programa de Pós-Graduação em Nanociências e Materiais Avançados
Avenida dos Estados, 5001 – Bairro Santa Terezinha – Santo André – SP
CEP 09210-580 – Fone: (11) 4996-0017
ppg.nanomat@ufabc.edu.br

FOLHA DE ASSINATURAS

Assinaturas dos membros da Banca Examinadora que avaliou e aprovou a Defesa de Tese de Doutorado do candidato César Augusto Díaz Pomar, realizada em 29 de maio de 2018:

Prof.(a) Dr.(a) **Jose Antonio Souza** (Universidade Federal do ABC) – Presidente

Prof.(a) Dr.(a) **Jeroen Schoenmaker** (Universidade Federal do ABC) – Membro Titular

Prof.(a) Dr.(a) **André Sarto Polo** (Universidade Federal do ABC) – Membro Titular

Remoto

Prof.(a) Dr.(a) **Valdeci Pereira Mariano de Souza** (Universidade Estadual Paulista Júlio de Mesquita Filho) – Membro Titular

Remoto

Prof.(a) Dr.(a) **Marcio Peron Franco de Godoy** (Universidade Federal de São Carlos) – Membro Titular

Prof.(a) Dr.(a) **Márcia Tsuyama Escote** (Universidade Federal do ABC) – Membro Suplente

Prof.(a) Dr.(a) **Thiago Branquinho de Queiroz** (Universidade Federal do ABC) – Membro Suplente

Prof.(a) Dr.(a) **Fabio Coral Fonseca** (Instituto de Pesquisas Energéticas e Nucleares) – Membro Suplente

Prof.(a) Dr.(a) **Reginaldo Muccillo** (Instituto de Pesquisas Energéticas e Nucleares) – Membro Suplente

Dedicatory

To my parents *Floremia* and *Pedro* who did everything possible to see their youngest son as a Doctor.

To my brothers *Pierre* and *Angélica* for all the teachings, support and love.

To *Fernanda*, for being the light that guides my life.

Acknowledgements

I would like to express my heartfelt gratitude to Dr. Jose Antonio Souza for guiding and supporting me all these years, and for his outstanding patience and advises.

I wish to thank to my PeNSeM laboratory partners (Cynthia, Guilherme, Helder, Adriane, Vinicius) for all our successful work together.

My grateful thanks are extended to Professor Fabio Furlan, Professor Flavio Leandro Souza, Professor Sydney Ferreira Santos, Dra. Fanny Costa, and Dra Aryane Tofanello for the help with the experimental measurements in the collaboration works.

I also would like to express my grateful to the Multiuser Central Facilities (UFABC) and to the Professor Herculano da Silva Martinho and their team for the experimental support.

Financial support is gratefully acknowledged from the CAPES agency and the UFABC scholarship.

“I, a universe of atoms, an atom in the universe”

Richard Feynman

“*Tudo o que eu fiz não vale uma sinfonia de Mozart*.”

César Lattes

“Una educación que integre las ciencias y las artes a la canasta familiar, de acuerdo con los designios de un gran poeta de nuestro tiempo que pidió no seguir amándolas por separado como a dos hermanas enemigas. Que canalice hacia la vida la inmensa energía creadora que durante siglos hemos despilfarrado en la depredación y la violencia, y nos abra al fin la segunda oportunidad sobre la tierra que no tuvo la estirpe desgraciada del coronel Aureliano Buendía.”

Gabriel García Marquez

Abstract

The aim of this work is to synthesize hierarchically micro/nanostructured hollow magnetic and semiconductor materials, to obtain a better understanding on the physical properties, and find technological applications. Initially, hematite and magnetite microtubes were synthesized by thermal oxidation process along with the presence of an applied electrical current and using metallic iron microwire as a precursor. The volume fraction of both Fe_2O_3 (hematite) and Fe_3O_4 (magnetite) phase on microtubes can be controlled as well as surface nanostructures formation of hematite by systematic change of the synthesis parameters such as temperature, heating rate, annealing time and electrical current value. The oxidation chemical reaction involves a process where a thin oxide layer is formed first on the metal surface, followed by simultaneous outward diffusion of metal ions through the oxide scale and inward diffusion of oxygen from the atmosphere into the core. In our case, the outward diffusion is faster leading to the creation of vacancies which coalesce into voids forming the microtubes. *In situ* electrical resistivity measurements were carried out during the oxidation process showing the whole process of the microtube formation. Scanning electron microscopy images show microtube morphology with diameter ranging from 40 μm to 100 μm and length of 5 mm. X-ray powder diffraction measurements evidence the presence of hematite (Fe_2O_3) and magnetite (Fe_3O_4) crystal phases comprising microtubes. Nanostructures of hematite appear in form of sticks and wires homogeneously dispersed on the microtube surface with diameters ranking from 80 nm to 300 nm and length of 1 to 5 μm. *In vitro* experiments involving adherence, migration, and proliferation of fibroblasts cell culture on the surface of the microtubes indicated the absence of immediate cytotoxicity for this material. We have also calculated both torque and driving magnetic force for these microtubes with nanowires as a function of external magnetic field gradient which were found to be robust opening the possibility for magnetic bio micro-robot device fabrication and application in biotechnology.

On the other hand, SnS and ZnS hollow microarchitectures decorated with nanostructures were synthesized by catalysis free thermal evaporation technique using metal microwires and sulfur powder as starting materials. For SnS, we observed a hollow formation comprised of a thin metallic Sn layer in the inner surface, SnS orthorhombic structure thick layer with SnS nanostructures on the top. For ZnS, we found out the formation of hollow sphere with a thin metallic layer in the inner part, a thick cubic phase layer of ZnS, and on this second phase, nanostructures of ZnS hexagonal crystal phase grew up homogeneously. The microsphere diameter is about 415 μm and the nanowires on the surface have average diameter of 70 nm and length 7 μm. ZnS and SnS hollow semiconducting microstructures

have exhibited efficient activity to degrade the methylene blue under simulated sunlight irradiation. The results reveal that these nano/microstructures have high photoactivity to organic degradation.

Keywords: Magnetic microtubes, nanowires, magnetic actuation, micro/nano chalcogenides, dye photodegradation.

Resumo

O objetivo deste trabalho é sintetizar materiais magnéticos e semicondutores ocos micro/nanoestruturados hierarquicamente, para obter um melhor entendimento das propriedades físicas e explorar aplicações tecnológicas. Inicialmente, microtubos de hematita e magnetita foram sintetizados por oxidação térmica juntamente com uma corrente elétrica aplicada e utilizando-se o microfio de ferro metálico como precursor. A fracção volumetrica de Fe_2O_3(hematite) e Fe_3O_4(magnetite) nos microtubos e a formação das nanoestruturas de hematite na superfície pode ser controlada por alterações sistemáticas dos parâmetros de síntese tais como temperatura, rampa de aquecimento, tempo de aquecimento e valor da corrente eléctrica. A reação química de oxidação envolve um processo onde uma fina camada de óxido é formada primeiro na superfície do metal, seguida por difusão simultânea de íons metálicos através da camada oxida e difusão de oxigênio da atmosfera para o interior. A difusão para fora é mais rápida, levando à criação de vacâncias que coalescem em poros formando os microtubos. Medidas de resistividade elétrica *in situ* foram realizadas durante o processo de oxidação mostrando todo o processo de formação do microtubo. Imagens de microscopia eletrônica de varredura mostram a morfologia do microtubo com diâmetro variando de 40 μm a 100 μm e comprimento de 5 mm. Medidas de difração de raios-X em pó evidenciam a presença de fases cristalinas de hematita (Fe_2O_3) e magnetita (Fe_3O_4) nos microtubos. Nanoestruturas de hematita aparecem em forma de bastões e fios dispersos homogeneamente ao redor da superfície do microtubo com diâmetros de 80-300 nm e comprimento de 1-5 μm. Experimentos *in vitro* envolvendo aderência, migração e proliferação de culturas de células de fibroblastos na superfície dos microtubos indicaram a ausência de citotoxicidade para este material. Também o cálculo do torque e da força magnética desses microtubos com nanofios em função do gradiente de campo magnético externo, mostrou que ele é robusto, abrindo a possibilidade para fabricação de bio-micro-robôs magnéticos para aplicação em biotecnologia. Por outro lado, microarquiteturas ocas de SnS e ZnS decoradas com nanoestruturas foram sintetizadas por evaporação térmica livre de catalisadores utilizando microfios de metal e pó de enxofre como materiais de partida. Para o SnS, observamos formação de uma estrutura oca composta por uma camada metálica de Sn na superfície interna, e uma camada de SnS de estrutura ortorrômbica com nanoestruturas de SnS na superfície. Para o ZnS, descobrimos a formação de uma esfera oca com uma camada metálica na parte interna, uma camada de ZnS com fase cúbica, e sobre ela nanoestruturas de ZnS com fase cristalina hexagonal cresceram homogeneamente. O diâmetro da microsfera é de 415 μm e os nanofios têm um diâmetro e comprimento médio de 70 nm e 7 μm,

respectivamente. As microestruturas ocas semicondutoras de ZnS e SnS exibiram atividade eficiente para degradar azul de metileno sob irradiao com luz solar simulada. Os resultados revelam que essas nano/microestruturas possuem alta fotoatividade para degradação orgânica.

Palavras–chave: Microtubos magnéticos, nanofios, atuação magnética, micro / nano calcogenetos, fotodegradação de corantes

CHAPTER 1: HOLLOW MICRO/NANO STRUCTURES

1.1- Introduction

In recent years, considerable effort has been put forward into the design and fabrication of one-dimensional nanomaterial such as nanorods and micro/nanowires with functional properties [1]. Attempts to obtain nanostructures with a specific size and morphology for expanding the applications are usually reported [2]. Nowadays, the control of micro/nanostructures shape along with the functionalization is a very important topic in current scientific research due to their special size and morphology dependent properties. On the other hand, methods to fabricate hollow micro/nanostructures have called attention because their unique shape, low mass density, higher surface area compared to the bulk counterpart, high porosity, interesting optical and magnetic properties and good strain accommodation [3]. These properties can be used for new applications such as micro/nanocontainers and reactors, energy storage, catalysis, environmental remediation, sensors, filters, coatings, capsule agents for drug delivery, templates for functional architecture composite materials, delivery vehicles and fillers. Furthermore, such a tubular morphology is expected to bring about changes in chemical, physical, and catalytic properties of material and devices. The most popular method to fabricate hollow structures can be recognized as the use of templating, coating or chemical etching [4].

In the last few years, significant effort has been focused on synthesis of Hematite (Fe_2O_3) and Magnetite (Fe_3O_4) micro/nanostructures due to interesting properties such as stability under ambient condition, high resistivity to corrosion, magnetic properties and low toxicity [5]. These characteristics place these two iron oxides as materials with great potential for a wide range of applications in the field of catalysis, gas sensors, electrode materials, magnetic recording media, spintronic, and sensor devices. Recently, many groups have reported synthesis of both magnetite and hematite micro and nanostructures by different routes as catalyzed oxidation, microwave-assisted reflux method, and pyrolysis [6]. However, majority iron oxide nanofabrication methods are complicated, since it requires particular conditions and expensive equipment to create physical and chemical controlled conditions [7]. When thermal oxidation is used as fabrication route some factors appear to be relevant on synthesis process. Among the most important parameters, electrical field is one of them. Extensive studies on the electric field in oxidation were first performed by Fromhold *et al* [8]. Quite frequently, the electric field is not explicitly considered. Instead, "effective ion diffusivity" is used which, however, cannot represent all electric field effects.

Despite of the importance of this area in materials science, herein we focused our work on

the synthesis of microstructures surrounded by nanostructures growing up from pure metal wires by thermal oxidation process under particular conditions. We have done a set of physical properties characterizations of iron oxide (Fe_2O_3, Fe_3O_4) microtubes to gain a better understanding on the underlining growth mechanisms of these structures and potential applications of them. Thus, X-Ray diffraction, scanning electron microscopy, *in situ* electrical resistivity, magnetization, and Raman spectroscopy have been employed in this work. Afterwards, preliminary conclusions on this system are presented and finally we have explored some future applications of the iron oxide microtubes in relation with the use of them in magnetic actuation, cellular growth, and photocatalytic activity.

By the other hand, chalcogenides micro/nanostructured materials have been extensively studied due to their semiconducting, optical, and dielectric properties [9]. Ability to switch, bend, and self-organize, in addition to their inherent infrared transparency brings about interesting applications involving devices fabrication in fields such as photonics, energy conversion, and storage devices [10]. ZnS is a semiconductor with bandgap energy of 3.6 eV at 300 K [11]. It has been used in electroluminescence [12], nonlinear optical devices [13], and as a LED when doped [14]. ZnS has been synthesized as nanobelts, nanorods, nanowires and nanosheets and nanocombs [15,16]. Among various synthesis routes, vapor-phase synthesis is probably the most extensively explored approach to form ZnS nanostructures [17]. SnS is a p-type semiconductor with a bandgap of 1.1-1.8 eV at room temperature, high conductivity (hole mobility = 90 $cm^2\ V^{-1}\ s^{-1}$) and absorption coefficients ($\simeq$104 cm^{-1}) near the fundamental absorption edge [18]. Various researchers have reported synthesis of diverse morphologies of SnS as nanowires [19], nanoribbons [20], nanotubes [21] and nanobelts [22]. The most common pathways to obtain these structures are template-assisted pulsed electrochemical route, hydrothermal synthesis, and solution based synthesis [9]. In the majority of cases, tin chips of pure metal and substrates are used in thermal evaporation process. Normally a catalytic material is used, since it allows nucleation process and subsequent nanostructure growth [23]. Usually, it is assumed that nanostructures formation from chalcogenides follows an epitaxial-like growth associated with three growth modes that may be described as layer-by-layer growth, island growth, and layer-by-layer plus islands [24]. Nanostructures of chalcogenides have been synthesized by means of diverse synthesis techniques, being the hydrothermal [25] and solvothermal [26] methods the most common procedures. Thermal evaporation is widely used to prepare films and nanostructures based on low melting point metal aid by catalytic material (seed). However, it has been rarely reported synthesis of nanostructures sulfur compounds without the presence of seed clusters [27]. Here, we have employed an alternative route to obtain SnS and ZnS micro/nanostructures by thermal evaporation of zinc/tin microwires and sulfur powder. Hollow structures of both SnS (microtube) and ZnS (microsphere) were observed by

scanning electron microscopy (SEM) and X-Ray diffraction reveals cubic and hexagonal crystal structures for ZnS and orthorhombic crystalline phase for SnS coexisting simultaneously with metallic phase. We have observed an efficient organic compound degradation by using these hollow semiconducting microstructures under simulated sunlight irradiation.

This thesis is organized into four chapters. Chapter 1 represents the introduction of hollow micro/nanostructure, their synthesis routes and applications. Also in this chapter, it is presented the semiconducting materials of interest in our work. The next chapter (Chapter 2) includes a review about the characterization techniques employed to study diverse physical properties of the obtained samples. Chapter 3 describes the results and discussion. In there, it is presented the synthesis of magnetic microtubes and micro/nano chalcogenides by a new synthesis route. The morphological, topological, structural, magnetic, electrical, optical characterizations are shown. The application of the magnetic microtubes as model to magnetic bio/micro/nano robot is also investigated. In the following, studies on the application of SnS and ZnS hollow samples synthetized in photodegradation of dye were evaluated. The final chapter 4 concludes our work and highlights the scientific contributions.

1.2- Fabrication routes of hollow micro/nanostructures

By defining a “hollow micro/nanostructure” as a solid structure with void space inside a distinct shell, whose dimensions are in the nanometer or micrometer range, one can find cubes, spheres, tubes, and boxes [28]. These set of unique morphologies are today some of the most studied structures which can be obtained through physical, chemical, and biological routes. It is clear the importance and requirement of strong research on this particular field because the goals on hollow micro/nano architectures are growing up very fast nowadays. Among different approaches, the commonly used synthesis for hollow structures is the template directed method that can be grouped into three major categories: hard templating, soft templating, and self-templating synthesis [29].

Hard templates with specific shapes have been synthesized followed by coating the outer surface of a sample with a layer of desired materials [30]. The core materials are then selectively removed to obtain the hollow structure. To achieve a successful coating on the surface of template, a surface modification to change the surface functionality, such as surface charge and polarity, is usually applied. There are some templates normally used. For example, polymer-based hard templates where polystyrene colloidal, polystyrene crystalline arrays and formaldehyde resin are normally used. Among resin, melamine formaldehyde and resorcinol formaldehyde are the most employed. Others platforms used are mesoporous silica, silica shell, mesoporous carbon, solid

carbon, metal-based, ceramic templates, and hard templates based on inorganic and complex salts [31].

In the group of the soft templates one can find the emulsion-based templates, direct emulsion templates for polymer hollow spheres, direct emulsion templates for inorganic hollow spheres, reverse emulsion templates, double emulsion templates, micelle/vesicle-based soft templates, and gas bubble-based soft templates [32]. However, in some cases, direct synthesis without the need of templates is preferred due to practical application issues. In those cases, self-templating strategy is employed. In general, self-templating methods involve a two-step synthesis: (1) the synthesis of template nanomaterials, and (2) the transformation of templates into hollow structures [33]. Unlike the conventional templating methods, the templates used in self-templating methods are not only the templates used to create inner hollow structures, but also the integrated composition of the outer shells [34]. In the surface-protected etching method, the hollow structures can be synthesized by enhancing the relative stability of the surface layer of a single-component nanostructure to make it more stable than the interior and preferential etching of the core part may allow the formation of hollow structures [35].

Indeed, there are a number of unconventional synthetic methods, such as surface-protected etching, Ostwald ripening, Kirkendall effect, and galvanic replacement [36]. The Ostwald ripening describes the change of an inhomogeneous structure over time in solid solutions or liquid sols and involves matter relocation. The IUPAC in 2007 recommended the definition of Ostwald ripening as the “dissolution of small crystals or sol particles and the re-deposition of the dissolved species on the surfaces of larger crystals or sol particles” [37]. Galvanic replacement reaction has been regarded as an effective self-templating method for producing hollow nanostructures with controlled sizes and shapes, porous walls, and tunable elemental composition, especially noble metals [38] . The driven force comes from the electrochemical potential difference between two metals, in which one metal acts as the reducing agent (anode) and the salt of the other metal as the oxidizing agent (cathode). The anode metal nanostructures are synthesized first. Upon contacting with the metal ions with higher reduction potential, the anode metal nanoparticles are oxidized and dissolved into the solution, while the metal ions are reduced and placed onto the outer surface of the anode template. Generally, the shape and interior void size of the final hollow structure closely resemble the initial anode metal template with a slight increase in dimension.

On the other hand, the Kirkendall effect is a classical phenomenon in metallurgy that can be used to obtain hollow nanostructures. It basically refers to a nonreciprocal mutual diffusion process through an interface of two metals so that vacancy diffusion occurs to compensate the unequality of the mass flow. To obtain a better knowledge of this phenomenon it is necessary to understand the general theory of diffusion. This introduction to diffusion mechanism presented in this chapter has

been written with reference to book "Diffusion in solids" by Helmut Mehrer [39].

The equations governing diffusion processes are Fick's laws. These laws represent a continuum description and are purely phenomenological. Fick introduced the concept of the diffusion coefficient and Fick's laws describe the diffusive transport of matter as an empirical physical understanding of diffusion in solids which is based on random walk theory and on the atomic mechanisms of diffusion. In an isotropic medium, physical and chemical properties are independent of direction, whereas in anisotropic media properties depend on the direction considered. Diffusion is isotropic in gases, most liquids, in glassy solids, in polycrystalline materials without texture, in cubic crystals and in icosahedral quasicrystals. In isotropic materials the diffusivity is a scalar quantity.

Fick's First Law. By considering the flux of diffusing particles in one dimension, where the particles can be atoms, molecules, or ions. Fick's first law for an isotropic medium can be written as:

$$J_x = -D\frac{\partial C}{\partial x} \tag{1}$$

where J_x is the flux of particles (diffusion flux) and C their number density (concentration). The negative sign in Eq. (1) indicates opposite directions of diffusion flux and concentration gradient. Diffusion is a process which leads to an equalization of concentration. The factor of proportionality, D, is denoted as the diffusion coefficient or as the diffusivity of the species considered.

Equation of Continuity. Usually, in diffusion processes the number of diffusing particles is conserved. For diffusing specie which obeys conservation law an equation of continuity can be formulated. For infinitesimal size of the test volume Eq. (1) can be written in compact form by introducing the vector operation divergence ∇, which acts on the vector of the diffusion flux

$$-\nabla.\mathrm{J} = \frac{\partial C}{\partial t} \tag{2}$$

Equation (2) is denoted as the *continuity equation*.

Fick's Second Law. Fick's first law Eq. (1) and the equation of continuity (Eq. 2) can be combined to give an equation which is called *Fick's second law* or sometimes also the *diffusion equation*:

$$\frac{\partial C}{\partial t} = \nabla.(D\nabla C) \tag{3}$$

Diffusion equation in various coordinates is, for example, the case when diffusion occurs in a chemical composition gradient. The composition-dependent diffusivity is usually denoted as the interdiffusion coefficient.

Diffusion Mechanism. The hopping motion of atoms is a universal feature of diffusion processes in solids. Diffusivity is determined by jump rates and jump distances. The detailed features of the atomic jump process depend on various factors such as crystal structure, size and chemical nature of the diffusing atom, and whether diffusion is mediated by defects or not. In some cases, atomic jump processes are completely random; in others, correlation between subsequent jumps is involved. There are various mechanisms of diffusion.

Interstitial Mechanism. Solute atoms which are considerably smaller than the solvent atoms are incorporated on interstitial sites of the host lattice forming an interstitial solid solution. Interstitial sites are defined by the geometry of the host lattice. An interstitial solute can diffuse by jumping from one interstitial site to another of its neighboring sites as shown in Fig. 1.1. Then the solute is said to diffuse by an interstitial mechanism.

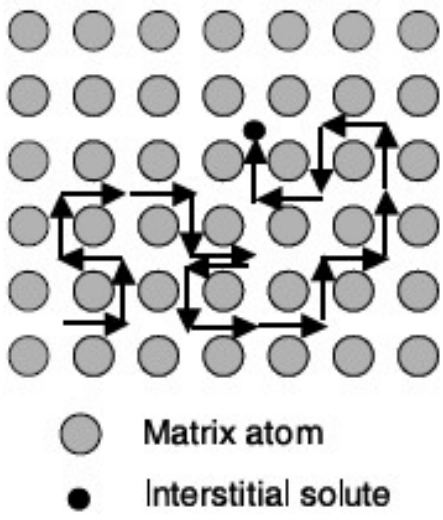

Figure 1.1: Direct interstitial mechanism of diffusion.

Collective Mechanisms. The diffusion of substitutional solutes and solvent atoms themselves requires a mechanism different from interstitial diffusion. In the 1930s, it was suggested that self- and substitutional solute diffusion in metals occurs by a direct exchange of neighbouring atoms (Fig. 1.2), in which two atoms move simultaneously, in collective form. In a close-packed lattice this mechanism requires large distortions to squeeze the atoms. This entails a high activation barrier and makes this process energetically unfavorable.

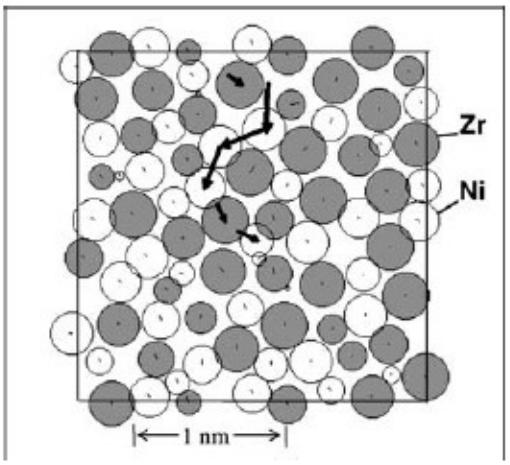

Figure 1.2: Atom chain motion in an amorphous Ni-Zr alloy according to molecular dynamics simulations of Teichler [40].

Vacancy Mechanism. Vacancies have been accepted as the most important form of thermally induced atomic defects in metals and ionic crystals. It has also been recognized that the dominant mechanism for the diffusion of matrix atoms and of substitutional solutes in metals is the vacancy mechanism. An atom is said to diffuse by this mechanism, when it jumps into a neighbouring vacancy (Fig. 1.3). The constriction, which inhibits motion of an adjacent atom into a vacancy in a close-packed lattice, is small as compared to the constriction against the direct or ring exchange. Each atom moves through the crystal by making a series of exchanges with vacancies, which from time to time are in its vicinity.

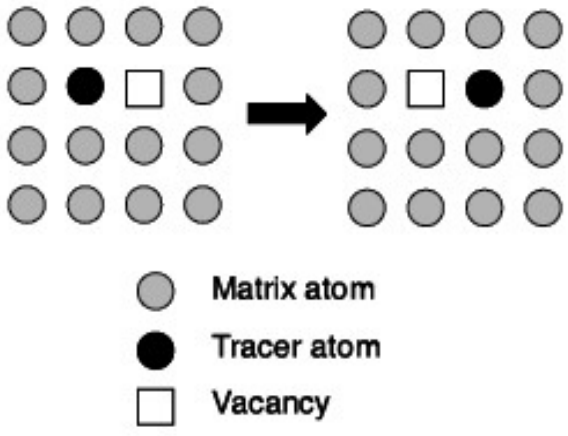

Figure 1.3: Monovacancy mechanism of diffusion.

Divacancy Mechanism. When a binding energy tends to create agglomerates of vacancies (divacancies, trivacancies), diffusion can also occur via aggregates of vacancies. This is illustrated

for divacancies in Fig. 1.4. At thermal equilibrium divacancies are formed from monovacancies. The concentrations of mono- and divacancies at equilibrium increase with temperature. Because of divacancies binding and the lower defect symmetry, diffusion via divacancies obeys slightly modified equations as compared to monovacancies. Otherwise, the two mechanisms are very similar. Diffusion by bound trivacancies is usually negligible.

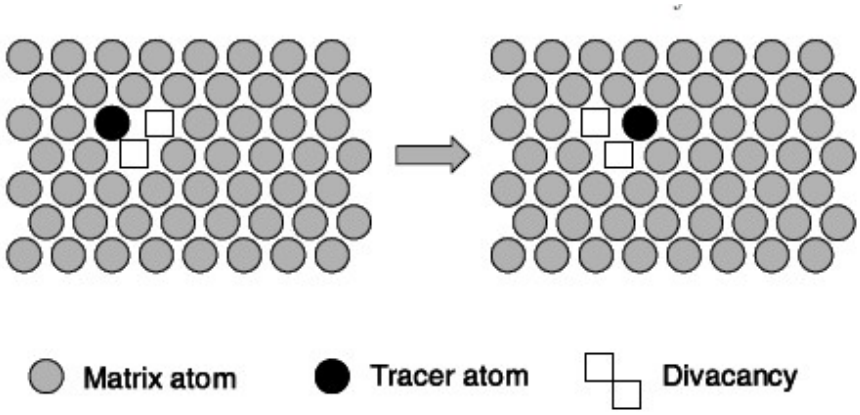

Figure 1.4: Divacancy mechanism of diffusion in a close-packed structure.

Interstitially Mechanism. When an interstitial atom is nearly equal in size to the lattice atoms (or the lattice atoms on a given sublattice in a compound), diffusion may occur by the interstitial mechanism also called the indirect interstitial mechanism. Self-interstitials – extra atoms located between lattice sites – act as diffusion vehicles. Figure 1.5 illustrates a collinear interstitial mechanism. Both atoms move in union – a self-interstitial replaces an atom on a substitutional site, which then itself replaces a neighbouring lattice atom. Interstitialcy mechanisms are collective mechanisms because at least two atoms move simultaneously.

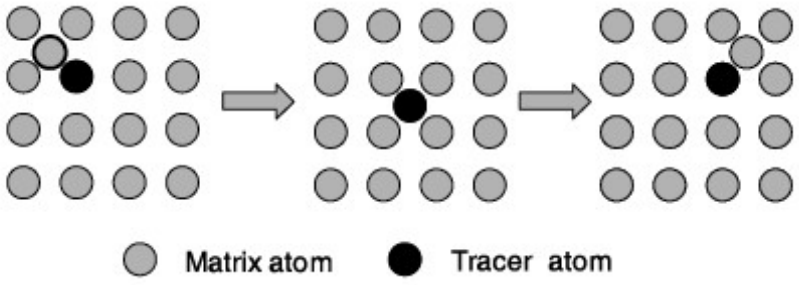

Figure 1.5: Interstitialcy mechanism of diffusion.

Interstitial-substitutional Exchange Mechanisms. Some solute atoms (B) may be dissolved on both interstitial (Bi) and substitutional sites (Bs) of a solvent crystal (A). Then, they can diffuse via one of the interstitial-substitutional exchange mechanisms illustrated in Fig. 1.6. Such foreign atoms are

denoted as ‘hybrid solutes’. The diffusivity of hybrid solutes in the interstitial configuration, D_i, is usually much higher than their diffusivity in the substitutional configuration, D_s.

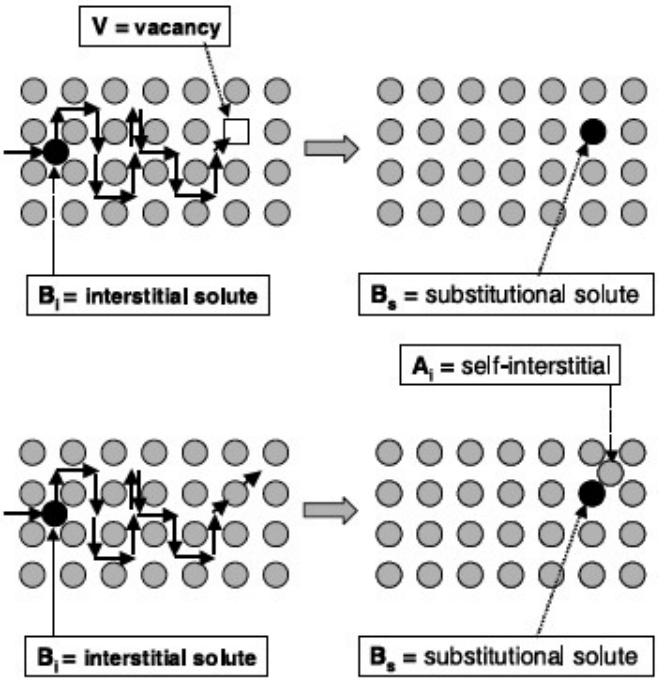

Figure 1.6: Interstitial-substitutional exchange mechanisms of foreign atom diffusion. Top: dissociative mechanism. Bottom: kick-out mechanism.

Diffusion and Driving Forces. Diffusing particles suffer a drift motion in addition to random diffusion, when an external driving force is applied. Table 1.1 lists examples of driving forces. An electric field is the most common example of an external force. Another example is the gradient of the chemical potential. The nature and analytic expressions for the driving forces can be deduced from the thermodynamics of the processes.

Table 1.1. Examples of driving forces for drift motion of atoms

Force	Expression	Remarks
Gradient of electrical potencial $E = -\nabla U$	q^*E	q^*: effective electrical charge
Gradient of chemical potential	$-\nabla\mu$	μ:chemical potential
Temperature gradient ∇T	$-(Q^*/T)\nabla T$	Q^*: heat of transport
Stress gradient	$-\nabla U_{el}$	U_{el}: elastic interaction energy due to stress field
Gravitational force	mgz	m: particle mass g: acceleration due to gravity
Centrifugal force	m^*w^2r	m^*: effective atomic mass w :angular velocity r: distance from rotation axis

Interdiffusion and Kinkerdall effect. In 1947, Smigelskas and Kirkendall observed a movement of the initial interface in a Cu/Zn diffusion couple, as a result of a faster diffusion of Zn into the copper than that of copper into the Zn (the intrinsic diffusion coefficient of Zn is 2.5 times larger than that of Cu at 785 °C) [41]. The Kirkendall experiment revealed two important results: (1) atomic diffusion occurs via vacancies and (2) each metal diffuses at a different mobility. In some cases, condensation of vacancies in excess can give rise to void formation, called 'Kirkendall voids', near to the original interface and within the faster diffusion side. Formation of the Kirkendall voids is basically unfavorable to technological application in alloys. Engineers try to avoid this effect in the case that inter diffusion occurs at the bonded-interface because the Kirkendall voids deteriorate the bonding strength of the bond-pad interface or may cause wire bond failure in integrated circuits. However, recently researchers have applied the destructive effect in a constructively way for synthesizing hollow nanostructures in an approach that the Kirkendall voids coalesce into a single hollow core [42]. Table 1.2 shows some of the hollow nanostructures obtained by using the Kinkerdall effect.

Table 1.2- Hollow nanostructures obtained by using Kinkerdall effect.

Material	Morphology	Publication year	Ref.
Ag_2Se	Nanotubes	2006	[43]
AlN	Hollow particles	2007	[44]
Al_2N	Hollow particles	2007	[45]
Co_3S_4, CO_2. AlO	Hollow particles	2006	[46]
CdS	Polycrystalline nanoshell	2005	[47]
CuO	Hollow nanoparticles	2008	[48]
Co_3S_4	Hollow nanoparticles	2009	[49]
CoSe	Hollow nanoparticles	2006	[50]
MoS_2	Hollow nanoparticles	2007	[51]
NiO	Hollow nanoparticles	2006	[52]
CuS, CuCl	Hollow nanoparticles	2007	[53]
Cu_7S_4	Hollow nanoparticles	2007	[54]
FeO_4	Hollow nanoparticles	2006	[55]
Fe_2O_3	Microcages	2009	[56]

1.3 – Semiconducting materials of interest

Besides the interest of hollow materials fabrication, joining the tubular arrangement with magnetic properties of the samples has become highly attractive because such configuration can be an ideal candidate for multifunctional material toward biomedical applications, such as targeting drug delivery or for capturing, concentrating, and releasing species ranging in size from large proteins to small molecules. Distinctive outer surfaces can be differentially functionalized with environment-friendly and/or probe molecules to a specific target. Therefore, fabrication of magnetic micro/nano hollow structures nowadays has triggered important efforts by materials scientists to develop controlled synthesis methods and analytically study their properties. Different magnetic microrobots have been obtained in other works by using diverse materials to synthesize them. Thus, microtubes of chitosan films containing cobalt and nickel salts [57], cobalt-platinum (CoPt) and cobalt-nickel (CoNi) [58], porous polysulfone [59], comprised soybean protein isolate with poly-L-glutamic acid and magnetite nanoparticles [60], Niquel-Titanium (NiTi) [61] have been reported previously. Despite iron is the most abundant magnetic material in nature, there are few reports

using iron to obtain hollow magnetic microtubes [62]. Herein in the initial part of our thesis, we have work with two iron oxide phases (magnetite and hematite) to obtain hollow magnetic microtubes.

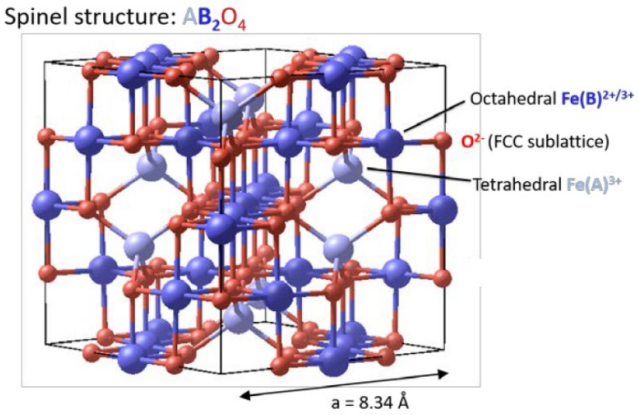

Figure 1.7: Representation of inverse spinel crystal structure of magnetite. The inverse spinel structure of Fe_3O_4 is based on a FCC arrangement of O^{2-} cations in which Fe^{3+} cations occupy 1/2 of the tetrahedral interstices, and a 50:50 mix of Fe^{3+} and Fe^{2+} cations occupy 1/8 of the octahedral interstices. Image extracted from ref [63].

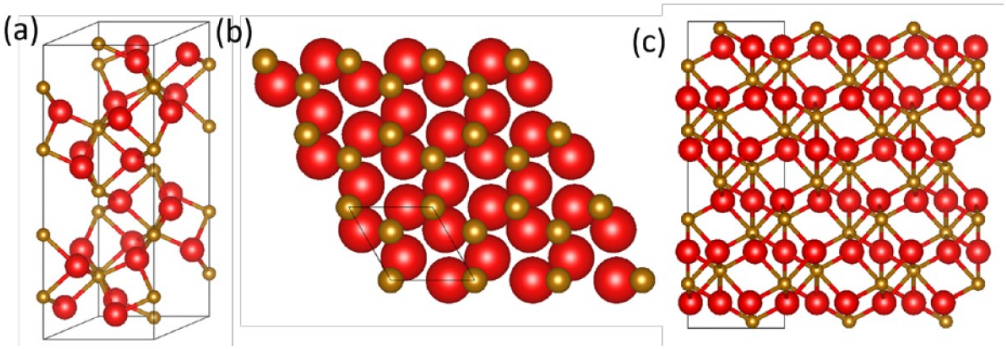

Figure 1.8: Representation of hexagonal crystal structure of Hematite. (a) The hexagonal unit cell of α-Fe_2O_3 contains 6 formula units. O^{2-} anions are red, Fe^{oct3+} cations are brown. (b) Fe^{oct3+} cations occupy two thirds of the octahedral interstitial sites between hexagonal close packed O^{2-} planes (drawn in space filling style with unit cell indicated). (c) Side view of the α-Fe_2O_3 structure that shows how the Fe^{oct3+} cations are not coplanar. Image extracted from ref [63].

Magnetite has a spinel inverse crystalline structure, where tetrahedral (A sites) are occupied by Fe^{3+}, whereas the twice octahedral (B sites) are randomly occupied by Fe^{2+} and Fe^{3+} (Fig. 1.7). Hematite exists in two forms, α-Fe_2O_3, which has a hexagonal structure, and γ-Fe_2O_3, which is cubic. In our case, Fe_3O_4 oxidizes to form α-Fe_2O_3 (Fig. 1.8).

The other systems studied in this work were a couple of samples belonging to the chalcogenides family. Systematic research on materials based on chalcogens (sulphur, selenium and tellurium), called chalcogenides, started at the middle of the twentieth century. Many researchers have tried to synthesize non-oxides semiconductors with narrow band gap for the visible-light-driven catalysis. The chalcogenides *SnX* (X: S, Se and Te) are relatively little investigated in

photoelectrochemical (PEC) cells and solar devices compared to oxides [64]. Among the congeners, tin sulfides are used in semiconductor sensors, photocatalysts [65], optoelectronic devices [66], solar cells [67], and near-infrared (NIR) detectors [68]. Moreover, tin sulfides family shows a variety of phases such as *SnS*, Sn_2S_3, Sn_3S_4, Sn_4S_5, and SnS_2. The constituent elements are nontoxic, inexpensive and relatively abundant in nature; *Sn* and *S* atoms are bonded in layer by weak Van der Waals forces [69]. *SnS* is reported to be n-type semiconductor with an orthorhombic crystalline structure and has attracted much attention in the solar energy conversion due to its optimal band gap (Eg ~ 1.3 eV), high absorption coefficient of ~104 cm^{-1} and moderate electrical conductivity [70]. Up to now, *SnS* with different morphologies was produced by chemical bath deposition [71], and electrochemical plating method [72].

On the other hand, *ZnS* is an important semiconductor compound of the II-VI group which has a wide band gap of 3.7 eV at room temperature and a relatively large exciton binding energy (40 meV) and it has been extensively investigated [73]. Several *ZnS* nanostructures, including nanowires, nanobelts, nanoribbons, and nanowires have been successfully synthesized using a variety of methods such as thermal evaporation, laser ablation catalytic growth, Self-assembly, and chemical vapor deposition [74,75, 76, 77]. *ZnS* nanowires have attracted much research attention because they promise to open huge potential applications for optoelectronics and other interdisciplinary utilities such as: nano LEDs, nano FETs and nano laser that can operate at room temperature [78,79, 80]. In most of the previous studies, effort has been paid to develop and explore methods to grow highly crystalline nanowires and to control the size and the dimensionality of *ZnS* nanostructures. Much less attention has been placed on other applications. Also, information on the optical properties ZnS nanowires and the dependence on the photoluminescence on the morphology of ZnS nanostructures is still lacking.

Both magnetite and hematite are magnetic materials, being the magnetite classified as ferrimagnetic and the hematite as antiferromagnetic. To understand this material's classification we present a simple introduction to magnetic properties such as diamagnetism, paramagnetism, ferromagnetism, antiferromagnetism and ferrimagnetism. This introduction to magnetism presented in this chapter has been written with reference to books by Stephen Blundell [81], and David Jiles [82]. Magnetism in materials arises from electronic configuration which induces effects associated with isolated magnetic moments and/or interactions among them. Electrons in atoms possess magnetic moments due to both their intrinsic spin and their orbital motion. An atomic magnetic moment for a multi-electron atom depends on the exact configuration of its electrons, in particular on the spin (*S*) and orbital (*L*) components, which are governed by quantum mechanics and simplified in Hund's rules. The total angular magnetic momentum of an atom, *J*, is the sum of *S* and *L* according to Hund's rules. Typically, the atomic moments macroscopically sum zero in the

absence of an applied magnetic field since they are disordered by thermal fluctuations. These materials are named paramagnets. However, in a small number of cases, namely for some *3d* transition metals and *4f* rare earth metals, collective ordering of atomic magnetic moments occurs in the absence of an external field, and a non-zero net magnetic moment may arise. This net magnetic moment per unit volume is designated as magnetization, *M*. In order to differentiate between the different classes of magnetism, it is useful to define the magnetic susceptibility, that is, the degree to which a material's magnetization, *M*, responds to an applied magnetic field, *H*. The magnetic susceptibility is, χ_m, defined as:

$$M = \chi_m H. \tag{4}$$

It is also useful to define the permeability, μ, of a material, which is the degree to which a material's magnetic flux density *B* responds to a magnetic field *H*:

$$B = \mu H. \tag{5}$$

Since $B = \mu_0(H + M)$, in which μ_0 is the permeability of free space, a large susceptibility implies a large permeability and viceversa ($\mu = \mu_0(\chi_m + 1)$).

Diamagnetism and Paramagnetism. Diamagnetism is the term used to describe a weak increase in a magnetization of one material in a direction opposite to an applied magnetic field, i.e., a weak negative susceptibility. It comes from electron in closed shells. All materials exhibit this effect and it had origin in quantum mechanical phenomenon. In materials with a net atomic magnetic moment, *J*, other effects such as paramagnetism dominate over diamagnetism. In a paramagnetic material in zero external magnetic fields, non-zero atomic magnetic moments are distributed randomly due to thermal fluctuations. However, in the presence of an external magnetic flux density, *B*, each magnetic moment, *m*, has an associated potential energy, $U = -mB$, which is minimized when the magnetic moment is aligned with the external field. This gives rise to a positive susceptibility. In a high magnetic field, all the magnetic moments in a material are aligned and a saturation magnetization, M_S, is reached. Both diamagnetism and paramagnetism describe the net effect of many isolated magnetic moments. Nevertheless, interactions between neighboring moments are important in some materials and must be considered in order to gain a more complete representation of magnetism.

Collective magnetism. A ferromagnetic ordering takes place when the neighboring atomic magnetic moments aligns parallel with respect to each other (Fig. 1.9 (a)). This can produce large macroscopic magnetization in the absence of external magnetic fields. Conversely, an antiferromagnetic ordering is a material in which neighboring magnetic moments may spontaneously align anti-parallel with respect to their nearest neighbors yielding no net macroscopic magnetization (Fig. 1.9 (b)).

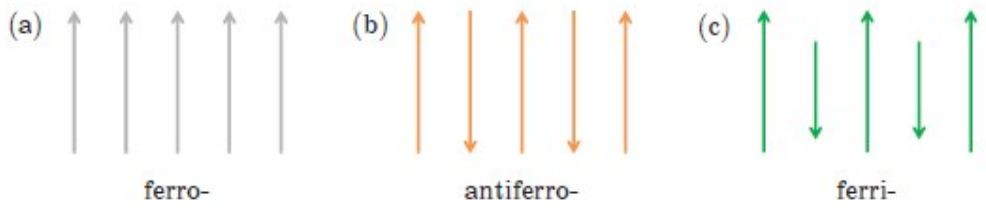

Figure 1.9: Schematic showing spontaneous ordering of magnetic moments in (a) ferro-, (b) antiferro- and (c) ferri-magnets.

In ferrimagnets, like in antiferromagnets, neighbouring magnetic moments may spontaneously align anti-parallel, however a net macroscopic magnetization may arise since the neighboring moments are of different magnitudes (Fig. 1.9 (c)). Since these three magnetic effects mentioned depend on the orientation of neighboring magnetic moments, they are said to be collective magnetism effects. These effects arise due to the exchange interaction among ions in the system.

Ferromagnetic behavior as a function of temperature. Ferromagnets exhibit spontaneous magnetic moment ordering in the absence of applied magnetic fields due to the exchange interaction. This ordering may be reduced by the presence of thermal energy due to a finite thermal energy which acts to randomize the magnetic moments. If the temperature is increased gradually from absolute zero in zero external field, the magnetization decreases. Eventually, at the so called Curie Temperature of the material, the thermal effects dominate over the exchange interaction and the material starts to behave as paramagnetic. This is a reversible transition and on cooling back through the Curie temperature the material starts to order again. A schematic of magnetization in ferromagnetic materials as a function of temperature is shown in Fig. 1.10

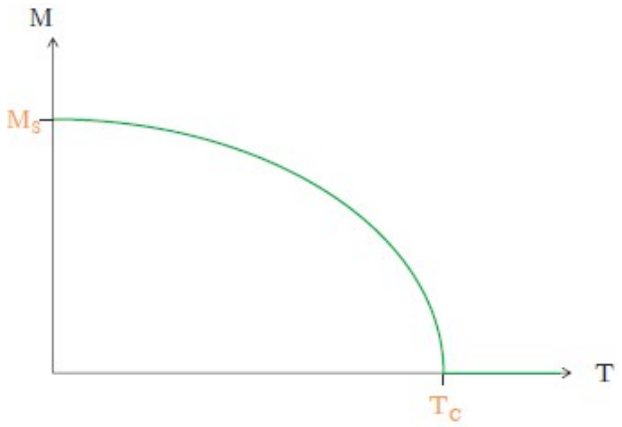

Figure 1.10: Schematic picture of a spontaneous magnetization as a function of temperature in ferromagnetic materials. At absolute zero temperature, the saturation magnetization may be achieved. As temperature is increased from zero temperature, ordering is reduced until the Curie Temperature when all spontaneous ordering is lost.

Magnetic hysteresis. A magnetic state may be altered in the presence of an external magnetic field. Ferromagnets are said to be hysteretic because the magnetic states they support depend on the external magnetic field history. For example, if a ferromagnet is magnetized in the +x direction to saturation and then the external magnetic field is removed, the ferromagnet retains a remanent magnetization in the +x direction. On the contrary, if the ferromagnet is magnetized in the –x direction to saturation and the external magnetic field is removed, the remanent magnetization is in the −x direction. It means that for ferromagnetic materials the orientation of the system depends on its history. Fig. 1.11 illustrates magnetic hysteresis in the context of the saturation magnetization, M_S, the maximum magnetization achievable under high fields, the remanent magnetization, M_R, the magnetization that remains after saturation on removal of the external magnetic field, and the coercive field, H_C, the magnitude of external magnetic field in the direction opposite to saturation required to demagnetize the system. The magnitude of the coercive field, H_C, reflects how easy a structure is demagnetized. If a structure is anisotropic due to its shape or crystal structure, its coercivity depends on the direction of the externally applied magnetic field, H, and is maximal when H is aligned along the easy axis of magnetization. Materials which have a high coercivity are said to be hard and are not easily demagnetized. Most materials, however, are naturally soft, since are demagnetized in low external magnetic fields and hence have small coercivity.

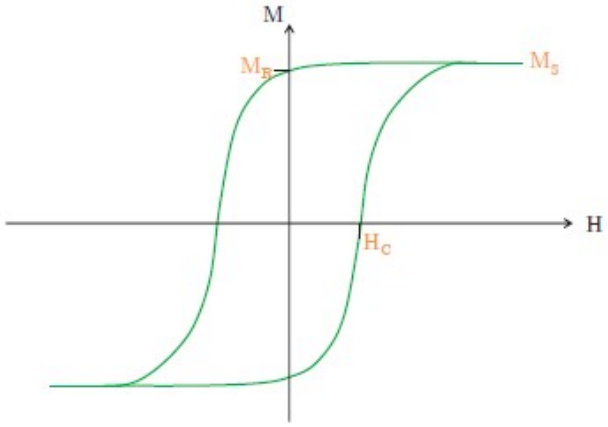

Figure 1.11: Schematic picture of a hysteresis loop for a typical ferromagnet showing the magnitude of the net magnetization, *M*, along the same axis as an externally applied magnetic field, where *H*. M_S, M_R and H_C correspond to the saturation magnetization, remanent magnetization and coercive field respectively.

1.4- Objectives of this work

The main objective of this work is to obtain a better understanding of both oxidation and sulfurization process in metals due to thermal treatment. Bellow, we list some specific objectives:

1. To synthesize iron oxide micro/nano structures using a free-catalytic synthesis method based in thermal oxidation assisted with the passage of electrical current.
2. To characterize the morphological, structural, magnetic, and electrical transport properties of micro/nanomaterials.
3. To investigate the interactions between nanostructures and biological systems to probe the biocompatibility the iron oxides micro/nano structures.
4. To build a magnetic bio/micro/nano robot (wireless microsystems) based on hematite/magnetite structural phases.
5. To synthesize hollow micro/nano structures of SnS and ZnS (chalcogenides) by a free-catalytic new route based on thermal treatment of both sulfur power and metal wire under controlled atmosphere.
6. To study the morphological, topological, structural, and optical properties of the SnS and ZnS samples.
7. To investigate the viability of the obtained chalcogenides to photodegradation of organic dyes from aqueous solution.

CHAPTER 2: CHARACTERIZATION TECHNIQUES

2.1- Electrical Resistivity and *in situ* sample preparation

The electric transport mechanism for all samples produced in this work was studied by dc electrical resistivity measurements as a function of temperature. For this, the construction of an apparatus capable of measuring electrical resistance at high temperatures is required. All measurements were performed using the four probe method at different temperature ranges. The sample holder was constructed of ceramic material which in addition to electrical insulation withstands high temperatures. A picture of this apparatus is shown in Fig. 2.1.

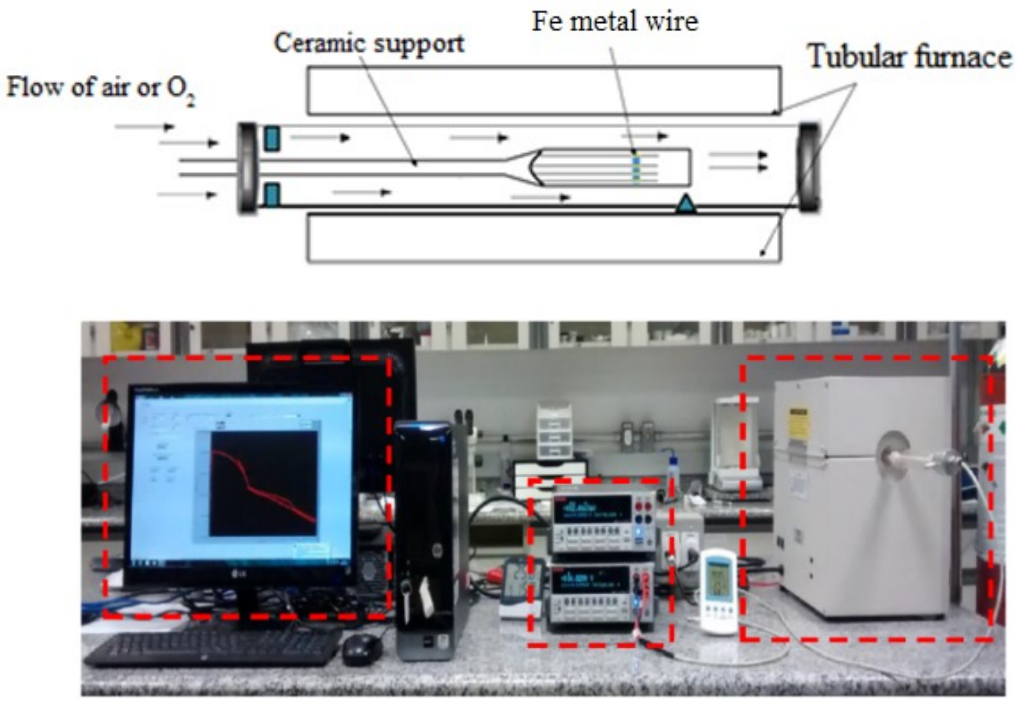

Figure 2.1: The electric transport measurement apparatus.

2.2- X- Ray diffraction

All samples produced during the development of this work were characterized by X-ray diffraction (XRD) measurements. These characterizations have as a primary objective the identification of crystallographic phases in the samples. XRD measurements were obtained using a Bruker Diffractometer Model D8 Focus, operating in transmission mode with radiation of $CuK\alpha_1$ λ = 1. 54056 Å; in Bragg-Brentano configuration (θ-2θ). We used an angular pitch 0.01 ($2\theta^o$) with

an angular step by time t = 1.5 s. The crystal structure was refined using the Rietveld method using the Topas software.

Figure 2.2: Bruker Diffractometer Model D8 Focus employed for XRD measurements.

2.3- Magnetization Measurements

Magnetic susceptibility measurements were carried out by using the Superconducting Quantum Interference Devices (SQUID) of Quantum Design from the experimental multiuser center at UFABC. This equipment allows magnetization measurements using a vibrating sample magnetometer (VSM). All samples were characterized by measuring the magnetization as a function of temperature and by applying different magnetic fields on Field Cooling (FC) and Zero Field Cooling (ZFC) modes.

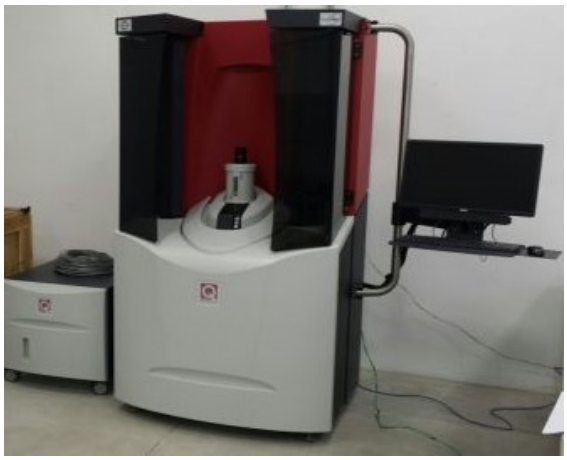

Figure 2.3: Quantum Design MPMS SQUID VSM used to magnetic measurements.

2.4- Scanning Electron Microscopy

In order to study the morphological properties of the produced samples, scanning electron microscopy experiments (SEM) were performed by using a microscope model JSM-5500 of JEOL Thermocientific. A scanning electron microscope comprises an electron gun that produces an electron beam in a vacuum column with pressures lower than 10^{-4} mbar. The energy of an electron beam incident may be a few hundred eV to 30 keV. The electron beam is focused on a small surface of the sample mounted previously on aluminum sample holder. The samples were attached to the aluminum sample holder with carbon tape.

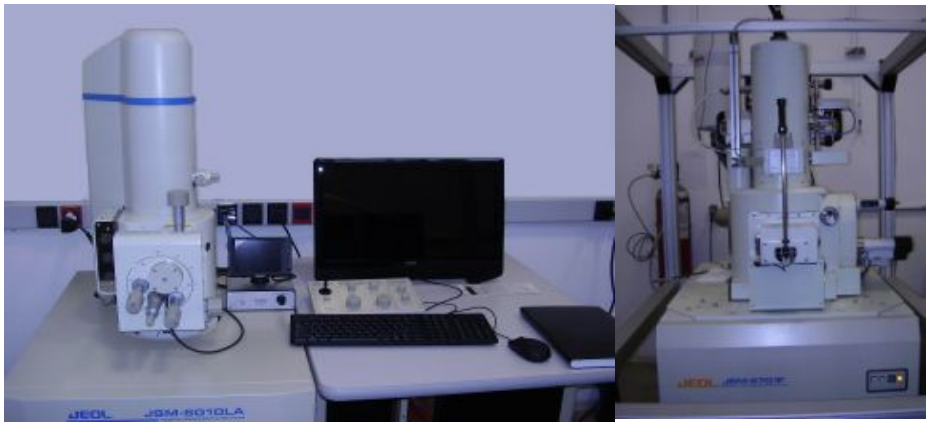

Figure 2.4: Scanning electron microscopy JSM-6010LA JEOL (left) and field emission Scanning electron microscopy FESEM JMS-6701F, JEOL (right) used to morphologic characterization.

2.5- Raman spectroscopy

Raman measurements were performed by using a triple spectrometer (T64000, HORIBA Jobin-Yvon) with a thermoelectric cooled CCD detector (Synapse, HORIBA Jobin-Yvon). The 532 nm line of an optically pumped semiconductor laser (Verdi G5, Coherent) was used as the excitation source. The laser power at the sample was maintained below 5 mW on a spot of ~10 microns. Raman spectroscopy is a form of vibrational spectroscopy, much like infrared (IR) spectroscopy. However, whereas IR band arise from a change in the dipole moment of a molecule due to an interaction of light with the molecule. Raman bands arise from a change in the polarizability of the molecule due to the same interaction. This means that these observed bands (corresponding to specific energy transitions) arise from specific molecular vibrations. When the energies of these transitions are plotted as a spectrum, they can be used to identify the molecule as they provide a "molecular fingerprint" of the molecule being observed. A Raman system is conceptually simple and includes the following main components: a laser excitation source, excitation delivery optics,

collection optics, wavelength separation device, detector and associated electronics, and recording device.

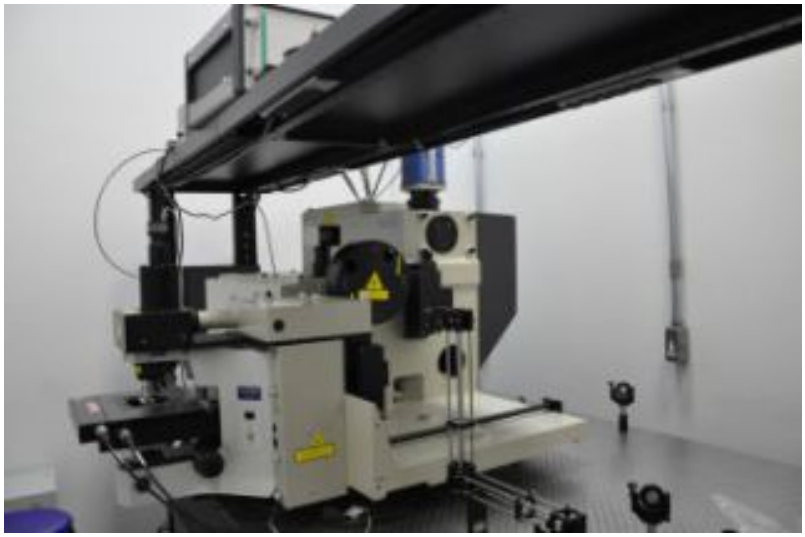

Figure 2.5: Raman dispersive Spectroscopy T64000, Horiba Jobin-Yvon.

2.6- UV-Vis spectroscopy

Electronic absorption or UV-visible spectroscopy is one of the simplest and yet most useful optical techniques for studying optical and electronic properties of materials. Most of the organic molecules and functional groups are transparent in the portion of the electromagnetic spectrum which we call the ultraviolet and visible regions. That is the region, where wavelength ranges from 190 nm to 800nm.

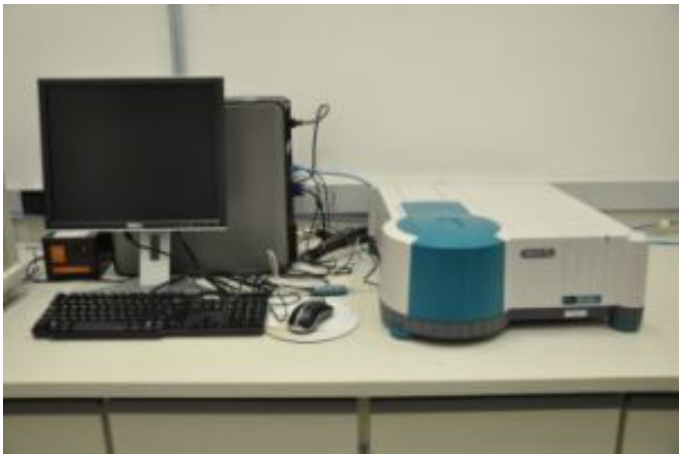

Figure 2.6: UV-VIS Spectrophotometer Cary 50-Varian.

The basic principle of electronic absorption spectroscopy is based on the measurement of light absorption due to electronic transition in the sample. The energy adsorption due to atoms and

molecules pass from a state of low energy, ground state, to a state of higher energy, excited state. The electromagnetic radiation that is absorbed has energy exactly equal to the energy difference between the excited and ground state. UV-VIS measurements were executed in the Cary 50-Varian Spectrophotometer from the experimental multiuser center at UFABC.

2.7- Atomic force microscopy

To explore the topology of obtained samples AFM device was employed. The scanner head is a piezoelectric tube scanner capable of up to 90 x 90 micron scans with 1% lateral accuracy and a 6.7 micron vertical range. The AFM includes an optical microscope with 1.5 micron resolution for ease of navigating on the surface. All roughness calculations were made using Gwyddion free software. The images are flattened before calculations are made. For our case, measurements of superficial roughness (Rq and Ra) were executed.

The RMS (Rq) roughness is the standard deviation of the z values:

$$R_q = \sqrt{\frac{\sum_{i=1}^{N}(Z_i - Z_{av})^2}{N}}$$

Meanwhile, the mean roughness (Ra) is the arithmetic average of the deviations from the center plane,

$$R_a = \frac{\sum_{i=1}^{N}|Z_i - Z_{av}|}{N}$$

Figure 2.7:Atomic force microscopy AFM/SPM Series 5500 - Agilent.

CHAPTER 3: RESULTS AND DISCUSSION

3.1- AFM/FIM magnetic microtubes decorated with nanowires

Over the last few years, significant effort has been focused on the synthesis of hematite (Fe_2O_3) and magnetite (Fe_3O_4) nanostructures in order to understanding growth mechanism due to important properties observed on both compounds such as magnetism, stability under ambient condition, high resistivity to corrosion and low toxicity [83-84]. These properties place these two iron oxide compounds as materials with great technological potential for a wide range of applications in fields such as catalysis, gas sensors, magnetic recording media, spintronic, sensor devices, and nanobiotechnology [85,86]. Different routes such as thermal oxidation [87], catalyzed oxidation [88], microwave-assisted reflux method [89], and pyrolysis methods [90] have been used to synthetize these micro/nanostructures. On the other hand, hollow magnetic structure with the presence of both iron oxide phases is absent in literature and, as far as we know, there are no reports on hematite and magnetite microtubes fabrication. The studied systems in our experimental work were magnetic microtubes obtained from pure iron wires resulting in a structure containing two oxides phases: magnetite (Fe_3O_4) and hematite (Fe_2O_3). In this case, our principal goal of obtaining both hollow and magnetic structures is reached, as we will show in details in this chapter. This hierarchical microstructure combining antiferromagnetic (AFM) hematite, ferrimagnetic (FIM) magnetite, and hematite nanowires on the surface was produced through a very simple method by using thermal oxidation along with electrical current, which constitutes a simple and new route to obtain hollow magnetic micro/nano structures.

3.1.1-Iron metallic microwire

Since iron (Fe) is our precursor material in all carried out experiments, some of its physical properties are presented. At atmospheric pressure, there are three allotropic forms of iron: alpha iron (α) or ferrite, gamma iron (γ) or austenite, and delta iron (δ). At very high pressure, a fourth form appears, called epsilon iron (ε) or hexaferrum. At room temperature, iron has a body centered cubic (bcc) crystal structure with spatial group *Im-3m* (Fig. 3.1 (a)). At temperature T = 1043 K (770 °C), known as Curie temperature (T_C), iron has a magnetic transition and becomes paramagnetic. As iron passes through Curie temperature there is no change in crystalline structure, but there is a change in the magnetic properties as magnetic ions becomes disordered. At 1183 K (910 °C), α-iron is formed, and the crystal structure changes to face centered cubic (fcc). As the iron is heated further to 1653 K (1380 °C) it becomes into its δ allotrope, which has a body-centered cubic (bcc) crystal

structure. Finally, at 1811 K (1538 °C), iron melts. Figure 3.1(a) shows the X-ray diffraction measurement of pure iron microwire used in all our experiments, which belongs to I*m-3m* space group and has a diameter of 75 μm, as can be observed in SEM images of Figure 3.1(b) and (c). Table 3.1 shows some of the main physical properties of metallic iron.

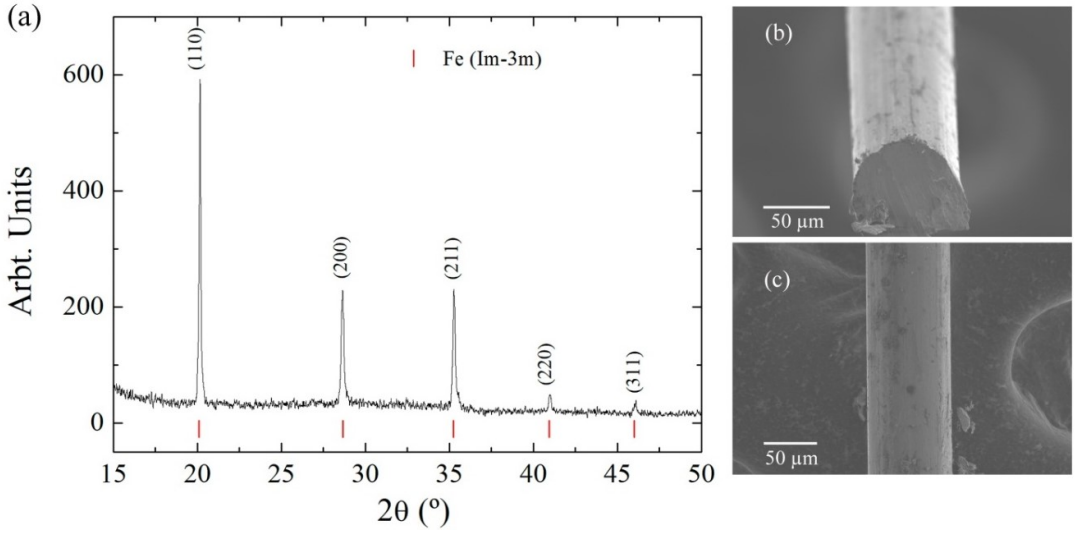

Figure 3.1: (a) X-ray diffraction measurement (belong to the *Im-3m* space group) and (b), (c) SEM images of iron microwire used in the experiments.

Table 3.1: Physical features of Iron [91].

Melting point	1538 °C
Boiling point	2861 °C
Linear thermal expansion coefficient	12.6 x10^{-6} K^{-1}
Electrical resistivity at Room Temperature	9.71x10^{-6} Ω.cm
Density	7.87 g/cm^3
Ferromagnetic Curie temperature	770 °C

To gain a better understanding of magnetic behavior in the used iron microwire, we have performed magnetization as a function of temperature measurements (Fig. 3.2). In this work, the magnetization values are given per unit of total mass (emu/g). The saturation magnetization of bulk iron has been previously reported (218 emu/g at 20 °C) [92]. The ferromagnetic–paramagnetic transition was not observed directly because the SQUID setup is equipped with a furnace which heat the samples only up to 1000 K (727 °C). An estimation of T_c can be obtained with the extrapolation of the obtained results. The estimated Curie temperature of Fe wire is T = 1032 K, which is slightly lower than the Curie temperature of the bulk iron (T = 1043 K) [91].

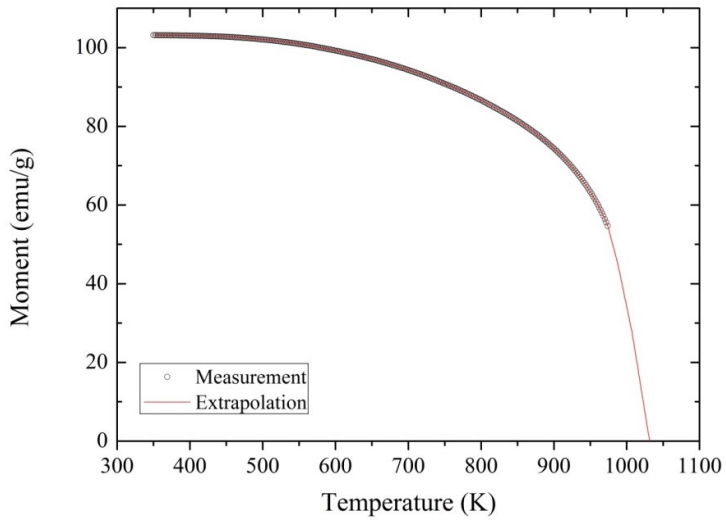

Figure 3.2: Magnetization as a function of temperature for pure iron microwire measured at a constant magnetic field of 500 Oe. Black curve corresponds to the experimental measurement and line shows an extrapolation for high temperatures.

3.1.2- Microtube formation and *in situ* electrical resistivity measurements

As we have discussed, in our case an alternative method was used to fabricate our samples. This method combines thermal oxidation and the application of an electrical current over the pure microwire metal. Resistivity measurements reveal important information about the whole process. The most remarkable observation is a change in the metallic behavior of the sample to a semiconductor-like at high temperature close to T ~ 800 C. Scanning electron microscopy images revealed that this change in the electrical resistivity behavior is closely related to a morphological transformation of the initial iron microwire into an oxide semiconducting microtube.

Figure 3.3 shows *in situ* electrical resistivity measurement for the microwire as a function of temperature between 30-900 °C. The conventional metallic behavior is observed until T~800 °C, since electrical resistivity increases almost linearly with increasing temperature. Above this temperature, henceforth named *morphological transformation temperature* (T_{MT}), there is a robust increasing in the electrical resistivity revealing deviation of metallic behavior, which indicates that the oxidation process becomes more pronounced. When the system is cooled down, the electrical resistivity increases, which correspond to a semiconductor-like behavior. Thus, the results indicate an electrical transport change from metallic to semiconductor properties. Interesting, besides the electrical behavior changing, scanning electron microscopy (right panel Fig. 3.3) of the final sample shows the formation of a hollow microtube. Thus, by carrying out *in situ* electrical resistivity measurements, we were able to assist simultaneously the oxidation process which drastically changes the electrical, and morphological properties of the sample.

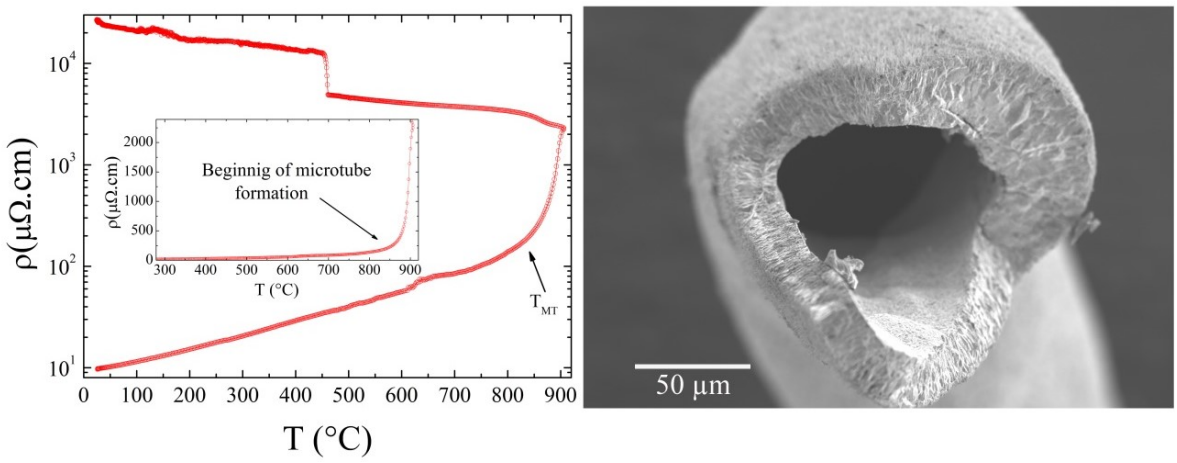

Figure 3.3: *In situ* electrical resistivity measurement of microwire which reveals metallic-semiconductor transition at T ~800 °C. Right panel shows a SEM image of the final sample obtained after thermal oxidation and electrical current passage. The initial microwire has been turned into a microtube on a *temperature of morphological transformation* (T_{MT}).

Sequential experimental measurements were carried out in order to explore different systematics starting from a pure iron microwire and resulting in a microtube formation. One of the first changing parameters is the set point temperature. Therefore, experiments consisted in measuring the electrical resistivity starting from room temperature with an electrical current of 10mA up to T = 700 ºC, T = 900°C, T = 950 ºC, followed by cooling down the system to room temperature were executed. Figure 3.4 shows results obtained for this systematic. At T = 700 ºC, (red line) resistivity value of the microwire is still in agreement with the value expected for metallic iron ($\rho_0 = 9.71\text{x}10^{-6}$ Ω.cm), and evolution of the measurements indicates a typical metallic behavior, that is, as the system is heated up, resistivity increases and as the system is cooled down, resistivity decreases. However, the electrical resistivity increases in the whole measured temperature interval, suggesting small oxidation on the surface of the microwire. This result is, therefore, a clear indication of a core/shell formation (iron/ iron oxide) when the measurements takes place up to T = 700 ºC. Next measurement carried out up to T=900 ºC showed that in temperature of T~800 °C electrical resistivity starts to increase abruptly changing from $9.74\text{x}10^{-5}$ Ω.cm to $2.6\ \text{x}10^{-3}$ Ω.cm. Indeed, there is a jump, which reveals a metallic microwire transformation into a semiconducting sample. This result is corroborated by the cooling curve where an increment of resistivity value is observed. For setting point temperature larger than T=700 ºC, resistivity as a function of temperature presents a semiconductor like behavior for all cooling curves. This results indicate that the oxidation process through diffusivity of ions is most pronounced above T= 700 °C.

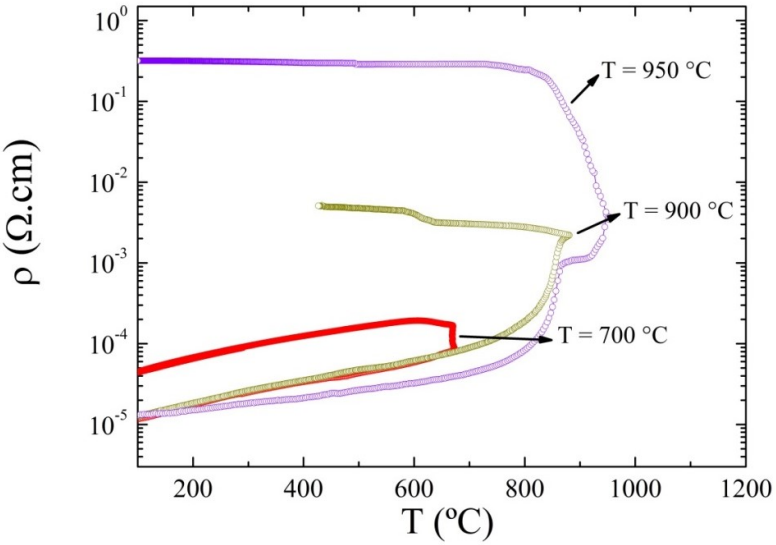

Figure 3.4: Electrical resistivity as a function of temperature for three Fe microwires measured during oxidation process in temperatures T = 700 ºC (red line), T = 900 ºC (olive line), and T = 950 ºC (purple line), followed by cool down the system to room temperature.

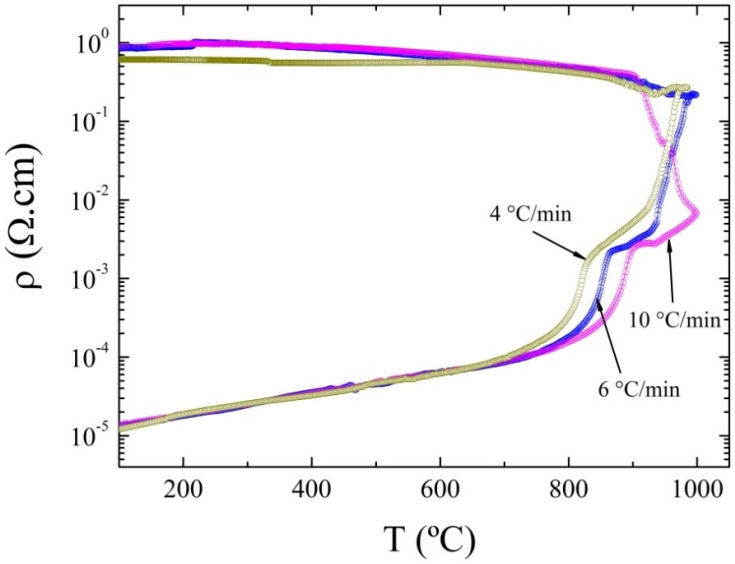

Figure 3.5: Electrical resistivity as a function of temperature for three iron microwires treated with different heating rates up to 1000 ºC followed by cooling process.

We also studied the role of heating rate (HR) on the oxidation process for a set point temperature of T=1000 °C. Figure 3.5 shows electrical resistivity measurements for three microwires by using different HR (fast, intermediate and slow rate) of 10°C/min (magenta line), 6°C/min (blue line) and, 4°C/min (olive line), respectively. Results indicate a similar behavior for the three samples, that is, a semiconductor-like behavior is observed for all of them during cooling curve. In the measurements there is an abrupt change in the resistivity, at T ~ 750 °C, accompanied by an additional jump. Interestingly, the jump temperature is different depending on the HR used for each measurement. There is a leftward shift on T_{MT} when the heating time is lower. The value of the

electrical resistivity of the samples after cooling does not present great difference for intermediate and slow heating rates, but a slight difference is appreciated in comparison with the fast heating rate, where a lower value of electrical resistivity is observed. It indicates that fast HR may produces sample with low resistivity when compared with the sample obtained with slow HR. Electric resistivity of magnetite has been reported to be lower than hematite [93,94]. Thus, result may be an indication that fast heating process could aid the magnetite phase formation over the hematite one.

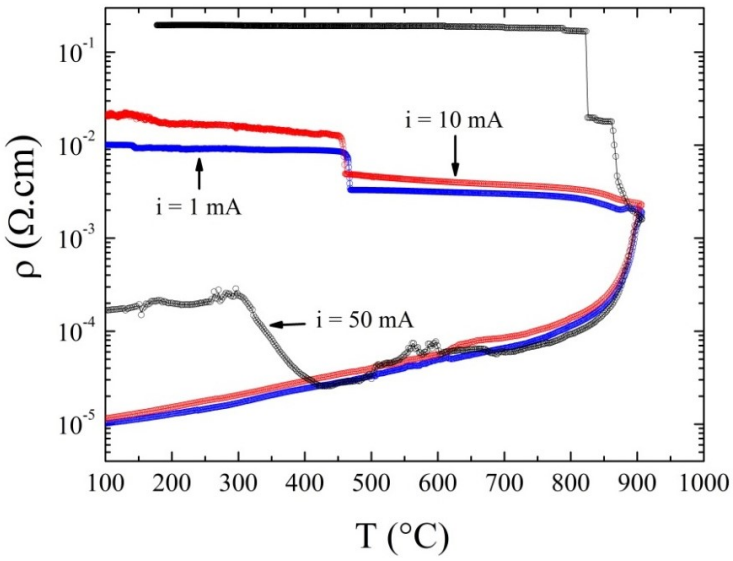

Figure 3.6: Electrical resistivity as a function of temperature for three Fe microwires with electrical current of 1mA (blue line), 10mA (red line), and 50mA (black line) measured during oxidation process up to 900 ºC.

Another systematic measurement was performed by changing the electrical current value. In this case, electrical currents of 1, 10 and 50 mA were applied through the iron microwire during the thermal oxidation process on a fixed heating rate of 10°C/min and set point temperature of 900 °C. Figure 3.6 shows the obtained results. A similar behavior is observed on the heating curve for the three measurements (just an anomalous behavior for i=50 mA at low temperature probably associated with the impurity presence in the sample). On the other hand, evident changes can be observed on cooling curves where the electrical resistivity increases drastically, most pronounced for i = 50 mA. As in the last case, this change in the electrical resistivity can be related to the oxidation process evolving dynamical phase transformation from magnetite to hematite and intermediate iron oxide phases.

In the last systematic involving sample preparation, we have used an electrical current of 10mA up to T= 900 C and heating rates of 4 °C/min, 6 °C/min and 10°C/min. Figure 3.7 shows results obtained adopting this procedure. For these particular experimental conditions, electrical resistivity measurements reveal two important facts to take into account. The first one is the shift on *morphological transformation temperature* (T_{MT}) to lower temperature for long HR in the heating

curve. The second one is the presence of a jump on the cooling curve in all measurements, but with the particularity of a leftward shift of this jump in the electrical resistivity measurements depending on whether heating rate used is greater. Thus, when a fast heating rate is used (blue line) the jump appears at T = 700 °C, but when a lower heating rate is applied the jump for this case appear at T=450°C. Depending on heating rate of each measurement, this critical change in the resistivity shifts to higher temperature. As said before, this abrupt change in the cooling curve may be related to the oxidation process evolving phase transformation of iron oxides.

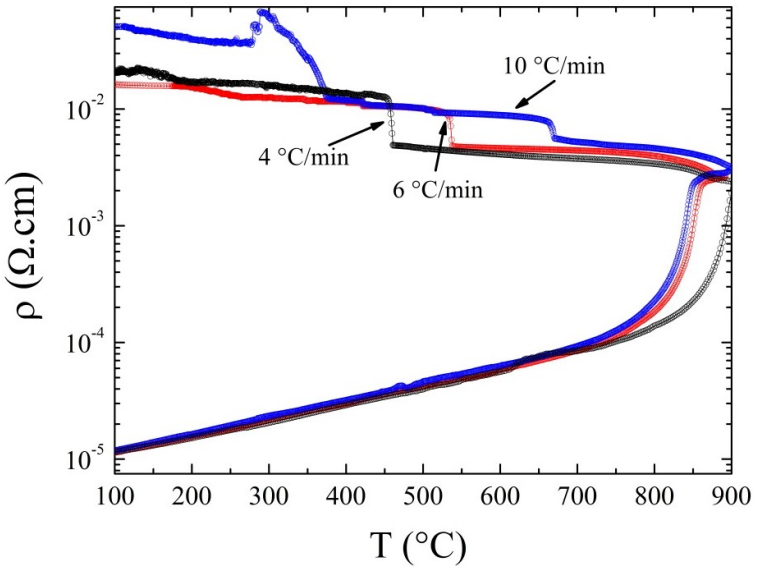

Figure 3.7: Electrical resistivity as a function of temperature for three Fe microwires (heating rates of 10 ºC/min (curve blue), 6 ºC/min (curve red), and 4 ºC/min (curve black)) measured during oxidation up to 900 ºC followed by cooling process.

This complete set of *in situ* electrical resistivity measurements carried out as a function of temperature, electrical current, and heating rate indicates a first experimental approximation revealing which role each parameter could have on the electrical properties of synthetized samples. With the aim to obtain a deep and better understanding on the as prepared samples, structural, morphological, and magnetic physical property characterizations have been done which will be show in the sequence.

3.1.3- Iron oxide formation and structural properties

Before presenting structural properties result, it is important to analyze the phase diagram of the iron–oxygen system shown in Fig. 3.8. In there, it is observed that usually the oxidation of pure Fe result in several crystal phases such as FeO, Fe_3O_4, and Fe_2O_3. Phase formed on oxidized iron above 570 ºC is predominantly FeO (Wüstite). Normally, the growth of this phase controls the

overall rate of oxidation. The wüstite phase is a p-type metal-deficit semiconductor which can exist over a wide range of stoichiometry, from $Fe_{0.95}O$ to $Fe_{0.88}O$ at 1000 ºC. With high cation-vacancy concentrations, the mobilities of cations and electrons (via vacancies and electron holes) in FeO are extremely high. Increasing the oxygen partial pressure in the oxidation should theoretically lead to an increase in the relative thickness of the hematite phase [95]. In fact, it was reported that FeO was formed initially and subsequent heating leads to the transformation of FeO to α-Fe_2O_3/Fe_3O_4 layer [96]. This is particularly important for our case because it can explain the absence of Wüstite phase in the prepared samples.

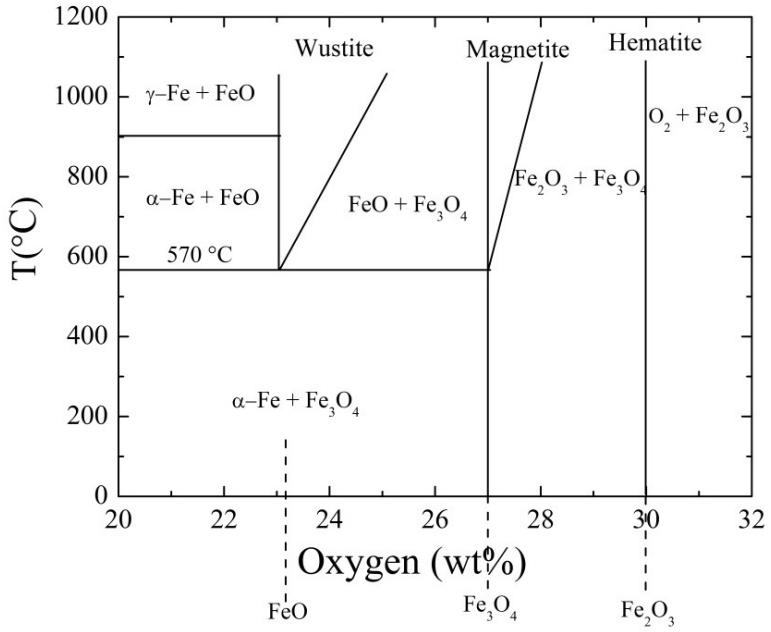

Figure 3.8: The Iron-Oxygen phase diagram [35].

With the purpose of identifying crystal phases of our samples oxidized according to processes discussed in last section, X-ray diffraction measurements were performed. Results are presented in Figure 3.9. X-ray diffraction pattern shown in Figure 3.9 (a) corresponds to a sample obtained at T=900°C, heating rate of 10°C/min, electrical current of 10mA without annealing time, i. e., the same synthesis parameter of sample in blue curve of Fig. 3.7. Rietveld refinement used for this measurement confirm the formation of both magnetite (Fe_3O_4) and hematite (Fe_2O_3) crystal phases belonging to the *Fd-3m* and *R-3c* space group symmetry, respectively with a proportion of 70% hematite and 30% magnetite.

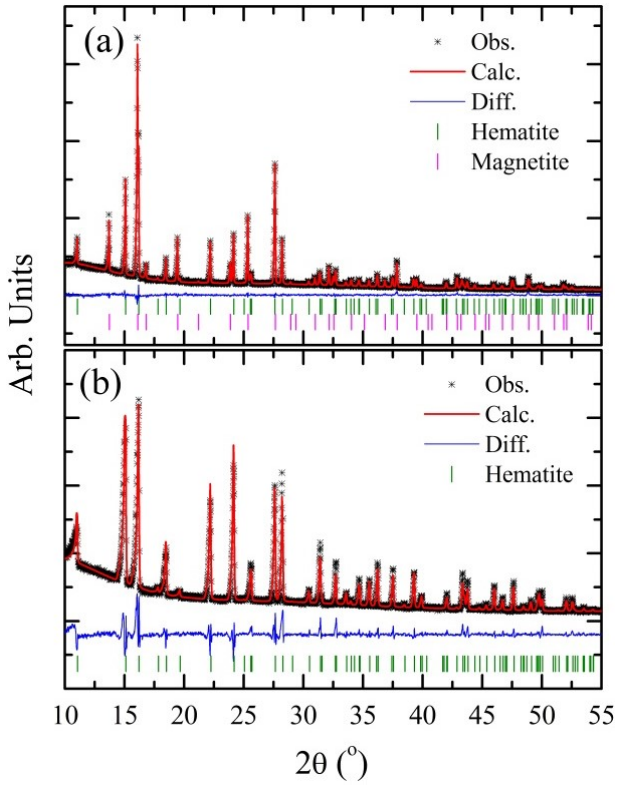

Figure 3.9: XRD measurements of microwire oxidized according to (a) curve blue from Fig.3.7 b) the same condition, but with an extra annealing time of 30 minutes at 900°C.

XRD measurements have been repeated in powdered sample obtaining the same phases. The identical two crystalline phases appear when sample is oxidized without electrical current. Moreover, if an additional time of 30 min (herein named annealing time (AT)) is included in the cycle, hematite phase dominates the oxidation process, as is shown in Figure 3.9 (b). Thus, by changing parameters such as temperature, electrical current and annealing time different fractions of magnetite and hematite crystal phases can be obtained during the oxidation process.

To follow the crystallographic phase evolution over all oxidation, we tried to reproduce the thermal treatment process through over iron wire in an *in situ* X-Ray diffraction experiment. With a heating rate of 10 °C/min, we carried out thermal treatment of the iron wire until a temperature limit of T = 900°C. A set of three temperatures were selected (T = 30 °C, T = 800 °C, and T = 900 °C) to XRD measurement. Figure 3.10 shows results obtained in this experiment with the Rietveld refinement for each case. As expected, at ambient temperature (T = 30°C) only iron phase belonging to the *Im-3m* space group is present (Figure 3.10 (a)). For T = 800°C (Figure 3.10 (b)) and T = 900°C (Figure 3.10 (c)) iron and wüstite phase belonging to the *Fm3m* space group, are observed. This is an interesting result since it is in contradiction with our previous XRD measurements made over samples where only hematite and magnetite crystallographic phases were observed.

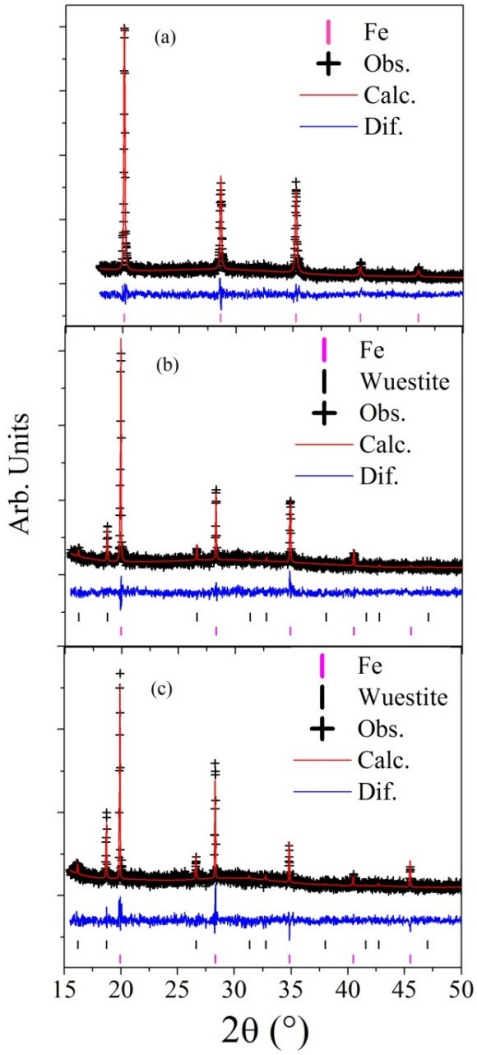

Figure 3.10: In situ x-ray diffraction patterns with Rietveld refinement of iron wire oxidized at temperature of (a) T = 30 °C, (b) 800°C, and (c) 900°C respectively.

As we said before, from the phase diagram of the iron–oxygen, above 570 ºC the phase predominantly formed is FeO (wüstite), but this formation is strongly influenced by the oxygen partial pressure present in the experiment. We believe that the fact that we executed measurements on a capillary tube supporting the iron wire influenced the oxidation process leading to wüstite (FeO) crystallographic phase formation. Magnetite/hematite phases are present in the samples of the original experiment because in this case a capillary tube was not protecting the iron wire, resulting in different oxygen partial pressure over the sample in the oxidation process.

Thus, structural analyses of obtained samples offers important information about the relation between synthesis parameter as annealing time, electrical current and heating rate with crystallographic phases formation. An interesting result from XRD analysis is that in our case volumetric fraction of both hematite and magnetite on the samples can be tuned by controlling

experimental parameters in the synthesis. As far as we know, this control of iron oxides crystallographic phases present in our samples has not been reported elsewhere.

3.1.4- Morphological and electrical transport properties

With the aim of observing the morphology of the synthesized samples, scanning electron microscopy images were obtained. Figure 3.11 shows some images of the most representative samples obtained in our work. Panel (a, b) correspond to microtubes synthetized at temperature of 750°C in a heating rate of 10°C/min, without electrical current and without annealing time. It is interesting to note that in this stage hollow structure is already formed. However, images evidence also the presence of iron metal as it is better observed on panel (b) where a metal wire is clearly distinguished in the middle of an external shell. Microtubes of panel (c) correspond to those obtained at temperature of 900°C in heating rate of 10 °C/min, without electrical current and without annealing time. It is clear the tubular structure is formed on this case. Panel (d) shows a microtube obtained by thermal treatment at temperature of 900 °C, heating rate of 10°C/min, without annealing time and without electrical current. Significant differences are not observed with microtubes of panel (c). Panel (e) shows a microtube obtained with same synthesis parameters of (d) but with an annealing time of 30 min. In this case, surface nanostructures are not observed. Panel (f) shows a microtube synthetized with the same conditions of (d) but with an electrical current of 10 mA. It is clear the regularity and high density of surface nanostructures in this case. Thus, surface of microtubes from panels (c), (d) and (e) do not show any nanostructure while in panel (f), it is possible to observe nanostructures formation, which appears in form of sticks and wires homogeneously dispersed around the microtube surface with diameters ranking from 80 nm to 300 nm and length of 1 to 5 μm.

This set of SEM images provides important information about morphology evolution of the samples according with the synthesis parameter used in each case. The first result is that below a temperature of 750°C it is observed tubular formation, but metal wire is still present in the core after thermal oxidation. The second conclusion is that temperature of 900 °C is the most suitable to obtain microtubes without the presence of metal core on the structure. Additionally, we have obtained information about the role of electrical current and annealing time over the final morphology of the microtubes which seem to have a relationship with surface nanostructure formation.

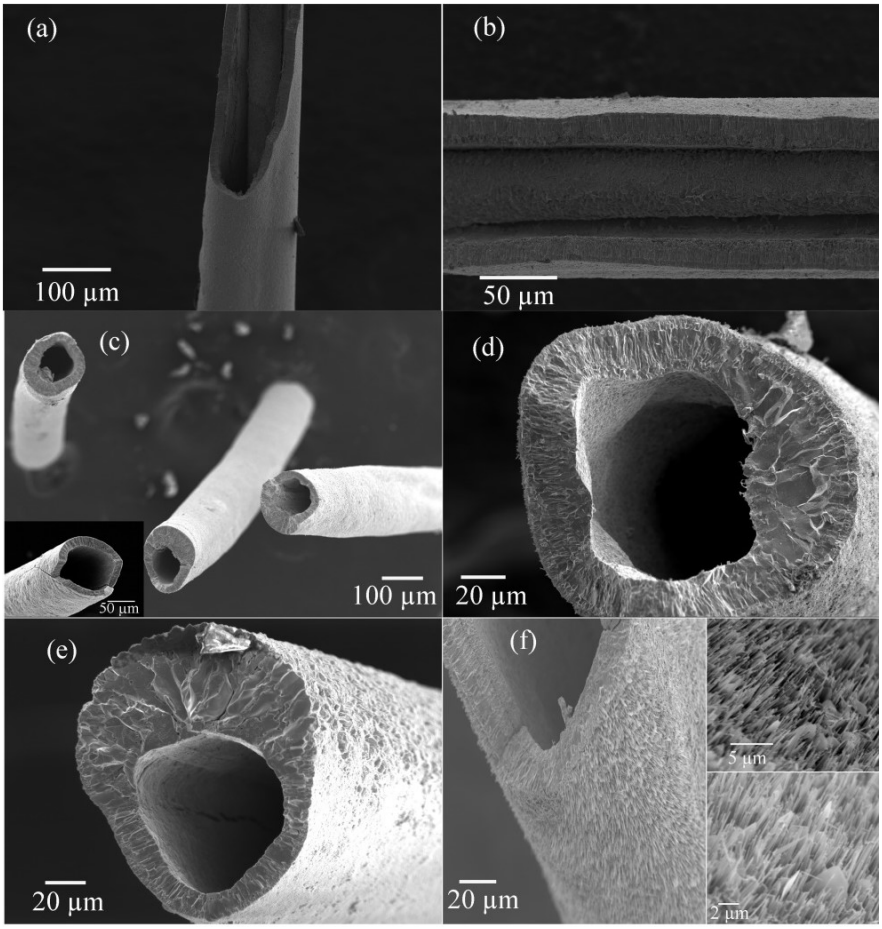

Figure 3.11: Representative SEM images of microtubes obtained with (a)(b) temperature of 750°C, (c) temperature of 900°C without electrical current, (d) temperature of 900°C without annealing time, (e) temperature of 900 °C with annealing time of 30 minutes and (f) temperature of 900 °C with electrical current and without annealing time.

For example, in one experiment made at T=600 °C with annealing time of 3 and 6 hours, nanowires grow on the surface of the core/shell structure, as can be observed in panels (a) and (b) from Figure 3.12. In this image a metallic core with an external shell decorated with nanowires is clearly observed. Here, increasing annealing time results in longer nanowires. As we had mentioned before, electrical current used initially to measure *in situ* electrical resistivity plays an important role on surface nanostructure formation, as can be observed in Figure 3.12 (c) and (d). In there, it is possible to observe microtubes obtained at temperature of 900°C, heating rate of 10°C/min, electrical current of 10mA without annealing time. On the surface of these microtubes, nanostructures grew up, which did not appear when synthesis is done over the same condition, but without any electrical current (Figure 3.11 (d)).

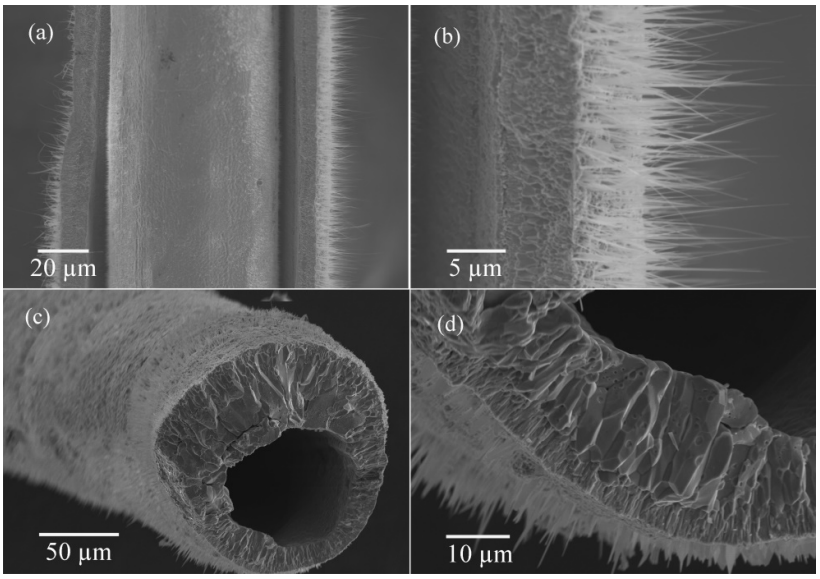

Figure 3.12: SEM images of surface nanostructures observed in thermal oxidation of iron wire with temperature of 600°C and annealing time of (a) 3 hours, and (b) 6 hours. Microtubes obtained at temperature of 900°C, electrical current of 10mA without annealing time are showed in panel (c) and (d).

As it is known, when an electric current is applied in a conductive material, part of the electrical energy is transformed into heat energy due to collisions of charge carriers with other atoms in the crystal. Another one is transformed in kinetic energy, increasing their state of agitation and temperature. When an electrical current is passed in a conductor material, the ionic diffusion referring to the two species may be affected by Joule effect or electro migration. The power produced by an electric current applied to a conductive material is given by the expression [97]:

$$P = RI^2 \tag{3.1}$$

Where the resistance is defined as $R = \frac{\rho l}{A}$ and $I = jA$, ρ is the electrical resistivity of the conductor, l is the length of the region between the electric current passage, A the cross-sectional area and j the electric current density. Replacing these relations into equation (3.1), the following expression is obtained:

$$P = j^2 \rho A l \tag{3.2}$$

When a material is exposed to high temperatures, the transfer of thermal energy is dominated by thermal radiation. The total energy of radiation per surface unit area is given by the Stefan-Boltzmann law

$$E = F\sigma A(T^4 - T_0^4) \tag{3.3}$$

where F is the emission factor, σ the Stefan-Boltzmann constant and A the surface area of the sample, T is the absolute temperature of the sample and the oven temperature T_0. For long time, the amount of radiated energy is equal to the energy dissipated by Joule effect, combining equations (3.2) to (3.3) one can obtain:

$$P = E$$

$$j^2 psl = F\sigma A(T^4 - T_0^4) \tag{3.4}$$

$$T^4 = \frac{j^2 \rho A l}{F\sigma A + T_0^4} \tag{3.5}$$

For our case, the temperature in the sample determined from equation (3.5) shows an increase of ΔT = 2 °C due to the Joule effect using a factor F ~1. At first glance the value is so small and could be neglected. Thus, despite Joule heat is not the main enhancing effect of electric current, it may have an influence on the micro/nanostructure formation because the electric field contribution, as going to be discussed in the growth mechanism section.

With the aim of studying the electrical properties of the as obtained microtubes, electrical resistivity measurements as a function of temperature were conducted. We use a four-probe method, where an electrical current of 1mA is applied on two external point contacts in the microtube and two inners contact points measured the voltage across them. Results of two microtubes are showed in Figure 3.13. We selected one microtube with high volumetric fraction of magnetite (blue line) and other with high volumetric fraction of hematite (red line). The values of electrical resistivity (ρ) were measured in the range of 30-200 °C for both microtubes. The $\rho(T)$ curves show in Fig. 3.13 indicates that both Fe_2O_3 and Fe_30_4 are typical semiconductors materials, since electrical resistivity decreases with increasing temperature. The presence of the Fe_3O_4 phase implies the presence of both Fe^{2+} and Fe^{3+} ions in the structure. Moreover, due to the absence of Fe^{2+} ions in Fe_2O_3, its charge carrier density is lower and consequently its ρ is expected to be higher than that of Fe_3O_4 at any corresponding temperature [98].

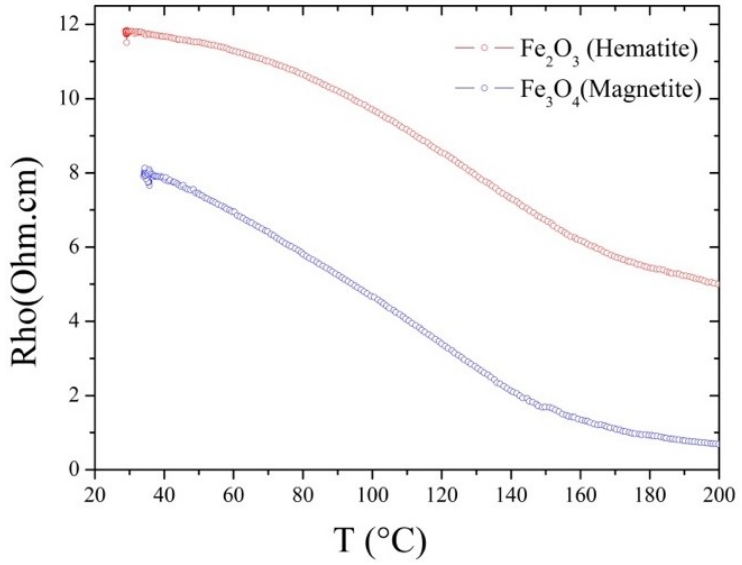

Figure 3.13: Electrical resistivity measurement of microtubes with high hematite (red line) and magnetite (blue line) volumetric fraction in the temperature range of 30-200 °C.

Different mechanisms of conduction can be explored by comparing the transport data to model predictions. Normally, when resistivity decreases exponentially with temperature, this fact would suggest that the mechanisms controlling the process are thermally activated. In that case, hopping mechanism [99] is employed.

Three electrical conductivity mechanisms are usually used to interpret the experimental data:

1. Arrhenius model. In this one, Resistivity ρ can be expressed as:

$$\rho = \rho_0 e^{\frac{E_g}{k_B T}} \tag{3.6}$$

2. The Adiabatic regime in the polaronic model. Resistivity ρ is expressed by:

$$\rho(T) = \rho_0 T e^{\frac{E_a}{k_B T}} \tag{3.7}$$

3. The Non-adiabatic regime in the polaronic model, where Resistivity ρ is given by:

$$\rho(T) = \rho_0 T^{3/2} e^{\frac{E_a}{k_B T}} \tag{3.8}$$

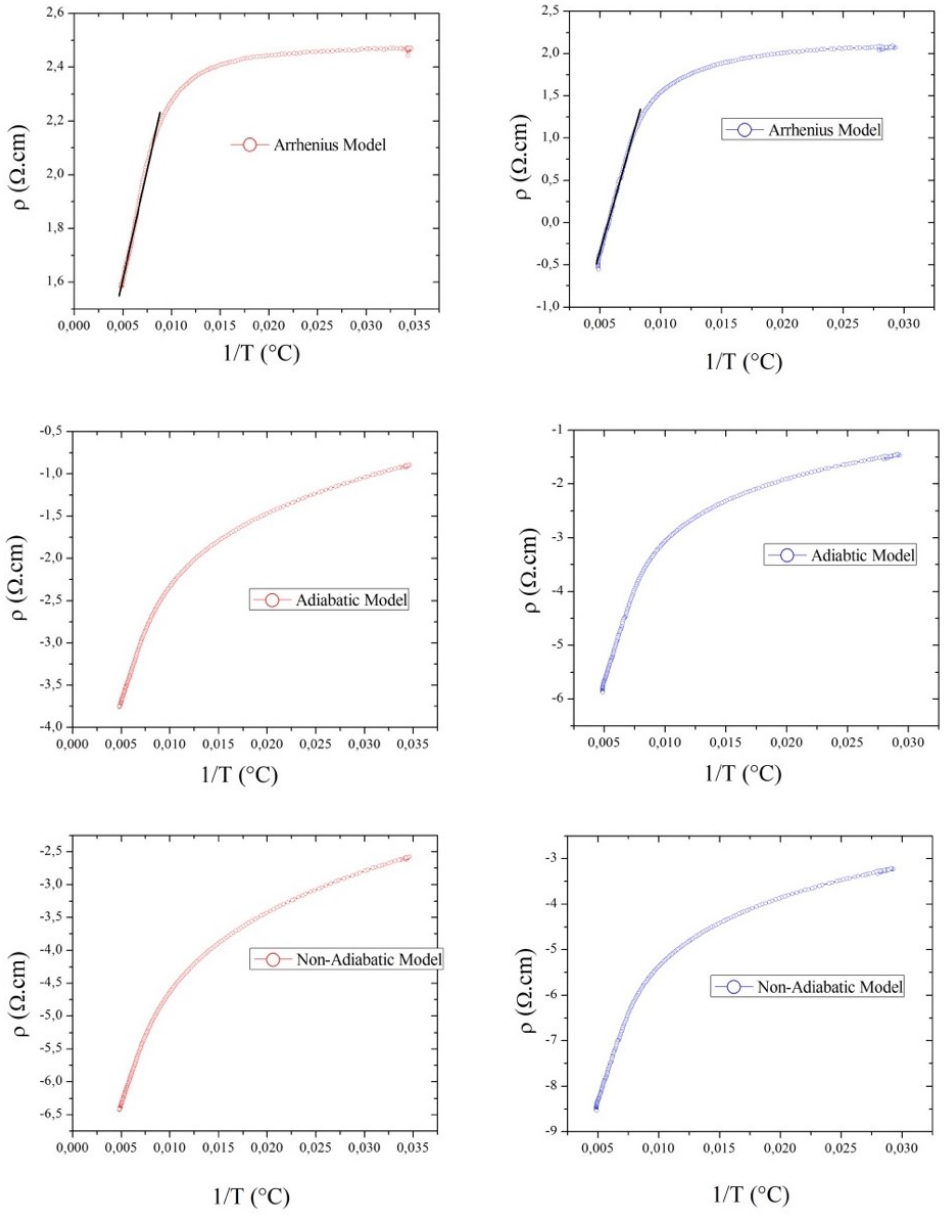

Figure 3.14: Electrical resistivity as a function of temperature fittings plots for magnetite (blue lines) and hematite (red lines) microtubes. Complete linear behavior is not observed for any model.

We have used these three models to fitting our electrical resistivity measurements of microtubes with high volumetric fraction of hematite and magnetite. Results are plotted in Fig. 3.14. For both magnetite and hematite microtubes (red and blue lines respectively) with the Arrhenius model the experimental dates show a linear behavior at the initial stage of the fitting, which indicates that this model is appropriated just for one part of the regime, i.e, for high temperatures it can be employed but it diverges in lower temperatures. This discordance may be associated with the presence of humidity in the measurements. It is well known that iron oxides are good humidity absorber [100,101] and this probably induces large variations in the electrical resistivity measurements, phenomenon that has been reported in similar works [102].

3.1.5 -Growth mechanism

Hollow microtubes and surface nanostructures formation have contributions from several factors. As it is well known, during an oxidation process the simple and well-understood steady-state diffusion of atoms is governed by Fick's law [103]. This means that diffusion of atom and vacancies are induced by the difference in atomic concentration due to chemical potential gradient. The presence of an electric field, which leads to a voltage gradient, can also contribute to the chemical potential [104]. The oxidation chemical reaction involves a process where a thin oxide layer is formed first on the metal surface, followed by simultaneous outward diffusion of metal ions through the oxide scale and inward diffusion of oxygen from the atmosphere into the core. Oxidation conditions including diffusion rates can determine the morphology of both intermediate and final product depending on the formation of voids and how they are arranged, as it was first point out by Kirkendall [105,106]. The Kirkendall experiment revealed that diffusion of substitutional lattice atoms creates defects and vacancies that facilitate atomic mobility. Condensation of vacancies can therefore give rise to void formation during the chemical reaction at interface, whose bonding strength is deteriorated in this process [107]. In the last time this effect becomes in a new synthesis route to obtain hollow micro/nanostructures of various material [108].

Ion diffusion may be also be affected by another phenomenon, known as *magnetic diffusion anomaly,* which occurs near to the Curie temperature of iron [109]. It is well know that many metallic elements undergo allotropic transformations and reveal different crystalline structures in different temperature ranges. Allotropic transitions are firts-order phase transitions, which are accompanied by abrupt changes in physical properties including diffusivity. Iron undergoes allotropic transitions from a bcc, to an fcc, and once more to a bcc structure, when the temperature varies according to the following:

$$\alpha Fe\ (bcc) \xleftrightarrow{1183\ K}\ \gamma Fe\ (fcc) \xleftrightarrow{1653\ K}\ \delta Fe\ (bcc) \xleftrightarrow{1809\ K}\ Fe\ melt$$

Magnetic phase transitions are usually second-order phase transitions. In such transitions an order parameter passes through the transition temperature in continuos manner. Second-order transitions are associated with continuous changes of physical properties. Iron has a magnetic transition from the ferromagnetic to paramagnetic state at T = 1043 K, denominated Curie temperature (T_c).

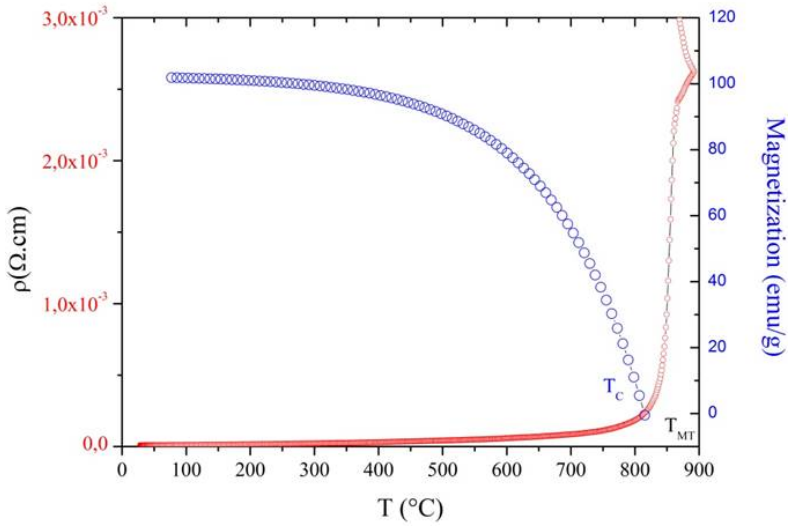

Figure 3.15: Electrical resistivity and magnetization as a funtion of temperature measurements of Fe_2O_3/Fe_3O_4 microtubes and iron wire respectively. The *temperature of morphological transformation* (T_{MT}) in this plot coincides with the Curie temperature of the iron around T = 800 ºC.

Normally, ion diffusivity measurements made in temperatures ranges below and above of the T_C of iron are used to evidence the magnetic diffusion anomaly [110]. For our case, we have observed experimental evidence of magnetic diffusion anomaly in the electrical resistivity and magnetization measurements made over the Fe_2O_3/Fe_3O_4 microtubes. By gathering these two measurements in a single graph (Fig.3.15), it is possible to observe that the temperature of morphological transformation (T_{MT}), defined previously as the temperature in which there is a robust increasing in the electrical resistivity, coincides with the Curie temperature of the iron wire used in the experiments (814 ºC). This means that transformation of metallic wire into semiconductor microtube observed in electrical resistivity measurements occurs in a temperature range where iron has a magnetic transition from ferromagnetic to paramagnetic state, which suggests that this magnetic transition plays a role in the iron diffusion.

Several works have been done studing the self-diffusion of pure iron in the α, γ and δ phases [111-112-113] as can be observed in Figure 3.16. From this figure it is evident that self-diffusion in iron is indeed a continuous function of the structural and magnetic transitions. The transition from bcc (α-Fe) to fcc (γ-Fe) is accompanied by a decrease in the diffusivity. This is in accordance with the observation that self-diffusion in fcc metals is slower than self-diffusion in bcc metals at the same temperature [39]. On the other hand, in the bcc region, below T_C, self-diffusion is slower that in the paramagnetic fcc one, which means that at temperatures a little higher than T_C, the diffusivity of iron increases because the influence of paramagnetic ordering.

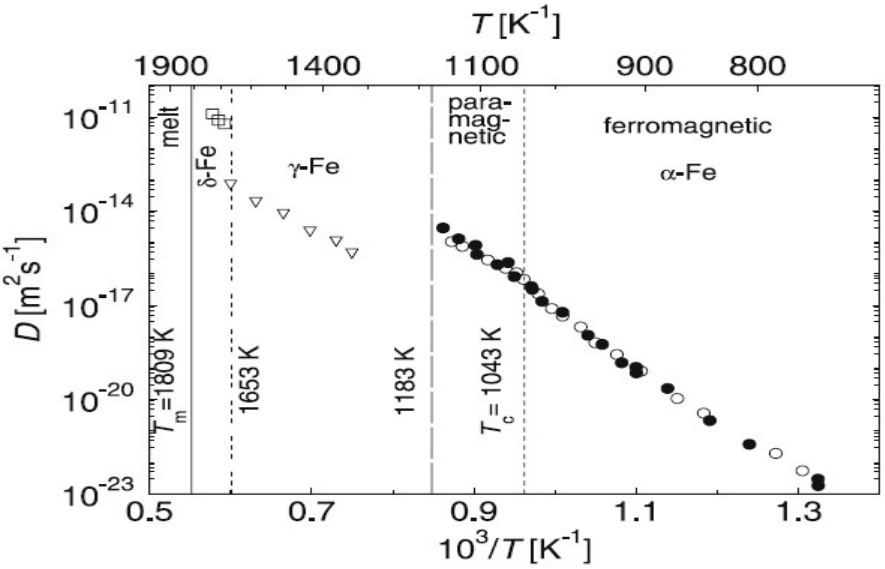

Figure 3.16: Self-diffusion in the α-, γ- and δ-phases of Fe.

The marked changes observed in the oxidation rates of certain metals and alloys in the vicinity of their second-order magnetic transition have been attributed to the change in the space charge and in the electron transfer energy at the metal/oxide interface occurring at T_c [114]. Additionally, some reports indicate that magnetic diffusion anomaly contributes to the formation and migration of vacancies [115-116]. In such cases, the increase of the free energy of vacancy formation in bcc Fe system due to magnetic spin ordering make vacancies more difficult to form in the ferromagnetic phase and lead to less vacancies being produced. Correspondingly, diffusion becomes more difficult in the magnetic ordered state than in the fully magnetic disordered one.

Thus, although the Kinkerdall efect influences in voids formation due to the larger outward Fe ion diffusion coefficient than inward oxygen ion diffusion [117] which is consistent with the smaller ionic radius of cations than anions, in our case additional contribution of the magnetic diffusion anomaly phenomena play a role in the vacancies formation. Both phenomenons are the responsible of the final hollow microtube formation. A sketch of the morphological variation from microwire to microtube is presented in Figure 3.17. In there, it can be observed how over the initial microwire (a) the influence of the Kinkerdall effect promoves creation of voids on the metallic core (b) which are high due to the role of the magnetic diffusion anomaly at temperatures near to the T_c of iron (T = 900 ºC) where iron core difunded totally and a complete hollow structured is finally formed (c).

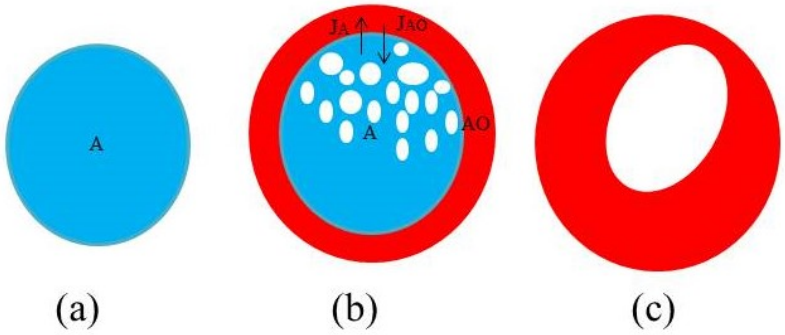

Figure 3.17: Schematic representation of hollow structure formation from the iron microwires to microtubes due to the ion diffusion mediated by Kinkerdall effect and anomaly magnetic diffusion process.

On the other hand, as we mentioned before, formation of hematite nanostructures on microtube surface is observed when electrical current is included in the oxidation process (Fig. 3.11 (f)). Nasibulin *et al* [118] have proposed a growth mechanism for iron oxide layers and subsequent nanostructures formation of on the top, synthesized through resistive heating method, which is a route where only electrical current is used. In that work, a layered-like structure formed by a sequence of $Fe/Fe_3O_4/Fe_2O_3$ followed by hematite (Fe_2O_3) nanowires on the outer layer is reported. They claim that the driving force determining the migration of ions is the potential difference appearing during the oxidation process due to electrical current. Others theoretical studies have shown that in thermal oxidation process the electrostatic potential across the bulk oxide is limited to $\sim k_BT/e$, which means that the total electrostatic potential across the oxide layer should have contributions mostly from the electric field interfaces [119].

In order to probe the layered-like structure formation of obtained microtubes, micro-Raman spectroscopy measurementens were carried out (Fig. 3.18). Three selected regions in diferent microtubes were probed: the inner layer, the outer layer, and the nanowires on the surface (green points). Figure 3.18 shows a line sketch separating hematite layer from magnetite one in three different cases: (a) where hematite layer is smaller than magnetite one, which appears when the synthesis is made at temperature of 900°C, heating rate of 10°C/min, without annelaing time and without electrical current; (b) when a microtube is produced whith high annealing time, so the hematite layer proportion increases; and (c) when nanowires are observed on the surface of the microtube, which occurs if an electrical current of 10mA is used.

The characteristic hematite Raman bands were observed at 225, 245, 292, 409, 497, 610, and 1321 cm^{-1}, whereas magnetite ones are at 298 and 663 cm^{-1} [120]. The observed Raman bands of the three different regions were all assigned to belong to hematite, as can be seen in Fig. 3.18(a)(b)(c).

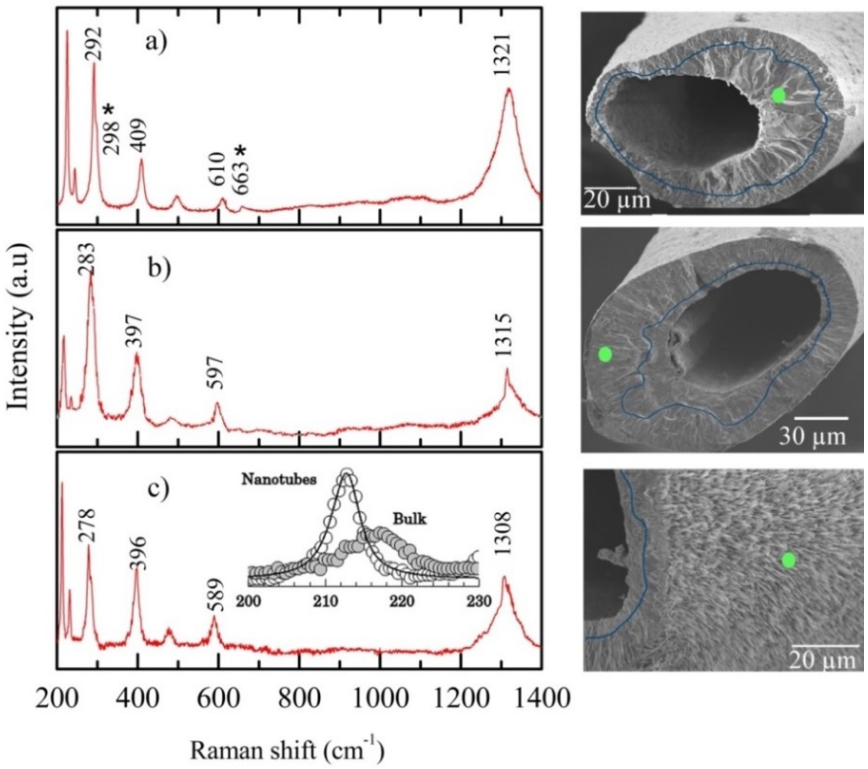

Figure 3.18: Raman spectra of the layered microtubes (a) produced without electrical current, (b) produced with high annealing time, and (c) nanowires. At right, SEM images showing the laser focus over the sample surface (green dot). The inset of c) shows the hematite nanowires 213 cm^{-1} vibrational mode fitted to the phonon confinement model (solid line), as explained in the text. The average diameter of the nanowires found from the fitting was D = 78 nm.

Interestingly, a carefull analysis on the Fig. 3.18 (a) revels the coexistence of a minority magnetite phase. It is known that bivalent iron from magnetite is easily prone to oxidation [121]. Indeed, a local oxidation of magnetite can be brought about by the laser beam during the Raman experiment [122].

The Raman spectrum of the nanostructures (Fig. 3.18 (c)) corresponds to hematite phase. However, a blue-shift and broadening of the peaks was observed compared to the microtube of Fig. 3.18 (b). This is a typical phonon confining effect that occurs as crystal domain size becomes of the order of the Brillouim zone dimension. Due to the breaking down in the quasi-momentum conservation, contributions of Γ-point induce a frequency shift and an asymmetrical broadening of the phonon modes [123]. Following the method described on references [124, 125, 126], the Raman intensity data for the 213 cm^{1} mode were fitted to the confined phonon in nanowires. The average diameter of the nanowires found from the fitting was D = 78 nm, which is near to diameter observed in SEM images of D = 90 nm. Thus, DRX and Raman measurements showed that in our experiments microtubes of Fe_3O_4/Fe_2O_3 layers with surface Fe_2O_3 nanowires has been obtained.

The absence of wüstite phase (FeO) in our experiment can be explained by the incorporation of oxygen at the outer surface of the oxide layer which generates cation vacancies that diffuse

through the oxide toward the metal. To maintain a concentration gradient for diffusion, the vacancies must be continually destroyed in some place at the oxide-metal interface, place which corresponds to the FeO layer. This process leads to nucleate pores which enlarge as the oxide layer grows. If the oxide is sufficiently plastic, it can deform under the pressure of the oxidizing atmosphere so that the pores are progressively collapsed. In spite of the relatively high plasticity of the FeO layer, scale–metal adhesion is lost and the initial porous in the inner layer of FeO are formed next to the metal. Otherwise, some degree of separation will develop between metal and oxide to hinder the transfer of metal into the oxide. The oxidation rate, therefore, is slow, the scale is thinnest at areas where separation is most effective, and the outer layer has thickened at the expense of the Fe and FeO, until achieve one point when both metal and layer are totally consumed by the diffusion process [127].

Formation of nanostructures on the microtube surface may be understood on the basis that with the application of electrical current iron ions of Fe_3O_4 (magnetite) layer diffuses more efficiently. Despite of nanostructures growth was also evidenced in the case where only thermal treatment is employed, it is important to point out that this occurred when tubular formation was not observed. For the opposite case, when microtubes were formed, surface nanostructures grew up only when electrical current was used. The oxidation process involves ion diffusion from the iron wire core to the surface through the iron oxide layers and diffusion of oxide ions in the opposite direction. At certain temperatures, grain boundaries in the Fe_3O_4 layers, likely formed due to the oxidation stress, could be responsible for higher diffusion rates compared to lattice diffusion [128]. It is worth noting that the diffusion rate is enhanced in crystal defects at elevated temperatures.

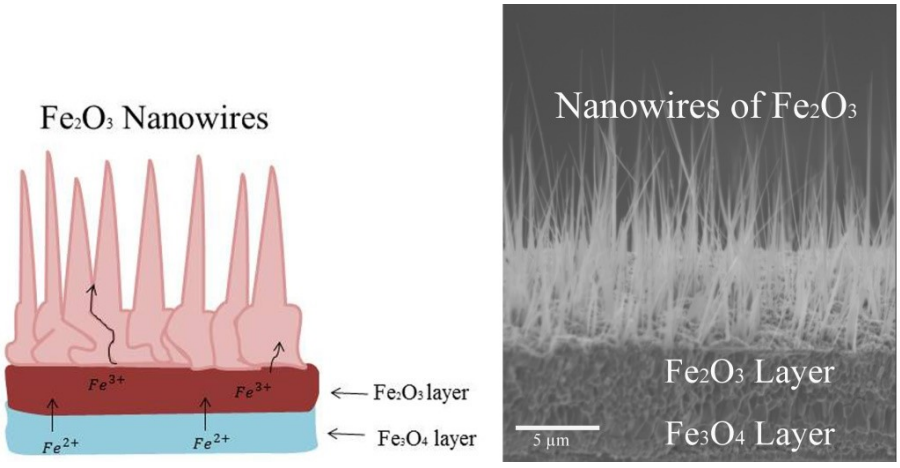

Figure 3.19: Sketch showing the path of Fe diffusion: Fe ions diffuse outward from the Fe_2O_3/Fe_3O_4 interface to the free surface via grain boundary, surface and lattice diffusion driven by the Fe_2O_3/Fe_3O_4 interfacial reaction, followed by surface diffusion from grain boundary junction areas to the nanostructure root and then to the nanostructure tip driven by the concentration gradient.

Thus, the electric field produced during resistivity measurements plus the electrical field produced during thermal heating of an iron wire, which correspond to our case, affects the ion mobility across the system and favors the regular formation of hematite nanostructures on the surface microtubes. Fig. 3.19 shows a model for the mobility path of Fe ions diffusion.

The whole formation process for our particular samples can be sumarized in three steeps as follows: first, the Kinkerdall effect and the magnetic anomaly ion diffusion produces a hollow structure with a differential volumetric fraction of both hematite (Fe_2O_3) and magnetite (Fe_3O_4); in a second steep, annealing time employed promoves the ion diffusion of magnetite layer increasing the volumetric fraction of hematite on the system. Finally, when electrical current is applied, surface nanostructures of hematite are formed by ion diffusion enhanced by the electrical field generated with the passage of electrical current. A squematic representation of this process is shown in Fig. 3.20.

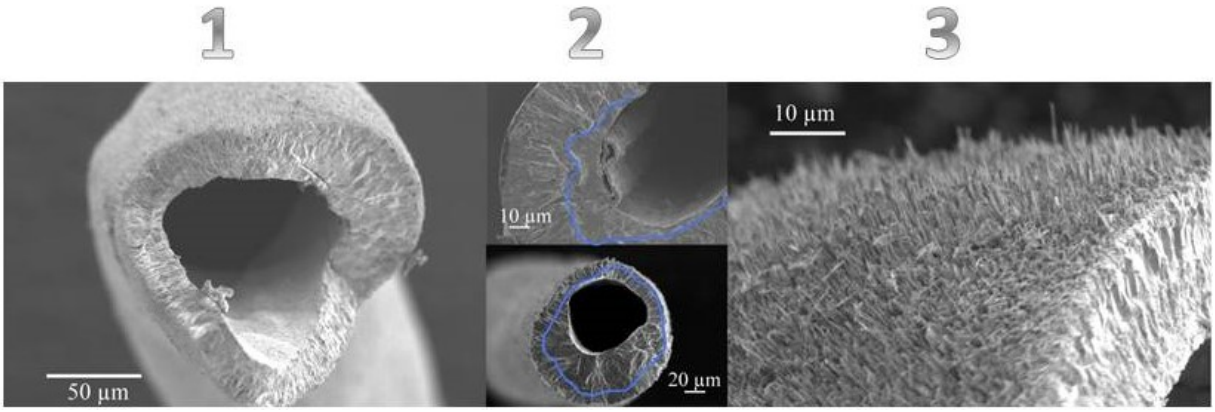

Figure 3.20: Micrograpy representation of growth mechanims steeps to obtain both hollow microtubes and surface nanostructures.

3.1.6 -Magnetic properties, magnetic actuation, and *in vitro* cellular growth

The magnetic properties of the obtained microtubes have been studied in details taking into account the experimental parameters such as set point temperature, heating rate, annealing time and electrical current. As previously observed, those synthesis parameters can influence the structural and morphological properties of microtubes and induce or not the appearance of nanowires. Zero field cooling (ZFC) and field cooling (FC) measurements have been shown in Fig. 3.21 (a, b). For ZFC, sample was first cooled from 300 K to 4 K at zero magnetic field. For FC, sample temperature increased from 4K to 300 K at a constant magnetic field of 500 Oe. Fig. 3.21 displays a set of magnetic measurements of microtubes synthetized at temperature of 900 °C, heating rate of 10°C/min and electrical current value of 10 mA without annealing time.

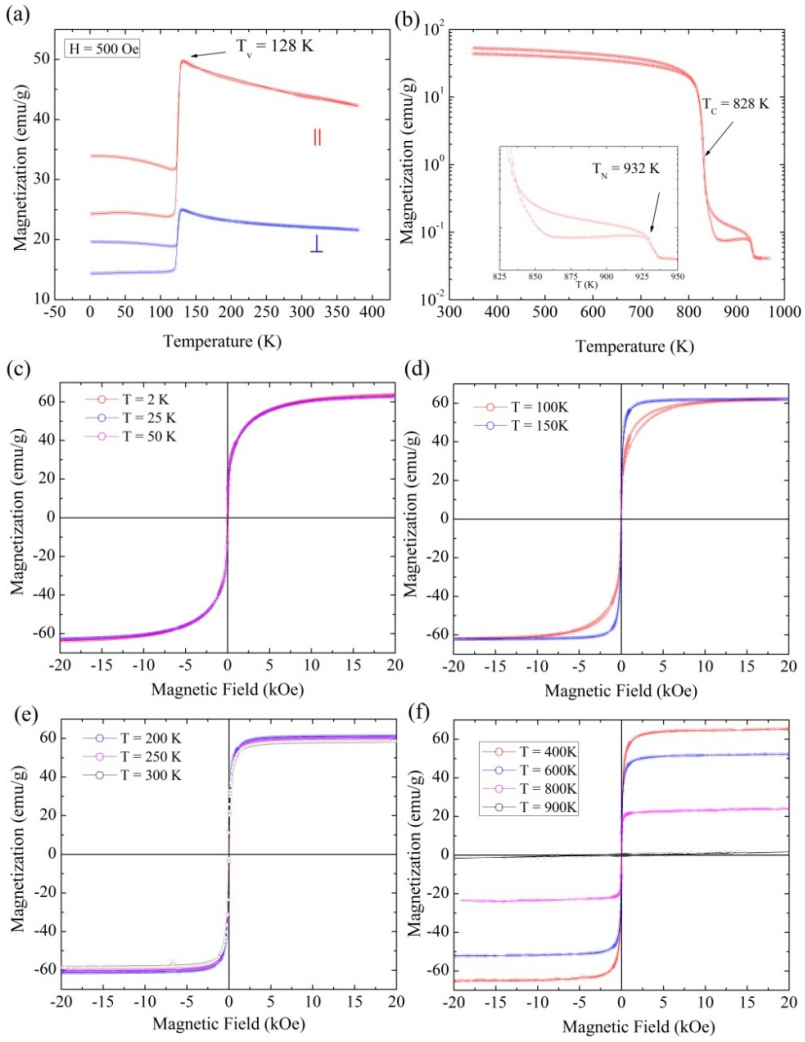

Figure 3.21: Temperature and magnetic field dependences of magnetization for the as-synthetized microtube. ZFC and FC curves show the (a) Verwey transition, and both (b) the Curie and Neel temperatures. Isothermal measurements from 2K at 300 K (c),(d),(e) does not show significant differences. The paramagnetic phase transition is evident in measurement made at T = 900 ºC (f) where the typical ferromagnetic-like behavior (red, blue, and magenta curves) goes to the paramagnetic-like one (black line).

In the Fig. 3.21 (a), one can see the well-known Verwey transition at T = 128 K, characteristic of Fe_3O_4 phase [129]. Additionally, blue line corresponding to same measurement made with a magnetic field oriented perpendicular to the sample, which shows no significant differences in this case when compared with the parallel one (red line). The magnetic moment difference between the parallel and perpendicular measurement may be due to the demagnetizing magnetic field, which induce a decreasing in the total magnetization. High temperature magnetic measurements in panel (b) show the Curie temperature for Fe_3O_4 at T = 828 K and the Neel temperature for Fe_2O_3 at T = 932K, which reveal presence of both magnetite and hematite phase in this microtube, as XRD (Fig. 3.9) measurements showed previously. The saturation magnetization for isothermal magnetic measurements from 2K to 300 K does remain almost in the same value of 60 emu/g as can be observed in panels (c), (d), and (e). Clear changes on magnetic moment value

are observed on isothermal measurements at high temperatures, panel (f), where magnetization decreases as temperature increasing, which have relation with magnetic phase transition present in the system at high temperatures corresponding to the magnetic phase transition from ferrimagnetic to paramagnetic state for the case of the magnetite (T_c = 828 K) and the antiferromagnetic to paramagnetic one for the hematite (T_N = 932K).

A second bath of microtubes synthetized with the same temperature and heating rate but with different electrical current values (1, 10 and 50 mA) was also studied. Fig. 3.22 displays magnetization as a function of magnetic field for the three samples. From these data, it is clear the inverse relation between electrical current value and magnetization; since when an electrical current of 1mA is employed the magnetization of saturation is ~ 80 emu/g, while a magnetization of saturation of ~ 40 emu/g is observed when electrical current of 50mA is used. This may indicate that electrical current induces ions diffusion and the consequent hematite formation, decreasing the magnetic moment of the sample.

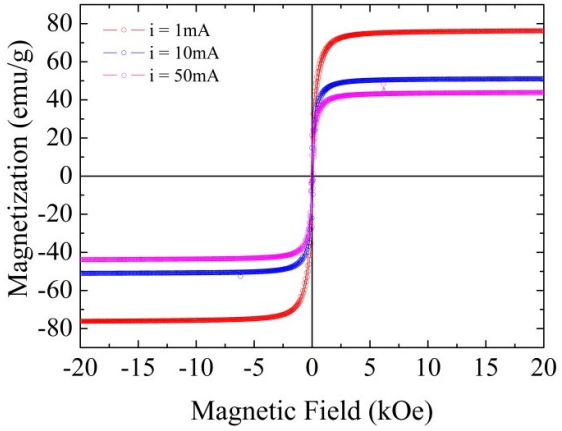

Figure 3.22: Magnetic field dependence of magnetic moment for as prepared microtube with electrical currents of 1mA, 10mA and 50mA. An inverse dependence between magnetic moment and electrical current is observed since for high electrical current values low magnetization is observed in the microtubes.

To study the magnetic properties when electrical current is absent in the synthesis, a microtube with the same synthesis parameters of the first group (T=900 °C, HR: 10°C/min) but without the application of electrical current was studied. Fig. 3.23 shows the obtained results. Saturation magnetization in this case reached a value ~ 40 emu/g, which is lower than the case when electrical current of 10mA is employed (50 emu/g).

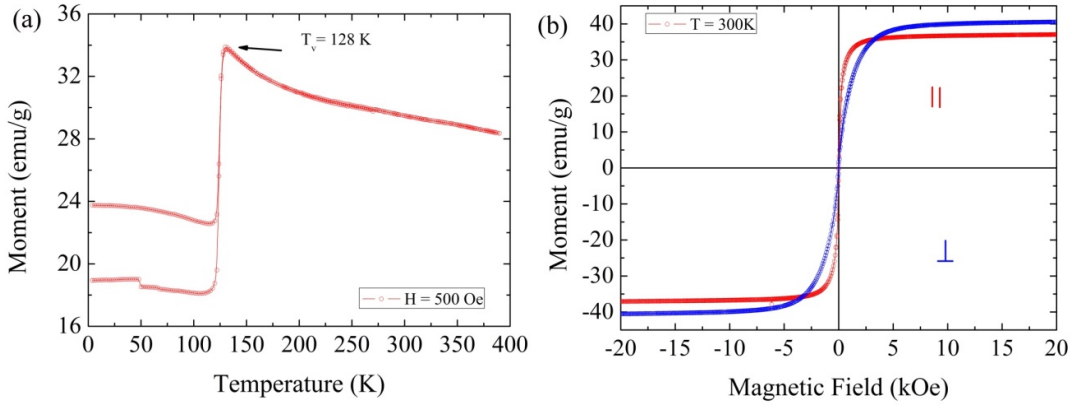

Figure 3.23: Magnetic and temperature field dependences of magnetic moment for as prepared microtube without use of electrical current. Panel (a) shows Verwey transition at T =128 K which indicates magnetite presence in the microtube. Panel (b) compares position of the sample parallel and perpendicular to the magnetic field without significant differences.

This result is very interesting because help to understand some aspects of crystallographic phases evolution on the microtubes. SEM images of microtubes obtained with electrical current (Fig. 3.11 (f)) showed that the main morphological difference with those when electrical current is not used is the surface nanostructure formation in the first case. Raman measurements confirmed that these nanostructures belong to hematite phase. Thus, decreasing in magnetic moment when no current is applied can be associated with the different layer growth of both hematite and magnetite phases induced when any electrical current is employed through the system. When electrical current is not used, a thinner magnetite layer together with a thicker hematite one is present in the microtube. Panel (a) in Fig. 3.22 confirms that magnetite phase is present in this microtube since the Verwey transition, signature of the magnetite phase, is detected in the magnetization as a function of temperature measurements.

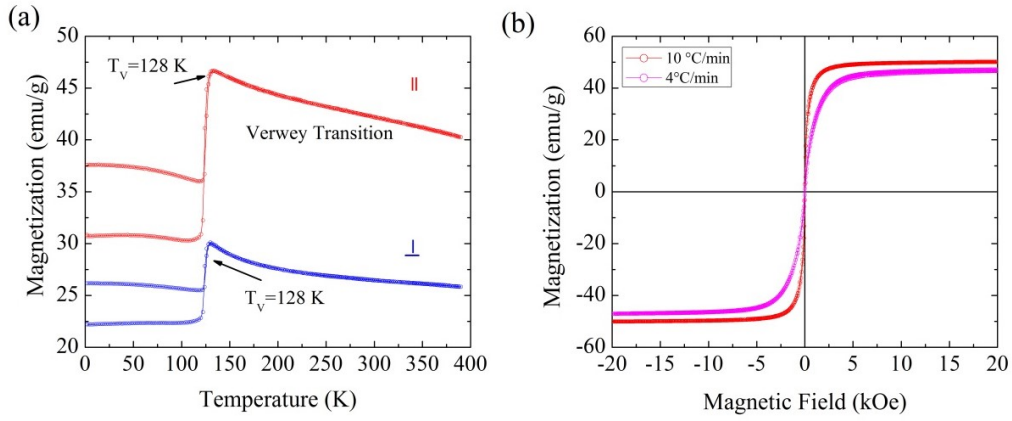

Figure 3.24: Magnetic measurements for microtubes prepared at different heating rates (a) with a rate of 10°C/min temperature as a function of magnetic moment measurement show Verwey transition at T =128 K which indicates magnetite presence in the microtube. (b) Isothermal measures of two microtubes obtained at different heating rate show a little difference in the magnetization.

Magnetic measurements of two microtubes obtained with different heating rate were also made. Figure 3.24 shows magnetic measurements for microtubes obtained at temperature of 900 °C, electrical current of 10mA, heating rates of 4 °C/min and 10 °C/min, without annealing time. Panel (a) shows that for this experiment only Verwey transition appears in the ZFC-FC curves. As can be observed in panel (b) in isothermal plots is evident a little difference in the magnetization for the two measurements, for slow heating rate a low magnetization (~40 emu/g) is observed when compared with the case of fast heating rate where is observed a high magnetization (~50 emu/g). This result is in agreement with previous electrical measurements (Fig. 3.7) which showed that fast HR produces samples with low resistivity (high magnetization) while slow HR produced microtubes with high resistivity (low magnetization).

According to SEM images and XRD measurements annealing time is a fundamental experimental parameter to hematite phase formation. To study the role of this parameter on magnetic properties of the microtubes, a set of magnetic measurements were made on a microtube synthetized at temperature of 900°C, heating rate of 10°C/min, 30 min of annealing time and without the application of electrical current. Results are plotted in figure 3.25. Panel (a) shows both Verwey and Morin transition at 128 K and 260 K, respectively. The Morin transition is a spin-flip transition where antiferromagnetic (AF) structure of Fe_2O_3 changes to weakly ferromagnetic order [130]. Thus, Morin transition is a well-known feature when exist high hematite volumetric fraction in the microtube. Panel (b) shows that for this microtube the magnetization is ~ 6 emu/g which is considerably lower than the last microtubes presented (Fig. 3.24), where no annealing time was used in the synthesis. This result confirms that, as showed previous in the DRX measurements, annealing time promotes hematite phase formation at high proportion in the microtubes.

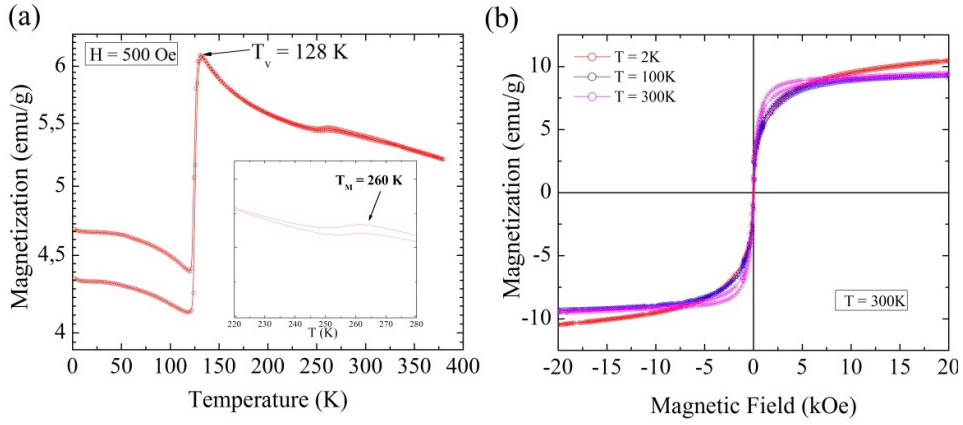

Figure 3.25: Magnetic measurements of microtube prepared with annealing time of 30 min. (a) Both Verwey and Morin transitions appear at T=128 K and T = 260K, respectively. (b) A low magnetic moment is observed in this microtube when compared with the microtube synthetized under the same conditions, but without annealing time.

Finally, we studied the influence of both electrical current and annealing time over the magnetic properties of a set of microtubes obtained at temperature of 900 ºC, heating rate of 10 ºC/min, electrical current of 10mA and annealing time of 30 min. Results are plotted in figure 3.26. Panel (a) shows both Morin (T=260 K) and Verwey (T = 128 K) transitions in the measurements, which confirms the presence of magnetite and hematite phase in the microtube. Panel (b) evidences an important feature of the microtube obtained under these experimental conditions which is the very low magnetization, ~0.6 emu/g, and the evidence of an antiferromagnetic-like behavior in the hysteresis cycle for this case. This is a strong evidence that by combining both annealing time and electrical current the hematite phase will be the predominant in the microtube, which agrees with previous SEM and DRX results when we showed that both electrical current and annealing time promotes the hematite formation, in the form of a thicker layer for the case of annealing time and as surface nanostructures for the electrical current one.

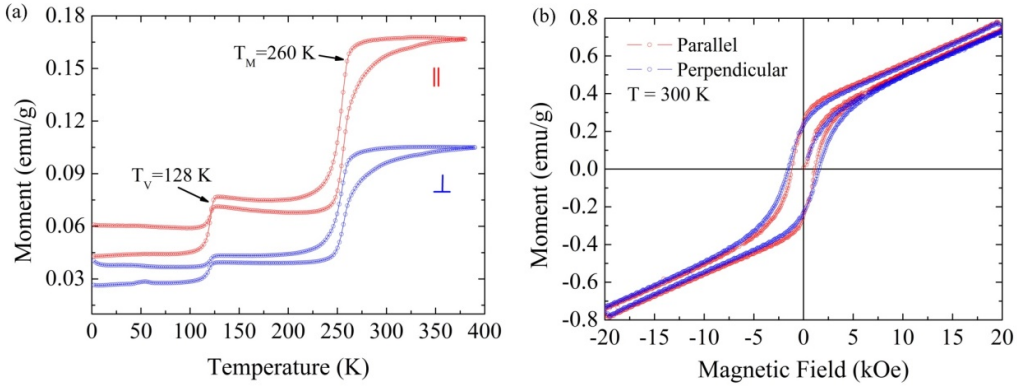

Figure 3.26: Magnetic measurements of microtube prepared with annealing time of 30 min and electrical current of 10mA (a) Both Verwey and Morin transitions appear at T=128 K and T = 260K respectively. (b) On isothermal plot a very low magnetic moment is observed in this microtube which evidences that the combination of annealing time and electrical current in the synthesis induces the hematite formation in the final sample.

In Figure 3.27 we summarize the measurements of magnetization as a function of temperature and magnetic fields (inset) for three microtubes with different volume fraction of magnetite/hematite: (a) magnetite; (b) both magnetite and hematite phases coexistence; (c) only hematite phase. In Fig. 3.27 (a), one can see the well-known Verwey transition at T = 128 K, characteristic of Fe_3O_4 compound. The saturation magnetization reaches 41.5 emu/g at low fields, see inset. Fig. 3.27 (b) shows the same measurements for the second microtube where one can see not only the Verwey transition of magnetite, but also the Morin phase transition at T = 260 K belonging to hematite. The saturation magnetization is lower reaching 9.3 emu/g. Fig. 3.27 (c) shows the presence of only Morin transition; the saturation magnetization is very low ~ 0.5 emu/g even in magnetic field as large as 20 kOe confirming hematite microtubes. Corroborating the

previous results, temperature, heating rate, and annealing time play a fundamental role turning magnetite into hematite phase. It is very interesting that by using this method one can tune in the amount of magnetite going from a ferrimagnetic (high magnetic moment) to a nonmagnetic-like (very low magnetic moment due to antiferromagnetic alignment of hematite) microtubes. To our knowledge, the synthesis and controlling of magnetic phase volume fraction in a single microtube has not been reported so far. In the panel on the right of Fig. 3.27, we show a drawing illustrating the microtube along with magnetic lines and magnetic induced field produced by each one when they are saturated.

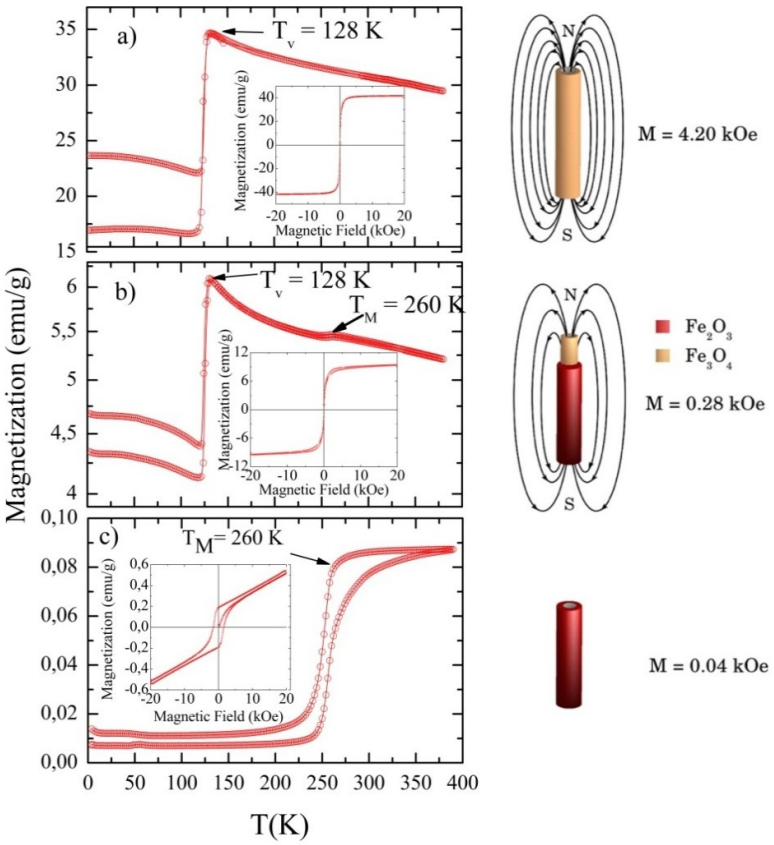

Figure 3.27: Temperature and magnetic field dependences of magnetic moment for (a) magnetite majority phase (b) magnetite/hematite, and (c) hematite microtubes. It is interesting to observe the presence of both Verwey and Morin phase transitions on the microtubes. The panel on the right illustrates the microtubes along with the magnetic induced field, produced by them when they are saturated.

Controlling the magnetic phases of microtubes may have several applications in devices driven by external magnetic actuation. Indeed, the wirelessly rotational and translational device movement can be driven by applying magnetic field gradients generated by external electromagnets. Such systems can be incorporated in micro devices for wireless magnetic manipulation with applications as local drug delivery or assistance in surgical operations. Recently, *ex vivo* testing in porcine eyes and *in vivo* in rabbit eyes, magnetic microtubes were successfully

manipulated using external magnetic fields [131]. Rotational and translational movements of the microtubes require a magnetic torque and force acting on the magnetic structure. Magnetic torque, $T_m = VM\ x\ B$, and magnetic force, $F_m = V\ (M.\nabla)B$, can be calculated using the magnetic field (B) and magnetic field gradient (∇B): V is the volume of the sample in m^3, H is the applied magnetic field in A/m and M is the magnetization of the sample in Tesla. We have calculated the magnetic torque and magnetic force for the microtubes presented in Fig. 3.27. Before, we have estimated the volume and saturation magnetic moment of these microtubes which were found to be $8.2x10^{-11}$ m^3 and 334.8 kAm^{-1}(a), $8.6x10^{-11}$ m^3 and 23.0 kAm^{-1}(b), $8.84x10^{-11}$ m^3 and 3.84 kA m^{-1}(c). Fig. 3.28 shows both torque and driving magnetic force as a function of external magnetic field gradient from $1mTm^{-1}$ up to $10mTm^{-1}$.

Also, we have used a gradient field supposing translation movement of the microtubes along the x-axis direction. By selecting a set of possible angles one can also estimate the magnetic torque. Fig. 3.27 reveals robust rotation and translation response to an external magnetic field indicating promising technological applications of these hollow microstructures in magnetic actuation - for instance, the magnetic force reaches up to 300 nN. Here, it is important to note that we simulated using low external magnetic fields (1-10 mT) and even considering these conditions both torque and magnetic force are in the same range of the results reported in literature [132].

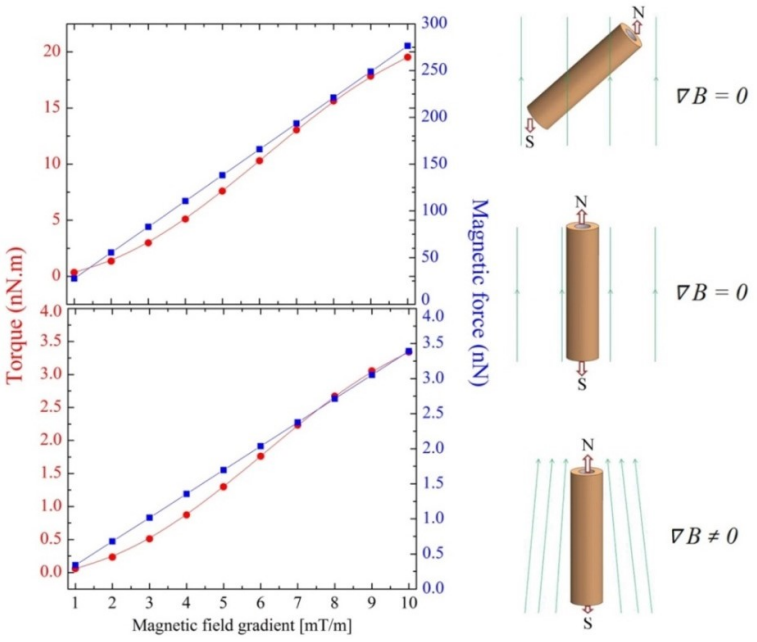

Figure 3.28: Calculated torque and magnetic force as a function of magnetic field gradient for the microtubes measured in Fig. 3.27. The panel on the right illustrates the torque and the magnetic force for the microtubes: Uniform magnetic field does not exert translational force on the microtubes. A uniform magnetic field tends to orient a microtube due to the torque. In this case, forces on north and south pole are equilibrated. A magnetic field gradient is required to exert a translational force on the microtube. A stronger magnetic force on the north pole than on the south, which is represented by the arrows.

By assuming higher values of external magnetic field (100-800 mT m^{-1}), as used in other works [133], both torque and magnetic force values for microtubes increases considerably; for example, with a gradient field of 800 mT m^{-1} ferrimagnetic microtubes would have values of T_m = 2.7x10^{-4} N.m and F_m = 8.83 x 10^{-5} N, while antiferromagnetic hematite microtubes T_m=17.2x10^{-9}N.m and F_m = 17.2x10^{-9} N.

In order to get further insights into wireless applications, we have simulated a magnetic field gradient produced by a finite solenoid (current = 1A, length = 50 mm, radius=10 mm). In Fig. 3.29 the solenoid axis is along the z-direction. The solid lines show the magnetic field gradient. After inserting the microtube in the bottom with the N-S axis along the solenoid radius direction, at initial times it rotates counterclockwise under the effect of the magnetic torque. The field gradient also exerts a force producing a linear movement along the z-axis. Controlling the current value, it is possible, for example, to equilibrate the weight of nano/microtube while keeping it levitating inside the solenoid. The acceleration acquired by a single microtube (mass = 0.6 micrograms) is also shown. At solenoid borders it could reach ~ 30 g, being a noticeable value. This could increase the terminal velocity of falling spherical particles in a viscous fluid by a 30 factor.

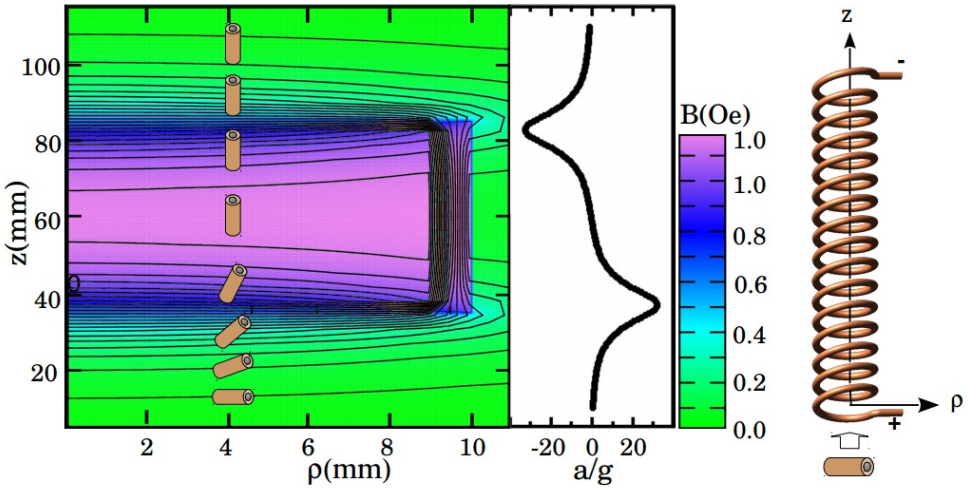

Figure 3.29: Sketch of a magnetic microtube rotating and translating movement (microtube dimensions are not in scale). Field gradient produced by a finite solenoid with length of 50 mm and radius of 10 mm and its effect on the microtube movement. The color scale shows the magnetic field intensity distribution. The solid lines are the gradient of magnetic field.

Finally, *In vitro* experiments involving adherence, migration, and proliferation of fibroblasts (3T3 NIH) cell culture on the surface of the microtubes were carry out in a collaboration with biosystem from Federal University of ABC. For that, cells were cultivated in DMEM (Dulbecco's Modified Eagle's Medium) culture medium with 2 mM L-glutamine, adjusted with sodium bicarbonate 2,2g/L and 10% fetal bovine serum. Cells were kept in incubator with temperature at 37°C and 5% of CO_2. When cells occupied approximately 80% of the culture flask area, they were

detached by enzyme action using trypsin solution 0,05% / EDTA 0,02% and amplified at the ratio 1:5 or used on sample cell adhesion test.

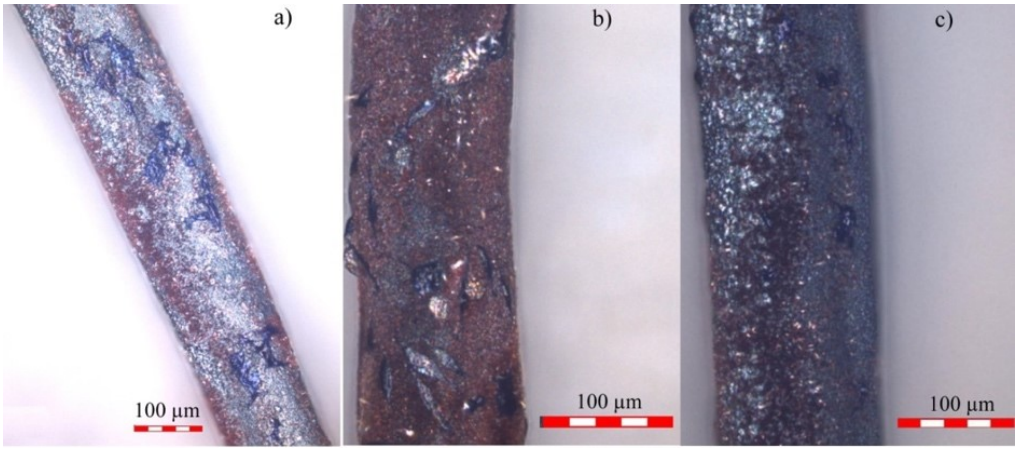

Figure 3.30: a) Hematite, b) hematite nanowires and c) magnetite sample after 3 day in culture medium. The fibroblasts colored at blue spread on surface without preference area. The pictures show that even needle shapes at the surface, the cells interacted with it, keeping alive and attached.

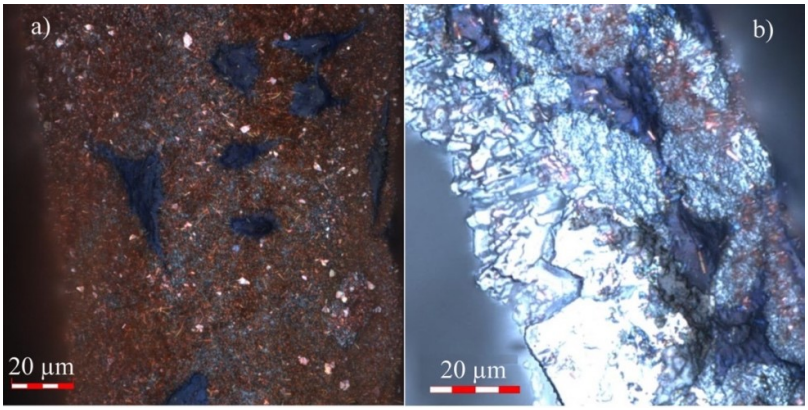

Figure 3.31: High magnification of transversal cut of a) hematite nanowires and b) hematite sample. In both cases the cell is attached at the high roughness surface**.**

The microtube surface was evaluated with confocal laser microscope before and after the cell culture assay. On the period of 3 days immersed in the culture medium and in contact with fibroblast cells no sign of morphology of topography change was observed, proving the corrosion resistance of the material. For the sample cell adhesion test, samples were sterilized by dry heat in oven, and placed on 12 well plate. Each well was seeded with $2x10^4$ cells. The plates were placed in incubator with temperature at 37°C and 5% of CO_2 for 3 days. After the incubation period samples were fixed in 4% formaldehyde buffered solution for 30 minutes, washed with water and stained with toluidine blue 0,1 % (m/v) in distilled water for 30 minutes. Samples were dried at room temperature covered from dust and evaluated with confocal laser microscope (Olympus).

Fibroblast cell adhesion was observed on the surface of all tested samples as can be observed in Fig. 3.30 and Fig. 3.31. The cell adhesion and growth on samples surface show that the material does not present cytotoxicity, because cytotoxic materials kill cells before the proper adhesion phase. Cells adhered homogeneously on samples surface without any preferred area. The highly rough surface present on the samples due to the nanowires allowed cells interaction and survival on the nano engineered topography.

3.2- Hollow SnS and ZnS micro/nano architectures

In the second part of our work, we have put an effort in the synthesis and characterization of micro and nanostructures of chalcogenides materials. A fast, inexpensive and cheap synthesis route has been studied and proposed. Finally, application on the obtained micro/nano structures in dye photodegradation was explored.

3.2.1- Synthesis of Hollow SnS and ZnS micro/nano architectures

Hollow SnS and ZnS microtube and microsphere decorated with nanostructures were synthesized with a homemade apparatus in which sulfur powder (0.1 g, 99.5% purity) and microwires of tin and zinc were placed together, separated by 10 cm of distance, into a closed tubular furnace, as shown in Figure 3.32 (a). Tubular furnace was pumped in order to prevent any contamination and then an Argon flux was established as trawling gas to carry sulfur vapor toward metallic microwires. The temperature of the furnace is raised to a defined set point temperature.

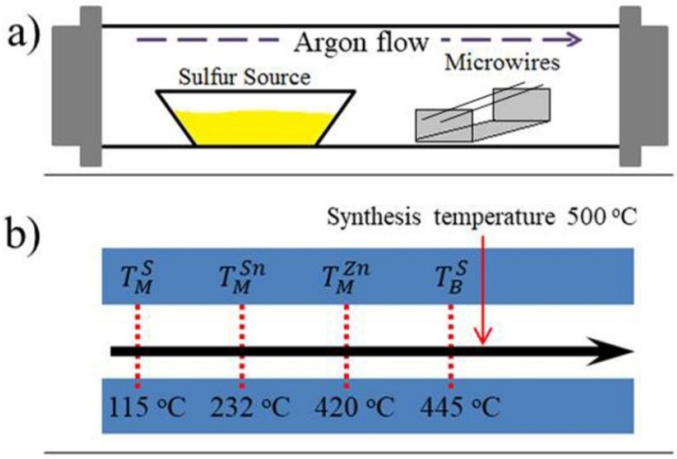

Figure 3.32: a) Sketch of experimental apparatus used for the growth of micro/nanostructures by using Sn and Zn metallic microwires and sulfur powder as precursor materials. b) Critical temperature of melting (T_M) and boiling (T_B) points of zinc, tin, and sulfur.

Taking into account the critical points shown in Figure 3.32 (b), one can see that S, Sn, and Zn undergo a phase transition to liquid state at 115, 232, and 420 ^{o}C, respectively. However, even above these temperatures, the integrity of the microwires (Sn and Zn) is preserved due to energy surface which influences the wettability and adhesion/cohesive force of the liquid metal. At T = 445 ^{o}C, sulfur boils away going to the reaction atmosphere and, at the same time, the argon flow carries the sulfur vapor to the liquid metal wire. At this temperature, sulfur vapor starts to react forming a SnS or ZnS shell on the surface of the liquid metals.

3.2.1- Structural, morphological and topological properties

Different syntheses parameters were used. Figure 3.33 shows scanning electron microscopy (SEM) images of the surface morphology in SnS samples prepared at T = 450 ºC (a), 500 ºC (b), 550 ºC (b), 600 ºC (d). It is noticeable that depending on the temperature different nanostructures grew up on the surface of the as-obtained samples and in some cases, there is no formation of them. For example, when the synthesis temperature is T= 450ºC there is formation of nanorods distributed homogeneously on the surface. But when a temperature of T = 500 ºC is used, nanorods are observed around the surface. On the other hand, for temperatures above 500 ºC there is no growth of any nanostructure, as can be observed in figure 3.33 (c) and (d), which may be associated with the coalescence of the nanostructures above these temperatures.

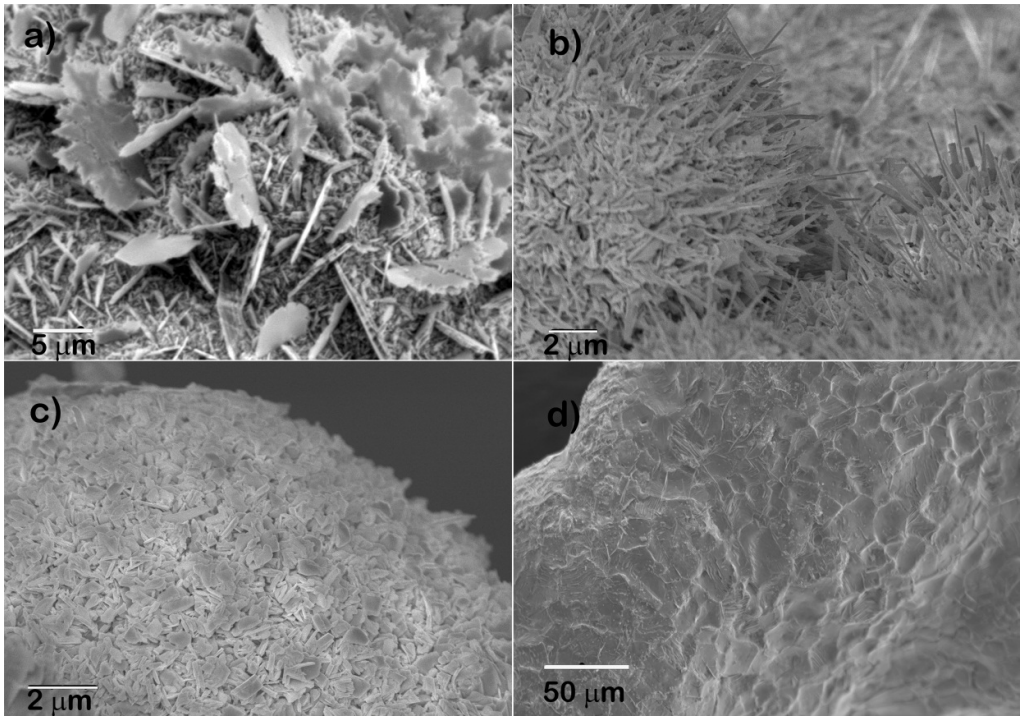

Figure 3.33: SEM images of SnS micro/nanostructures obtained with thermal treatment at a) T =450 ºC, t= 30 minutes b) T =500 ºC, t= 30 minutes, c) T =550 ºC, t= 30 minutes, d) T =600 ºC, t= 30 minutes.

In spite of temperature of T = 500ºC is the more suitable to obtain both homogenous and well distributed surface nanostructures, we selected this one as reference temperature to synthetize the samples in our work. Figure 3.34 shows representative scanning electron microscopy (SEM) images of the as-prepared sample under these experimental conditions. For this case, the metallic core of Sn is absent resulting in a hollow microstructure covered with nanostructures. In other words, a hierarchically micro/nanostructure has been formed composed by a thin metallic layer

followed by a SnS outer layer, and nanorods on the top. The nanorods are homogeneously dispersed on the surface of the tube and have average diameter of 120 nm and length up to 1 μm. The outward diffusion of Sn cations due to chemical potential gradient forming SnS layer and nanostructures consumed the metallic core which may significantly influence the evaporation process of the remaining metallic part even at low temperature.

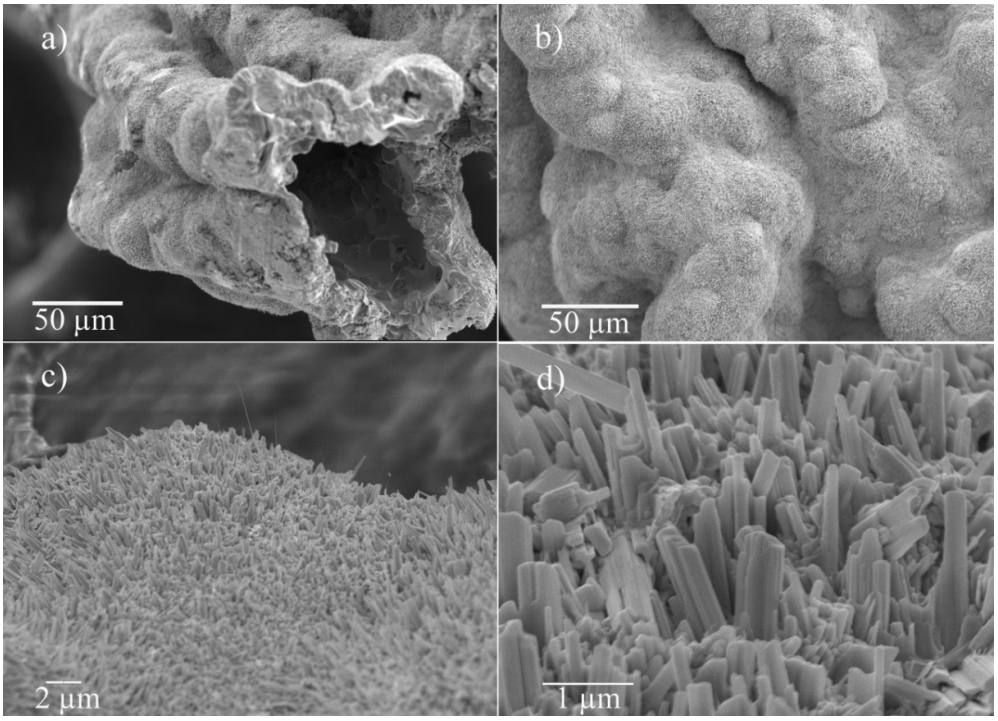

Figure 3.34: SEM images of SnS micro/nanostructures obtained with thermal treatment at T =500 ºC showing a) hollow microstructure, b, c, d) surface nanorods in different magnifications.

We have carried out an investigation about the structural phases present in SnS micro/nanostructures by X-ray diffraction, as shown in Figure 3.35. A detailed analysis of the observed Bragg reflections in XRD pattern reveals the presence of the orthorhombic SnS phase (*Pnma* space group symmetry) along with the metallic tetragonal Sn phase (*I41/Amd* space group symmetry). The manifestation of metallic phase indicates that synthesis does not consume completely the tin microwire. Following the Scherrer equation, we have estimated the crystallite size for orthorhombic SnS phase. It was found crystallite size of 31 nm for the plane (102) [134]. The inset of Figure 3.35 shows an expanded view of a Bragg plane (220) for the metallic phase. A detailed analysis reveals very narrow reflection which indicates very large crystallographic domains for the metallic phase.

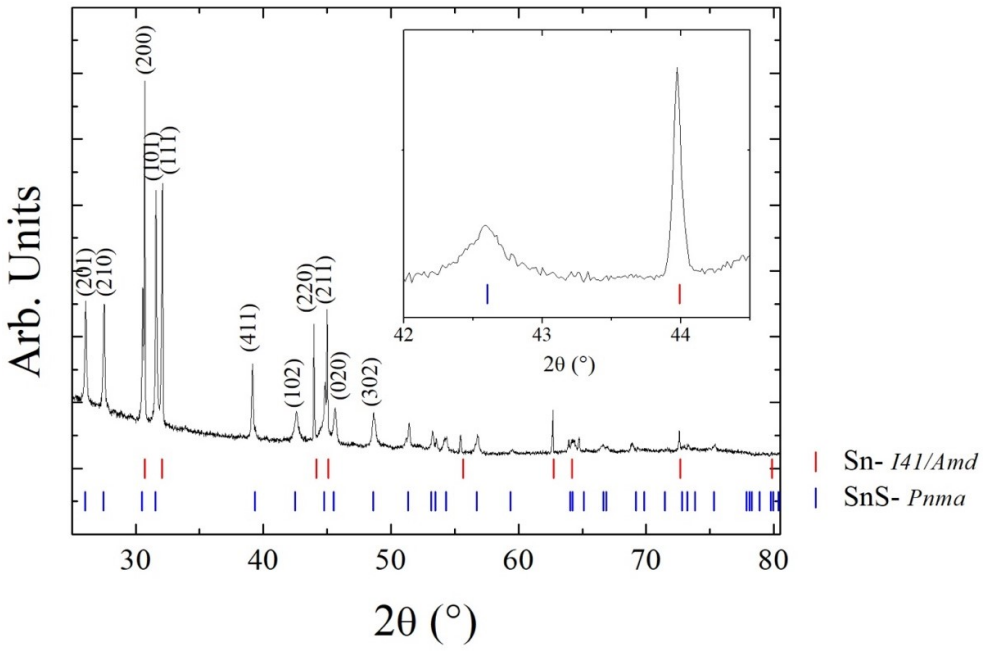

Figure 3.35: X-ray diffraction pattern for the SnS sample synthesized at 500 ^{o}C for 30 minutes. Red and blue tick marks indicate *I41/Amd* and *Pnma* space group symmetry of Sn and SnS, respectively.

In order to confirm which crystal phase belong to nanostructures, Raman spectroscopy measurementens have been done in the range from 50 to 400 cm^{-1}. Figure 3.36 exhibits the results for the SnS sample. Vibrational modes at 46, 59, 77, 109,and 229 cm^{-1} are present when the measurement was made on the microtube surface. Based on the previous report on Raman spectra of SnS single crystal, the observed Raman modes at 109 and 229cm^{-1} are assigned to Ag mode [135], 46, 77 cm^{-1} are assigned to B_2g mode, and 59 cm^{-1} is assigned to B_3g mode [136]. Previous XRD results had indicated the prescence of one phase for SnS. Acoording to our Raman measurements, we suggest the sequential formation of Sn metallic inner layer, covered with SnS (hexagonal) nanostructures.

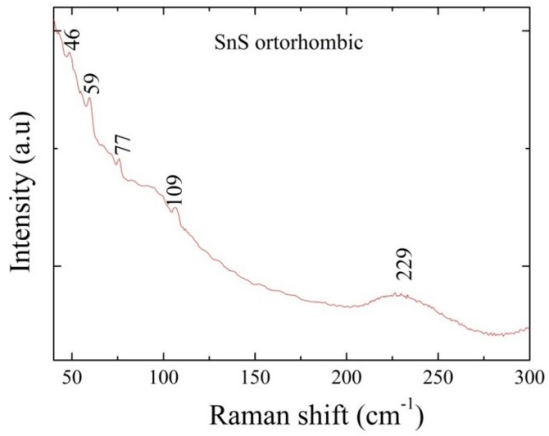

Figure 3.36: Raman spectrum obtained on the surface of SnS hollow microstructure. Five bands were observed at 46, 59, 77, 109,and 229 cm^{-1}.

On the other hand, Figure 3.37 shows representative SEM images of the ZnS sample as-synthesized at T = 500 during 30 min. It is very interesting that as one can see in Fig 3.37 (a), a hollow microsphere of ZnS is formed which is decorated with nanowires/nanoribbons. Again, even though the boiling point of the Zn (T = 907 ºC) metal is higher than the synthesis temperature, a hollow structure is formed surrounded by nanostructures (nanowires and nanosheets) in the surface, as can be observed in panel d), e) and f) from Fig. 3.37.

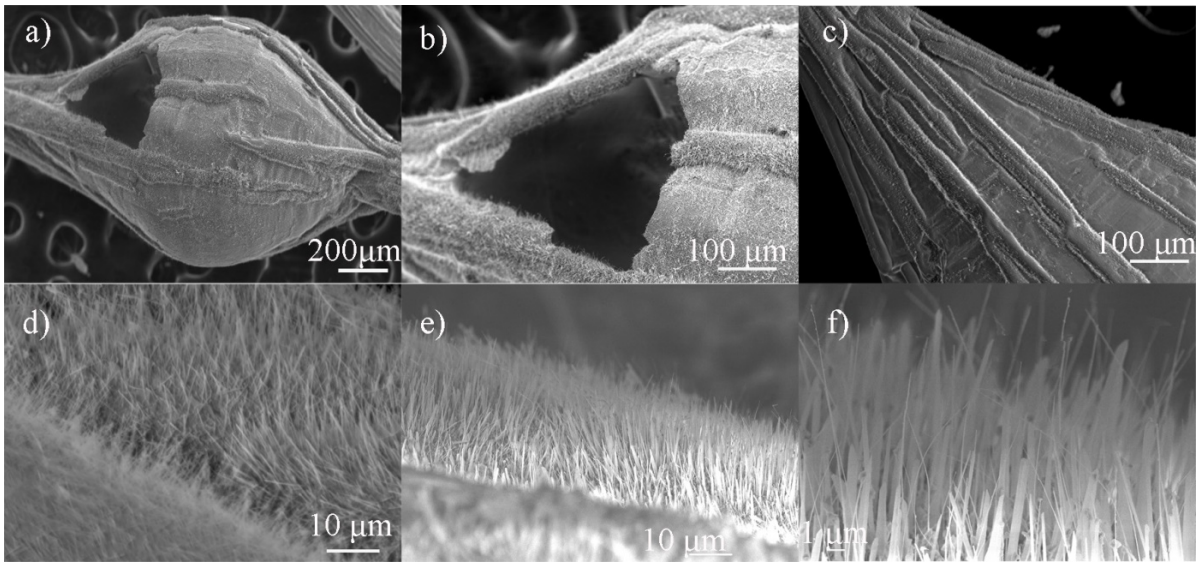

Figure 3.37: a)b)c) ZnS microsphere with nanostructures on the surface obtained with thermal treatment at T=500 ºC. d) e) f) Surface images of nanowires/nanosheets in different regions and magnifications.

For ZnS samples, significant differences are observed when compared with SnS case. While hollow microstructures were obtained with Sn, for the Zn case thermal treatment results in ZnS microspheres decorated with nanowires. The microsphere diameter is about 415 µm and nanowires have average diameter and length of 70 nm and 7 µm, respectively. X-Ray diffraction patterns of ZnS samples are shown in Figure 3.38. A careful inspection on the patterns reveals that all the Bragg plane reflections can be indexed into three different crystallographic phases: the metallic pure hexagonal Zn phase (*P63/mmc* space group symmetry) and two ZnS phases with different symmetry, ZnS cubic (*F43/m*) and ZnS hexagonal (*P63/ mc*) ones. Taking into account the width at half maximum of the Bragg reflection, one is able to estimate the size of the crystal domains by using the Scherrer equation of both phases. We have obtained 12 nm for the cubic phase (plane (103)) and 26 nm for the hexagonal crystal phase (plane (311)).

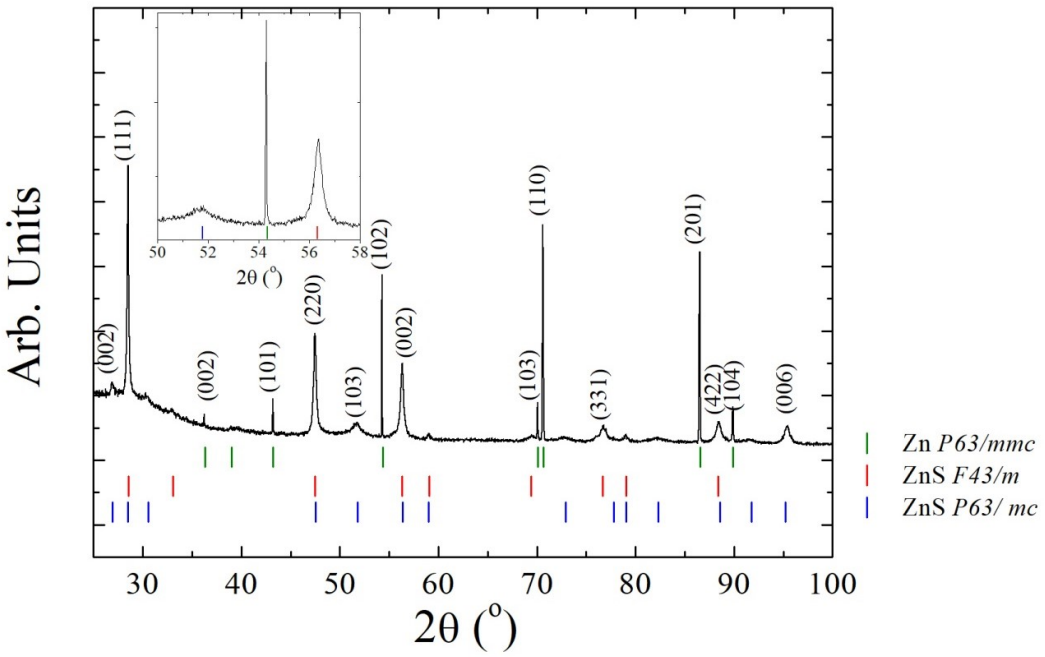

Figure 3.38: X-ray diffraction pattern of the as-obtained ZnS samples. ZnS cubic (*F43/m*) and ZnS hexagonal (*P63/mc*) phases appear in addition to pure tetragonal (*P63/mmc*) Zn metal one. The inset shows an expanded view of three Bragg reflections belonging to cubic, hexagonal, and tetragonal phases.

In order to identify which crystal phase belong to the nanostructures observed on the ZnS microsphere, Raman spectroscopy measurementens have been done on the surface in the range from 50 to 400 cm^{-1}. Figure 3.39 exhibits the results.

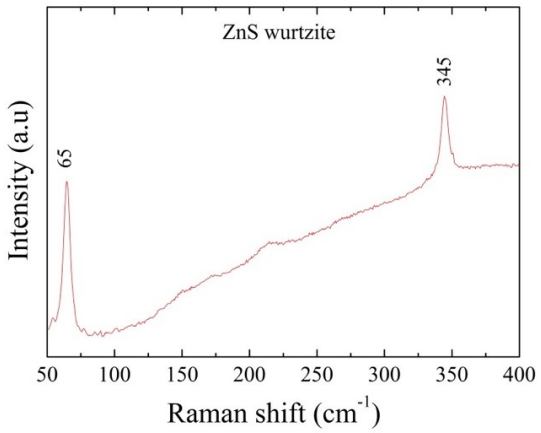

Figure 3.39**:** Raman spectrum obtained on the surface of ZnS microsphere. Two bands were observed at 65 and 345 cm^{-1}.

Vibrational modes at 65 and 345 cm^{-1} are present when the measurement was made on the microsphere surface. These peaks corresponding to 2_{Ag} vibrational mode of wurtzite structure [137]. Thus, surface nanostructures belong to hexagonal ZnS (wurtzite) phase. Previous XRD measurements had indicated the prescence of two phases for ZnS with different cristallite size. Acoording to our Raman measurements, we suggest the sequential formation of Zn metallic inner

layer, ZnS (cubic) thick layer covered with ZnS (hexagonal) nanostructures. Thus, hollow hierarchical micro/nano architectures formation from metal microwires grew up after a systematic study involving changes on temperature and annealing time.

3.2.2- Growth mechanism

The growth process is driven fundamentally by thermodynamics of the crystal phases. First, the metallic microwires go to liquid phase and at higher temperature sulfur boils off reacting with the liquid. The appearance of this spherical drop is associated with surface energy involving in the intermolecular bonds when a liquid surface is formed. In this phenomenon, the molecules on the surface have more energy compared with the molecules in the inner part of the liquid. At liquid metal–air interfaces, surface tension brings about great attraction of liquid molecules to each other due to cohesion force. As a result of the surface tension intrinsic to liquids, curved surfaces are formed in order to minimize the area. This phenomenon arises from the energetic cost of forming a surface. Therefore, the Gibbs free energy of the system is minimized when the surface is curved to form the least surface area possible [138]. Since surface tension of a liquid is a measurement of how the molecules in the liquid are able to hold on to each other it is clear its influence on the evaporation rate. Boiling points of Sn (2600 °C) and Zn (907 °C) is close related to surface tension values of Sn (750 mN/m) and Zn (551 mN/m) [139]. Additionally, outward diffusion process of cations (Zn and Sn ions) forming ZnS layer consumes the metallic core which promotes the creation of vacancies which ultimately results in a void at the center of the liquid core. This dynamical phenomenon leads to the appearance of surface due to the void formation and coalescence which also may play an important role accelerating the evaporation process of the liquid. Therefore, the formation of a sphere is due to low surface tension and the diffusion of ions creating vacancies which leads to hollow microstructure.

On the other hand, the formation of nanostructures can be understood under the self-catalytic growth mechanism [140] similarly to catalyst-free vapor–liquid–solid (VLS) process. In the self-catalytic growth, external catalyst is not introduced during the VLS growth. Therefore, the nanonuclei clusters necessary for nanostructures growth can form through internal chemical reactions. The sulfur is decomposed into sulfur vapor which precipitates in the liquid forming the layer and nanodroplets due probably to defects. The liquid droplets become supersaturated with sulfur species, forming ZnS and SnS nuclei, which act as self-catalytic sites. Subsequently, the growth of ZnS and SnS nanostructures occurs from the ZnS and SnS nuclei centers. As the reaction time goes further, the metal ion diffusion through lattice, grain boundary and surface forming ZnS layer and ZnS nanostructures. Afterwards, the amount of metal liquid in the core decreases which

can influences the vapor pressure of the liquid. At this stage, a significant amount of liquid would evaporate into the atmosphere leaving a hollow structure with a thin metal liquid layer covering its inner surface.

3.2.3- Photocatalytic activity studies

In a collaboration with Advanced materials and methods group (GMAv) from Federal University of ABC, photocatalytic property of the samples was evaluated by photodegradation of methylene blue (MB) solution under visible-light irradiation from a 450 W Xe lamp coupled with AM 1.5 G simulated sunlight (at 100 mW/cm-^{2}). Photocatalytic degradation of MB was performed by taking 2 mL of MB solution (10μM) containing 0.8 mg of catalyst under simulated sunlight irradiation for 210 min. Before the light was switched on, the systems were kept in the dark for 20 min to achieve the adsorption-desorption equilibrium. The degradation efficiency was monitored by UV–VIS spectrophotometer to record the characteristic absorption at 664 nm at certain time intervals.

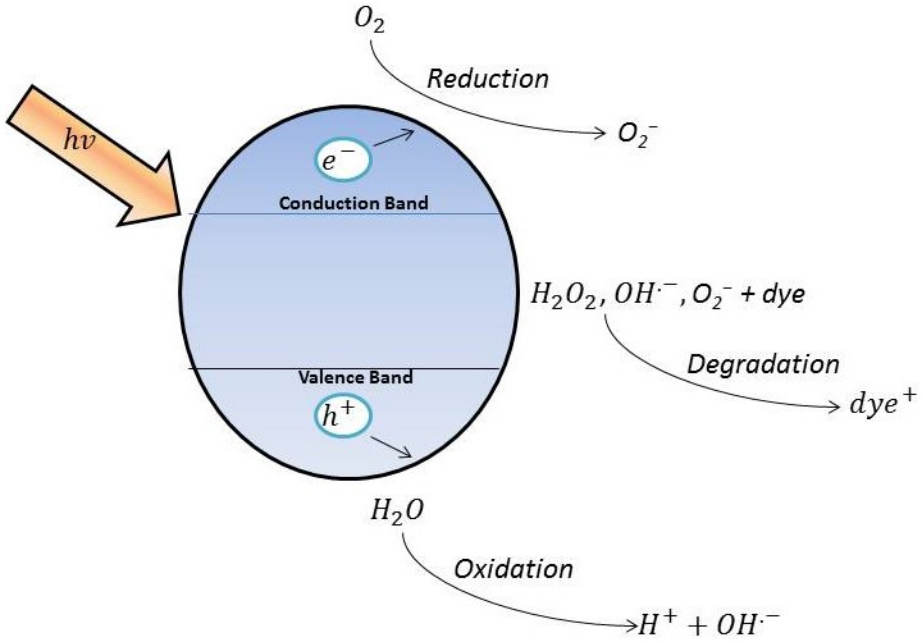

Figure 3.40: Scheme of photocatalytic dye degradation mechanism with ZnS and SnS micro/nanostructures.

The photocatalytic degradation efficiency of methylene blue under simulated sunlight irradiation monitored by UV–Vis spectroscopy as a function of time was performed by using both SnS microtubes and ZnS microspheres decorated with nanostructures. In aerated aqueous suspension, irradiated semiconductors are capable of decomposing many pollutant contaminants due to generation of electron-hole pairs which are oxidizing and reducing agents, respectively [141, 142]. The activation of ZnS and SnS nanostructures by light ($h\upsilon$) produces electron-hole pairs

which are powerful oxidizing (Zn(Sn)S + hυ → $h^+ + e^-$) and reducing agents. The oxidative and reductive reactions are expressed as $OH^- + h^+ \rightarrow {}^{\cdot}OH$ and $O_2 + e^- \rightarrow O_2^-$, respectively. These electrons can reduce the oxidants species adsorbed on catalyst surface to yield the oxidizing species such as H_2O_2, O_2^-/HO_2 and OH radicals, which are considered to be responsible for the dye degradation [143, 144]. The scheme of mechanism for photocatalytic degradation is shown in Fig. 3.40.

The photocatalytic activity of SnS nanostructures has also been reported to exhibit superficial area/porosity/shape-dependence in the photodegradation of methylene blue. Figure 3.41 (a) and (b) show the optical absorption spectra of the mixed MB dye solution and as-synthesized SnS and ZnS micro/nano structures under sunlight as a function of irradiation time, respectively. The intensity of the absorption peak of MB at 664 nm decreases with an increase in the irradiation time, which indicates that the MB molecules are degraded by the catalysis in the solution.

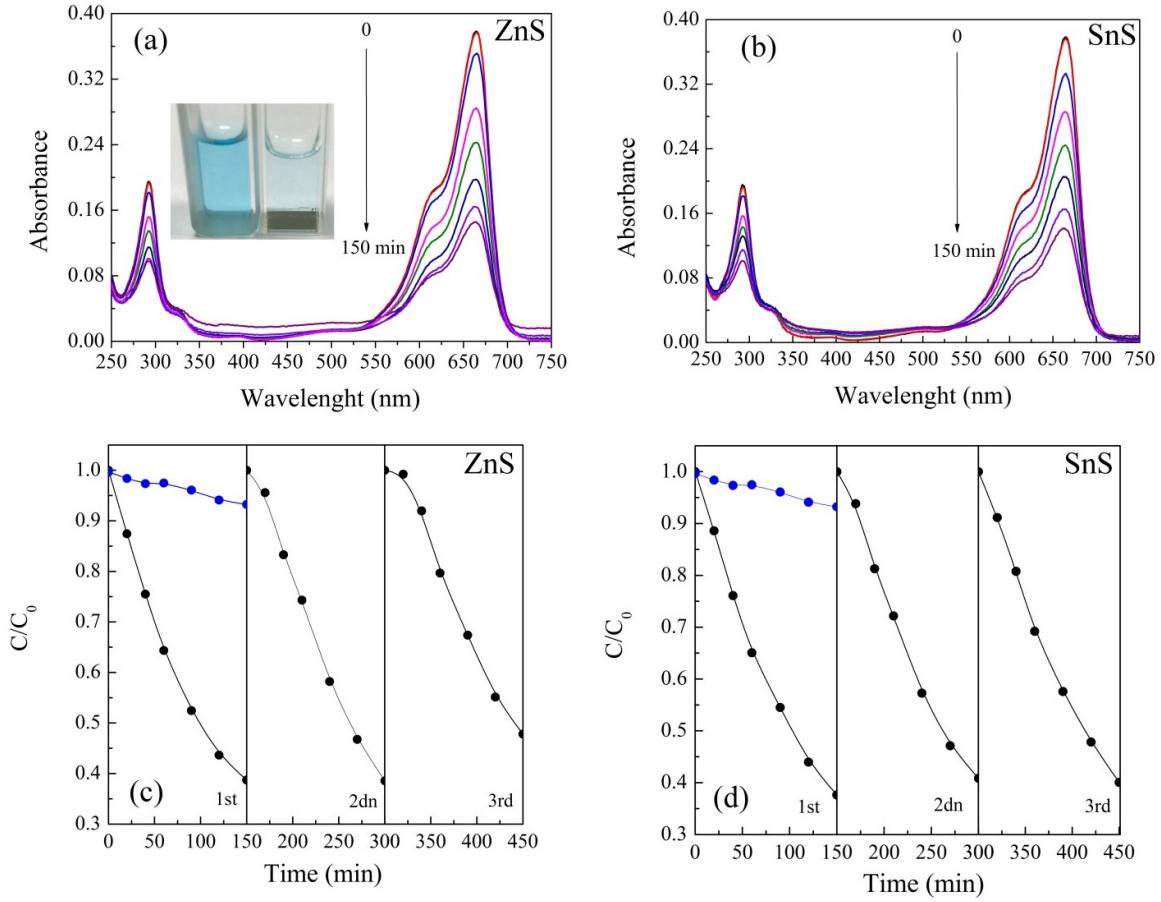

Figure 3.41: Photodegradation of MB in aqueous solution by a) ZnS and b) SnS micro/nanostructures under simulated sunlight irradiation. Recycling test of c) ZnS and d) SnS samples in photocatalytic degradation of MB.

As a consequence, the decrease of the absorbance due to decrease of dyes concentration was also observed through discoloration of MB, see inset of Figure 3.41 (a). For comparison, the blank

test (MB solution without photocatalysts under simulated sunlight) showed that MB is stable and does not decompose even after long-time illumination, see Figure 3.41 (c) e (d), black line. Fig. 3.41 (c) and Fig. 3.41 (d) show the variation of MB concentration (C/C_0) (C_0 is the initial concentration) as a function of exposure time for ZnS and SnS, respectively, under visible light irradiation.

To test the stability and reusability of the ZnS–SnS samples, cycling experiments were carried out in the photodegradation of MB under visible light. After three cycles of photodegradation, there is no significant change in the photocatalytic activity of the ZnS–SnS samples, as it is shown in Figure 3.41 (c, d), which indicated a high stability of both samples in photocatalytic reaction. The concentration of MB has decreased by almost half (48%) after 90 min for ZnS structures. In the case of SnS microtubes, after 90 min, 46% of the dye was degraded.

Since the mass of ZnS (0.1 mg) is lower than the SnS (0.3 mg) sample, it is clear that ZnS microsphere is the best candidate for photodegradation applications since similar efficiency in MB degradation was observed for both samples but in the case of ZnS the results were obtained with an amount of sample three times lower than the SnS case. The noticeable photocatalytic activity of ZnS architecture (hollow microsphere decorated with nanowires) contributes to adsorbing more dye molecules and improving catalytic efficiency. In addition, the micro/nano hierarchical architectures used here can be separated easily from the solution. Thus, the optimization of the morphology may enhance the photocatalytic efficiency.

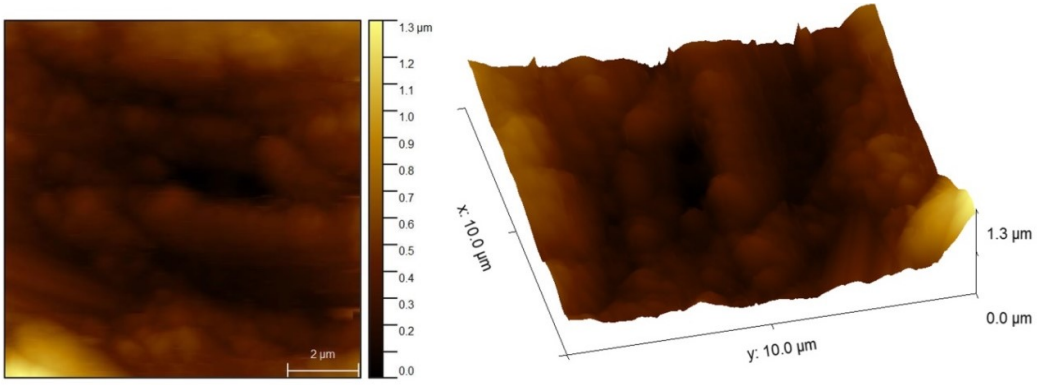

Figure 3.42: AFM topography images of SnS micro/nanostructures. For this case R_a = 133 nm and R_q = 175 nm.

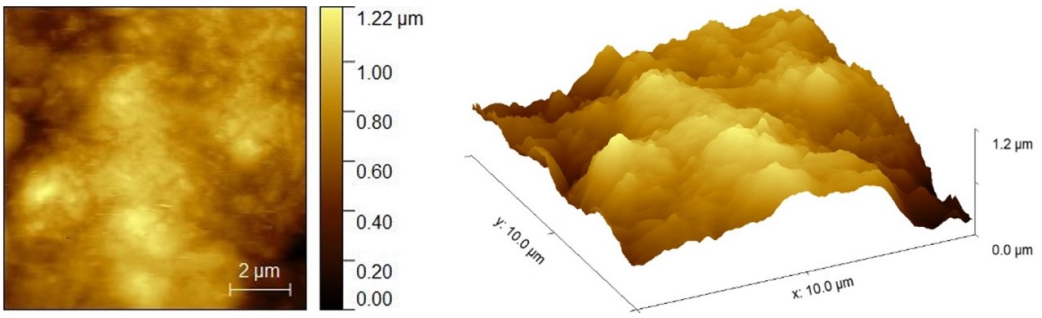

Figure 3.43: AFM topography images of ZnS micro/nanostructure. For this structure Ra = 158nm and Rq = 200 nm.

The presence of nanostructures on the surface of SnS and ZnS structures increases the surface area of the samples, which provide more accessible and highly active surfaces and could act as efficient photocatalysts. To probe it, we have done AFM measurements in contact mode of both SnS and Zns micro/nanostructures on 20 µm × 20 µm imaged surface area for each sample, as it is shown in Figures 3.42 and 3.43. Roughness analysis checked by several parameters such as mean roughness (R_a) and root mean square (R_q) show important differences between ZnS and SnS samples. For the ZnS case, both mean roughness and root mean square are higher (R_a = 158 nm, R_q = 199 nm) than SnS sample (R_a = 133 nm, R_q = 174 nm.). This confirms that ZnS sample has high surface area which produces higher adsorption capacity compared to SnS sample.

Table 3.1: A comparison of the literature with those obtained in this work for the ZnS and SnS samples.

	Mass (mg)	C_0 (MB)	Degradation MB in 90 min	Morphology
Present work ZnS	0.1	1.5 mg/L	48 %	Micro/nano hollow spheres
Ref [145]	500	5 mg/L	88 %	Micro raspberry
Ref [146]	100	10 mg/L	10 %	Nanoparticles
Ref [147]	100	10 mg/L	15 %	Nanoparticles
Present work SnS	0.3	1.5mg/L	46 %	Micro/nano hollow structures
Ref [148]	70	1.4 g/L	65 %	Nanoparticles
Ref [149]	2	10 mg/L	Complete degradation	Nanocubes
Ref [150]	125	12 mg/L	95%	Nanoribbons

We have compared the results of this work with other similar reports in the literature. This comparison has been done in terms of the mass of the catalytic material employed in each case, the amount of methylene blue used, the initial concentration of the methylene blue, the degradation of the MB in 90 minutes, and the morphology of the structure employed in each case. Results are presented in Table 3.1. Results evidence that the performance of hierarchical ZnS sample is noticeable, since even with a few amount of this catalytic material, it is achieved photodegradation efficiency of dyes similar to other reports.

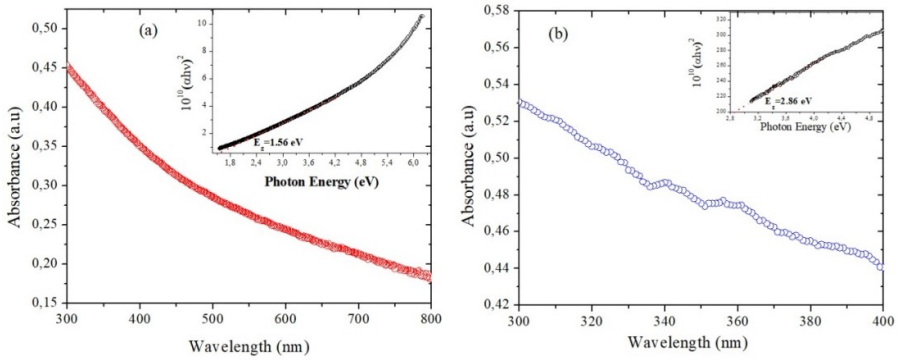

Figure 3.44: The UV-visible diffuse reflectance spectra and Tauc plot (inset) of (a) SnS and (b) ZnS samples.

The optical band gap energy (E_g) of Zns and SnS micro/nano structures was calculated by Tauc plot of $(\alpha h\nu)^2$ vs. $h\nu$. Results are shown in Fig 3.44. For ZnS case, we have observed an energy value around 2.8 eV, which is lower than the bulk electronic band gap value, 3.6 eV [151]. This observed value for ZnS sample can be attributed to the growth mechanism nature of the nanostructures which influence the physical properties of the system, here the enhancement of optical properties for photodegradation applications. We suggest that the lower energy absorption is due to both the presence of interstitial Zn species in ZnS lattice and S vacancies as structural defects. It is important to mention that in our method nanostructures are formed as a result of lattice, grain boundary and surface diffusion of cation ions from the liquid inner part to outward direction across the ZnS layer. Indeed, cation diffusion through ZnS layer also created Zn and S vacancies and interstitial species introducing energetic levels within the forbidden gap of semiconductors [152]. For example, the density of zinc vacancies can tune in luminescent properties towards visible light emission in ZnS nanostructures [153]. These ions and defects can also involve deep trap energy levels between valence and conduction bands of ZnS which also result in lower energy absorption. Therefore, the incorporation of these metallic ions in the crystal lattice may result in a shift of light absorption towards the visible light region creating electron-hole pair responsible for methylene blue degradation. For the SnS case, energy value around 1.56 eV, which is near than the bulk electronic band gap value reported in several works [154].

CHAPTER 4: CONCLUSIONS

Magnetic microtubes decorated with nanowires and cells have been obtained. The magnetic microtube synthesis process is accompanied by *in situ* electrical resistivity measurements. Microtubes of both antiferromagnetic hematite and ferrimagnetic magnetite with hematite nanowires on the surface can be obtained by controlling the set point temperature, heating rate, annealing time, and electrical current. The hollow structure formation is brought about by the difference in the diffusion coefficient of outward iron and inward oxygen ions migration which lead to the voids formation. As revealed by electrical resistivity measurements, the hollow formation takes place in a temperature window of T = 800 – 900 ºC. This simple method to fabricate magnetic microtubes and the facility to tune in the magnetic moment magnitude going from an antiferromagnetic (nonmagnetic –like) to a ferromagnetic state may bring about interesting applications. *In vitro* experiments of fibroblasts cell culture on the surface of the microtubes revealed adherence, migration, and proliferation which indicated the absence of cytotoxicity for this material. We have estimated the magnetic torque and magnetic force which reveal robust rotation and translation response to an external magnetic field confirming promising technological applications of these hollow microstructures in magnetic actuation. We believe that interesting breakthrough and new applications may be achieved by using magnetic bio microtubes in several fields. Taking advantage of the hollow structure, it is possible to build a transport mechanism of ionic fluid through it by means of Lorentz forces. Besides cells on the surface, it is also possible to think in trap inside chemical or biological agents towards drug and targeted cell delivery.

On the other hand, SnS microtubes and ZnS hollow microspheres decorated with nanostructures were synthesized in sulfatation (sulfur vapor atmosphere) conditions including temperature and annealing time by using metallic microwires and sulfur powder as starting materials. Due to surface tension, intrinsic to liquids, curved surfaces are formed in order to minimize the area resulting in microsphere in ZnS sample. For ZnS compounds, cubic and hexagonal crystals of ZnS were observed while for Sn, orthorhombic structure (SnS) appears in addition to metallic phase. The thickness and width of nanostructures are in the range of 50–300 nm for SnS and 80–400 nm for ZnS samples. Ion diffusion through lattice, grain boundary and surface can determine the morphology of both intermediate and final product. The photocatalytic activity of the ZnS and SnS samples has been investigated for the degradation of methylene blue (MB) dye under simulated sunlight irradiation. The results indicate that microspheres decorated with ZnS nanostructures are a very good candidate for photodegradation applications. The observed results demonstrate the potential of thermal evaporation process without any catalyst material as a simple, fast and efficient

route to obtain hierarchically hollow micro/nano structures of SnS and ZnS compounds with enhanced photocatalytic activity of semiconductor micro/nanoparticles under sunlight radiation.

Thus, in this PhD thesis we have developed two new synthesis methods to fabricate hollow structures in the micro/nano scale. Both fabrication routes are simple, cheap, and reproducible and they do not involve high and expensive laboratory requirements. By using them, we have fabricated successfully magnetic and semiconductor hollow structures from Fe, Zn and Sn pure metals. For all cases, nanostructures were observed on the surface of the hollow structure. These micro/nano structures were studied by using diverse characterization techniques such as SEM, DRX, Raman, AFM and SQUID which allow us to understand the physical properties of these new systems. Based in these properties, we have performed some tests to find real applications of both magnetic microtubes and hollow chalcogenides. For the magnetic microtubes adherence, migration, and proliferation of fibroblasts cell culture cell culture was satisfactorily probed which evidence that this kind of system can be utilized as wireless magnetic bio-micro robot. On the other hand, ZnS and SnS hollow semiconducting microstructures have exhibited efficient activity to degrade the methylene blue under simulated sunlight irradiation. The results reveal that ZnS microstructures have higher photoactivity to organic degradation when compared to SnS in the same time interval. The observed results demonstrate the potential of thermal evaporation process without any catalyst material to obtain hollow hierarchically micro/nano architectures of SnS and ZnS with enhanced photocatalytic activity.

REFERENCES

[1] R.S. Devan, R. A. Patil, J.H Lin, Y.R Ma, *One - Dimensional Metal - Oxide Nanostructures: Recent Developments in Synthesis, Characterization, and Applications*, Advanced functional materials, 22, 3326-3370, 2012.

[2] A. Ali, H. Zafar, M. Zia, I. Haq, A.R Phull, J.S Ali, A. Hussain, *Synthesis, characterization, applications, and challenges of iron oxide nanoparticles,* Nanotechnol Sci Appl., 9, 49–67, 2016.

[3]Xiaojing Wang, Ji Feng, Yaocai Bai, Qiao Zhang§, and Yadong Yin: *Synthesis, Properties, and Applications of Hollow Micro-/Nanostructures*, Chem. Rev., 116, 10983−11060, 2016.

[4] Caruso, F.; Caruso, R. A.; Möhwald, H. *Nanoengineering of Inorganic and Hybrid Hollow Spheres by Colloidal Templating*. Science, 282, 1111−1114, 1998

[5] R.M. Cornell, U. Schwertmann, *The Iron Oxides: Structure, Properties, Reactions occurrences and uses*, Wiley-VCH, New York, 2003.

[6] P. Hiralal, H. Unalan, K. G. U Wijayantha, A. Kursumovic, D. Jefferson, J. L. MacManus-Driscoll and G. A. J. Amaratunga**:** *Growth and process conditions of aligned and patternable films of iron(III) oxide nanowires by thermal oxidation of iron*, Nanotechnology, 19, 455608, 2008

[7] S. Sheng, W. Chao, Z. Zan, *Magnetic iron oxide nanoparticles: synthesis and surface coating techniques for biomedical applications*. Chinese Phys B; 23, 037503, 2014.

[8] A. T. Fromhold, JR., AND Earl L. Cook: *Kinetics of Oxide Film Growth on Metal Crystals: Thermal Electron Emission and Ionic Diffusion*, Physical review, 163, 3, 15,1967.

[9] M. Popescu, *Chalcogenides: Past, present, future*, Journal of Non-Crystalline Solids**,** 352 887–891, 2006.

[10] M.R Gao, Y.F Xu, J. Jianga and S. H Yu, *Nanostructured metal chalcogenides: synthesis, modification, and applications in energy conversion and storage devices*, Chem. Soc. Rev., 42, 2986-3017, 2013.

[11] C.M Liddell, C.J Summers, *Monodispersed ZnS dimers, trimers, and tetramers for lowers symmetry photonic crystal lattices*, Adv Mater.**,** 15,1715–1719, 2003.

[12] E. Schlam, *Electroluminescent Phosphors*, Proc. IEEE**,** 61, 894, 1973.

[13] J. Xu, W. Ji, *Characterization of ZnS nanoparticles prepared by new route,* J. Mater. Sci. Lett.**,** 18, 115-119, 1999.

[14] L. Sun, C. Liu, C. Liao, C. Yan, *ZnS nanoparticles doped with Cu(I) by controlling coordination and precipitation in aqueous solution*, J. Mater. Chem.**,** 9,1655-1670, 1999.

[15] C. Liang, Y. Shimizu, T. Sasaki, H. Umehara, and N. Koshizaki, *Au-Mediated Growth of Wurtzite ZnS Nanobelts, Nanosheets, and Nanorods via Thermal Evaporation*, J. Phys. Chem. B**,** 108, 9728-9733, 2004.

[16] C. Lan, J. Gong, Y. Jiang, Y. Songa and S. Yang, *Controlled synthesis of ZnS nanocombs by self-evaporation using ZnS nanobelts as source and substrates*, Cryst. Eng. Comm.**,** 14, 708-711, 2012.

[17] X.S Fang, C.H Ye, X.S Peng, Y.H Wang, Y.C Wu, L.D Zhang, *Large-scale synthesis of ZnS nanosheets by the evaporation of ZnS nanopowders*, Journal of Crystal Growth**,** 263, 263–268,

2004.

[18] S. R. Suryawanshi, S.S. Warule, S.S. Patil, K.R. Patil, and M.A. More, *Vapor−Liquid−Solid Growth of One-Dimensional Tin Sulfide (SnS) Nanostructures with Promising Field Emission Behavior*, ACS Appl. Mater. Interfaces, 6, 2018−2025, 2014.

[19] G. H. Yue, L. S. Wang, X. Wang, Y. Z. Chen, D. L. Peng, *Characterization and Optical Properties of the Single Crystalline SnS Nanowire Arrays*, Nanoscale Res. Lett., 4, 359−363, 2009.

[20] Z. Deng, D. Cao, J. He, S. Lin, S. M. Lindsay, Y. Liu, *Solution Synthesis of Ultrathin Single-Crystalline SnS Nanoribbons for Photodetectors via Phase Transition and Surface Processing*, ACS Nano, 6, 6197−6207, 2012.

[21] G. Radovsky, R. Popovitz-Biro, M. Staiger, K. Gartsman, C. Thomsen, T. Lorenz, G. Seifert, R. Tenne, *Synthesis of Copious Amounts of SnS_2 and SnS_2/SnS Nanotubes with Ordered Superstructures,* Chem., Int. Ed. Engl., 50, 12316−12320, 2011.

[22] J. Lu, C. Nan, L. Li, Q. Peng, Y. Li, *Flexible SnS nanobelts: Facile synthesis, formation mechanism and application in Li-ion batteries*, Nano Res., 6, 55−64, 2012.

[23] Y. Wu and P. Yang, *Direct Observation of Vapor-Liquid-Solid Nanowire Growth*, J. Am. Chem. Soc., 123, 3165-3166, 2001.

[24] F.C. Frank and J.H. van der Merwe, *One-dimensional dislocations*. Proceedings of the Royal Society of London Series a-Mathematical and Physical Sciences, 198, 1949.

[25] C. Jiang, W. Zhang, G. Zou, W. Yu, Y. Qian, *Hydrothermal synthesis and characterization of ZnS microspheres and hollow nanospheres*, Materials Chemistry and Physics, 103, 24–27, 2007.

[26] S. Biswas and S. Kar, *Fabrication of ZnS nanoparticles and nanorods with cubic and hexagonal crystal structures: a simple solvothermal approach*, Nanotechnology, 19, 045710-045715, 2008.

[27] B. D. Yao, Y. F. Chan, and N. Wang, *Formation of ZnO nanostructures by a simple way of thermal evaporation*, Appl. Phys. Lett., 81, 757-762, 2002.

[28] Edgar González, Jordi Arbiol,Víctor F. Puntes: *Carving at the Nanoscale: Sequential Galvanic Exchange and Kirkendall Growth at Room Temperature*, Science, 334, 9, 2011.

[29] Lou, X. W. D.; Archer, L. A.; Yang, Z.: *Hollow Micro-/ Nanostructures: Synthesis and Applications*. Adv. Mater., 20, 3987−4019, 2008.

[30] F. Caruso, R. A Caruso, H. Möhwald, *Nanoengineering of Inorganic and Hybrid Hollow Spheres by Colloidal Templating,* Science, 282, 1111-1114, 1998.

[31] R.A. Caruso, A. Susha, and F. Caruso: *Multilayered Titania, Silica, and Laponite Nanoparticle Coatings on Polystyrene Colloidal Templates and Resulting Inorganic Hollow Spheres*, Chem. Mater., , 13, 400–409, 2001.

[32] X. Fan, Z. Zhang, G. Li, N. A Rowson, *Attachment of solid particles to air bubbles in surfactant-free aqueous solutions*, Chem. Eng. Sci., 59, 2639−2645, 2004.

[33] M. Hu, A. A Belik, M. Imura, Y. Yamauchi, *Tailored Design of Multiple Nanoarchitectures in Metal-Cyanide Hybrid Coordination Polymers*, J. Am. Chem. Soc., 135, 384−391, 2013.

[34] F. H. Chen, L.M. Zhang, Q.T. Chen,Y. Zhang, Z. J. Zhang, *Synthesis of a novel magnetic drug*

delivery system composed of doxorubicin-conjugated Fe3O4 nanoparticle cores and a PEGfunctionalized porous silica shell. Chem. Commun., 46, 8633− 8635, 2010**.**

[35] C.C Huang, W. Huang, C.S. Yeh, *Shell-by-shell synthesis of multi-shelled mesoporous silica nanospheres for optical imaging and drug delivery*. Biomaterials 2011, 32, 556−564.

[36] Bryan D. Anderson and Joseph B. Tracy: *Nanoparticle conversion chemistry: Kirkendall effect, galvanic exchange, and anion exchange*, Nanoscale, 6, 12195, 2014.

[37] J. Aleman, A.V. Chadwick, J. He, M. Hess, K. Horie, R.G. Jones, P. Kratochvil, I. Meisel, I. Mita, G. Moad, *Definitions of terms relating to the structure and processing of sols, gels, networks, and inorganic-organic hybrid materials (IUPAC Recommendations 2007).* Pure Appl. Chem.,79, 1801−1827, 2007.

[38] Y. Sun, B. T. Mayers, Y. Xia, *Template-Engaged Replacement Reaction: A One-Step Approach to the Large-Scale Synthesis of Metal Nanostructures with Hollow Interiors*. Nano Lett., 2, 481−485, 2002**.**

[39] Helmut Mehrer: *Diffusion in Solids Fundamentals,Methods,Materials*, Diffusion-Controlled Processes, Springer-Verlag Berlin Heidelberg 2007.

[40] H. Teichler, *Structural dynamics on the μs scale in molecular-dynamics simulated, deeply undercooled, glass-forming* $Ni_{0.5}Zr_{0.5}$, J. Non-cryst. Solids 293, 339, 2001.

[41] AD Smigelskas, EO Kirkendall, *Zinc diffusion in alpha brass* , Trans. Aime, 1947.

[42] Y. Yin, R. M. Rioux, C.K. Erdonmez, S. Hughes, G.A. Somorjai, A. Alivisatos: *Formation of Hollow Nanocrystals Through the Nanoscale Kirkendall Effect*, Science, 304,30, 2004.

[43] CH Bernard Ng, H Tan, WY Fan: *Formation of* Ag_2Se *nanotubes and dendrite-like structures from UV irradiation of a* CSe_2*/Ag colloidal solution*. Langmuir 22, 9712 9717, 2006.

[44] Y. Ma, K. Huo, Q. Wu, Y. Lu, Y. Hu, Z. Hu and Y. Chen: *Self-templated synthesis of polycrystalline hollow aluminium nitride nanospheres*. J. Mater. Chem. 16, 2834–2838, 2006.

[45] J Zheng, X. Song, Y. Zhang, Y. Li, X. Li, Y. Pu.: *Nanosized aluminum nitride hollow spheres formed through a self-templating solid-gas interface reaction*. J. Solid State Chem. 180, 276-283 2007.

[46] R. Nakamuraa, D. Tokozakura, and H. Nakajima: *Hollow oxide formation by oxidation of Al and Cu nanoparticles*. J. Appl. Phys. 101, 074303, 2007.

[47] Q Li, RM Penner.: *Photoconductive cadmium sulfide hemicylindrical shell nanowire ensembles*. Nano. Lett. 5,1720–1725, 2005.

[48] Y Chang, ML Lye, HC Zeng: *Large-Scale Synthesis of High-Quality Ultralong Copper Nanowires*. Langmuir, 21, 3746-3748, 2005**.**

[49] X. Chen, Z. Zhang, Z. Qiu, C. Shi, X. Li: *Hydrothermal fabrication and characterization of polycrystalline linneite* (Co_3S_4) *nanotubes based on the Kirkendall effect*. J. Colloid Interface Sci. 308, 271–275, 2007.

[50] J Gao, B Zhang, X Zhang, B Xu: *Magnetic-dipolar-interaction-induced self-assembly affords wires of hollow nanocrystals of cobalt selenide*. Angew. Chem. Int. Ed. 45, 1220–1223, 2006.

[51] N.H Chou, R.E Schaak: *A library of single-crystal metal-tin nanorods: using diffusion as a tool*

for controlling the morphology of intermetallic nanocrystals. Chem. Mater. 20, 2081–2085, 2008.

[52] R. Nakamura, D. Tokozakura: *Shrinking of hollow Cu_2O and NiO nanoparticles at high temperatures*. Acta Mater. 56, 5276–5284, 2008.

[53] Q.Wang, J.X. Li, G.D Li, X.J Cao, K-J Wang, J.S Chen*: Formation of CuS nanotube arrays from CuCl nanorods through a gas-solid reaction route*. J. Cryst. Growth 299, 386–392, 2007.

[54] H. Cao, X. Qian, C. Wang, X. Ma, J. Yin, and Z. Zhu: *High symmetric 18-facet polyhedron nanocrystals of Cu_7S_4 with a hollow nanocage*. J. Am. Chem. Soc. 127, 16024–16025, 2005.

[55] C. M. Wanga, D. R. Baer, L. E. Thomas, and J. E. Amonette.: *Void formation during early stages of passivation: Initial oxidation of iron nanoparticles at room temperature*. J. Appl. Phys. 98, 094307–094308, 2005.

[56] A. Cabot, V. F. Puntes, E. Shevchenko, Y. Yin, L. Balcells, M. A. Marcus, S. M. Hughes, and A. P Alivisatos: *Vacancy coalescence during oxidation of iron nanoparticles*. J. Am. Chem. Soc. 129, 10358–10360, 2007.

[57] S. Fusco, G. Chatzipirpiridis, K. M. Sivaraman, O. Ergeneman, B. J. Nelson, and S. Pané: *Chitosan electrodeposition for microrobotic drug delivery*, Adv. Healthcare Mater., 2, 7, 1037–1044, 2013.

[58] G. Chatzipirpiridis, E. Avilla, O. Ergeneman, S. Pané: *Electroforming of Magnetic Microtubes for Microrobotic Applications*, IEEE transactions on magnetics, 50, 11, 2014**.**

[59] K. M. Sivaraman, C. Kellenberger, S. Pané, O. Ergeneman T. Lühmann, N. A. Luechinger, H. Hall, W.J. Stark, B.J. Nelson: *Porous polysulfone coatings for enhanced drug delivery.* Biomed Microdevices, 14, 603–612, 2012.

[60] X. Wang, G. Yu, X. Han, H. Zhang, J. Ren, X. Wu and Y. Qu : *Biodegradable and Multifunctional Polymer Micro-Tubes for Targeting Photothermal Therapy*, *Int. J. Mol. Sci*., 15, 11730-11741, 2014.

[61] K. Sangwon, Q. Famin, K. Samhwan, A. Ghanbari, C. Moon, L. Zhang, J. Bradley, and C. Hongsoo, *Fabrication and Characterization of Magnetic Microrobots for Three-Dimensional Cell Culture and Targeted Transportation*, Adv. Mater., 25, 5863, 2013**.**

[62] H. Hashimotoa, S. Yokoyamab, H. Asaokaa, Y. Kusanoc, Y. Ikedad, M. Senoe, J. Takadaa,, T. Fujiia, M. Nakanishia, R. Murakamib: *Characteristics of hollow microtubes consisting of amorphous iron oxide nanoparticles produced by iron oxidizing bacteria, Leptothrix ochracea*, Journal of Magnetism and Magnetic Materials, 310, 2405–2407, 2007.

[63] G. S. Parkinson: *Iron Oxide Surfaces*, Surface Science Reports, 71, 272-365, 2016**.**

[64] D. Jariwala, V.K Sangwan, L.J Lauhon, T.J Marks and M.C Hersam *Emerging device applications for semiconducting two-dimensional transition metal dichalcogenides*, ACS Nano, 8, 1102, 2014.

[65] S. Kabouchea, B. Bellalb, Y. Louafia and M. Trarib: *Synthesis and semiconducting properties of tin(II) sulfide: Application to photocatalytic degradation of Rhodamine B under sun light*, Materials Chemistry and Physics, 195, 229-235, 2017**.**

[66] S. F. Wang, W. Wang, W. K. Fong, Y. Yu & C. Surya, *Tin Compensation for the SnS Based Optoelectronic Devices*, Scientific Reports, 7, 39704, 2017.

[67] V. Steinmann, R. Jaramillo, K, Hartman, R, Chakraborty, R, E. Brandt, J, R. Poindexter, Y. S. Lee, L. Sun, A. Polizzotti, H. Park, R.G. Gordon, T. Buonassisi, *3.88% Efficient Tin Sulfide Solar Cells using Congruent Thermal Evaporation,* Advanced Materials, 26, 7488-7492, 2014.

[68] X. Zhou, L. Gan, Q. Zhang, X. Xiong, H. Li, Z. Zhong, J. Hana and T. Zhai, *High performance near-infrared photodetectors based on ultrathin SnS nanobelts grown via physical vapor deposition,* J. Mater. Chem. C,4, 2111-2116, 2016.

[69] P. Sinsermsuksakul, J. Heo , W. Noh, A.S Hock, and R.G Gordon, *Atomic Layer Deposition of Tin Monosulfi de Thin Films,* Adv. Energy Mater., 1, 1116–1125, 2011.

[70] D. Koktysh, J. McBride, S. Rosenthal, *Synthesis of SnS nanocrystals by the solvothermal decomposition of a single source precursor*, Nanoscale Res Lett., 2, 144–148, 2007.

[71] A. Tanusevski, *Optical and photoelectric properties of SnS thin films prepared by chemical bath deposition*, Semiconductor Science and Technology, 18, 6, 2003.

[72] M. Ichimuraa, K. Takeuchib, Y. Onob, E. Araib, *Electrochemical deposition of SnS thin films, Thin Solid Films*, 21, 98-101, 2000.

[73] Q. Zhai, J. Li, J.S. Lewis, K.A. Waldrip, K. Jones, P.H. Holloway, M. Davidson, N. Evans, *Microstructure and electroluminescence of ZnS:Mn doped with KCl*, Thin Sold Films 414, 105-112, 2002.

[74] Y.W Wang, L.D Zhang, C.H Liang, G.Z Wang, X.S Peng, *Catalytic growth and photoluminescence properties of semiconductor single-crystal ZnS nanowires*. Chem. Phys. Lett., 357, 314–318, 2002.

[75] J. Iang Y, X.M Meng, J. Liu, Z. R Hong, C.S Lee, S.T Lee, *ZnS nanowires with wurtzite polytype modulated structure*. Adv. Mater;15:1195–1198, 2003.

[76] K. Manzoor, V. Aditya, S.R Vadera, N. Kumar, T.R.N Kutty, *Enhanced electroluminescence properties of doped ZnS nanorods formed by the self-assembly of colloidal nanocrystals*, Solid State Commun.,135, 16–20, 2005.

[77] Z.G Chen, J. Zou, G.Q Lu, G. Liu, F. Li, H.M Cheng, *ZnS nanowires and their coaxial lateral nanowire heterostructures with BN*, App.l Phys. Lett.,90, 103117, 2007.

[78] Q. Li and C. Wang, *Fabrication of wurtzite ZnS nanobelts via simple thermal evaporation*, Appl. Phys. Lett. 83, 359, 2003.

[79] F. Qian, S. Gradecak, Y. Li, C.-Y. Wen and C. M. Lieber, *Core/Multishell Nanowire Heterostructures as Multicolor, High-Efficiency Light-Emitting Diodes*, Nanoletters 5, 2287, 2005.

[80] Y. Huang, X. Duan and C. M. Lieber, *Nanowires for Integrated Multicolor Nanophotonics*, Small, 1, 142, 2005.

[81] S. Blundell Magnetism in Condensed Matter, , Department of Physics, University of Oxford. Oxford University Press Inc., New York, 2001.

[82] D. Jiles, *Introduction to Magnetism and Magnetic Materials*, Second edition Laboratory, US Department of Energy.

[83] C. Wu, P. Yin, X. Zhu, C.O Yang, and Y. Xie, *Synthesis of Hematite (α-Fe2O3) Nanorods: Diameter-Size and Shape Effects on Their Applications in Magnetism, Lithium Ion Battery, and Gas Sensors*, J. Phys. Chem. B, 110, 17806–17812, 2006.

[84] S. Lian, E. Wang, L. Gao, Z. Kang, D. Wu, Y. Lan, L. Xu: *Growth of single-crystal magnetite nanowires from Fe_3O_4 nanoparticles in a surfactant-free hydrothermal process*, Solid State Communications, 132, 375-378, 2004.

[85] J. Lee: *Gas sensors using hierarchical and hollow oxide nanostructures: Overview,* Sensors and Actuators B, 140, 319–336, 2009.

[86] J. Chen, L. Xu, W. Li, X. Gou, *Fe_2O_3 Nanotubes in gas sensor and lithium-ion battery applications*, Adv Mater, 17,582–586, 2005.

[87] P. Hiralal, H. Unalan, K.G UWijayantha, A. Kursumovic, D. Jefferson, J.L MacManus-Driscoll and G.A Amaratunga: *Growth and process conditions of aligned and patternable films of iron(III) oxide nanowires by thermal oxidation of iron*, Nanotechnology, 19, 455608, 2008.

[88] K. Tai1, K. Sun, B. Huang and S. J Dillon: *Catalyzed oxidation for nanowire growth,* Nanotechnology, 25,145603, 2014.

[89] S.H Yu, Q-Z Yao, G.T Zhou, S.Q Fu: *Preparation of Hollow Core/Shell Microspheres of Hematite and Its Adsorption Ability for Samarium*, Appl. Mater. Interfaces, 6, 10556−10565, 2014.

[90] M. Tadic, D. Markovic, V. Spasojevic, V. Kusigerski, M. Remškar, J. Pirnat, Z. Janglicic: *Synthesis and magnetic properties of concentrated Fe_2O_3 nanoparticles in a silica matrix,* J. Alloy. Comp, 441, 291-296, 2007.

[91] Handbook of Chemistry and Physics, 98th Edition, CRC Press, 2017.

[92] D. L. Huber: *Synthesis, Properties, and Applications of Iron Nanoparticles*, Small, 5, 482 – 501, 2005.

[93] Y. Mei, Z. Zhou, and H. L. Luo: *Electrical resistivity of rf ‐ sputtered iron oxide thin films*, Journal of Applied Physics, 61, 4388, 1987.

[94] B. A. Calhoun, *Magnetic and Electric Properties of Magnetite at Low Temperatures*, Phys. Rev., 94, 1577, 1954.

[95] N Birks, GH Meier, FS Pettit, *Introduction to the high-temperature oxidation of metals*, Cambridge University Press, 2006.

[96] G.W Simmons, D.J. Dwyer, *A LEED-AES study of the initial stages of oxidation of Fe (001),* Surface Science, 48, 373-392, 1975.

[97] J. Mercier, G. Zambelli, W. Kurz, *Introduction to Materials Science*, Elsevier Science, 2003.

[98] S. Dutta, S.K. Manik, M. Pal, S.K. Pradhan, P. Brahma, D. Chakravorty, *Electrical conductivity in nanostructured magnetite–hematite composites produced by mechanical milling*, Journal of Magnetism and Magnetic Materials 288, 301–306, 2005.

[99] Y. Mei, Z.J Zhou, and H. L. Luo: *Electrical resistivity of rf - sputtered iron oxide thin films*, Journal of Applied Physics, 61, 4388, 1987.

[100] A. E Cubillo, J.M Tulliani, C. Pecharromán, J.S Moya, *Iron-oxide nanoparticles supported on sepiolite as a novel humidity sensor*, Journal of the European Ceramic Society, 27, 1983-1989, 2007.

[101] P. Chauhan, S.Annapoorni, S.K Trikha, *Humidity-sensing properties of nanocrystalline haematite thin films prepared by sol-gel processing*, Thin Solid Films, 346, 266-268, 1999.

[102] K. Hoshino, B. Yeh, J. F. Wager, *Impact of humidity on the electrical performance of amorphous oxide semiconductor thin- film transistors*, Journal of the Society for Information Display, 21, 310-316, 2013.

[103] A. S. Khanna, *Introduction to High Temperature Oxidation and Corrosion*, ASM International, 2002.

[104] Y. Li, Y. Yangy and X. Feng: *Influence of Electric Current on Kirkendall Diffusion of Zn/Cu Couples*, J. Mater. Sci. Technol.,24, 2008.

[105] E. O. Kirkendall, *Diffusion of zinc in alpha brass*, Trans. AIME, 147, 104, 1942**.**

[106] Abdel-Aziz El Mel, Ryusuke Nakamura, and Carla Bittencourt: *The Kirkendall effect and nanoscience: hollow nanospheres and nanotubes*, Beilstein J. Nanotechnol., 6, 1348–1361, 2015.

[107] C.M. Wang, D.R. Baer, L.E. Thomas, and J.E. Amonette: *Void formation during early stages of passivation: Initial oxidation of iron nanoparticles at room temperature*, Journal of Applied Physics 98, 094308, 2005.

[108] R. Nakamura and H. Nakajima: *Application of the Kirkendall Effect to Morphology Control of Nanowires: Morphology Change from Metal Nanowires to Oxide Nanotubes*, Book: Nanowires - Implementations and Applications, Institute of Scientific and Industrial Research, Osaka University Japan, 2011.

[109] J. Kucera, *Analysis of magnetic anomaly in bcc iron*, Czech. J. Phys. B, 29, 797-808, 1979.

[110] M. Lubbehusen, H. Mehrer, *Self-diffusion in α-iron: the influence of dislocations and the effect of the magnetic phase transition,* Acta Metall. Mater. 38, 283, 1990.

[111] Y. Iijima, K. Kimura, K. Hirano, *Self-diffusion and isotope effect in α-iron*, Acta Metall. 36, 2811, 1988.

[112] F.S. Buffington, K.I. Hirano, M. Cohen, Self diffusion in iron Acta Metall. 9, 434, 1961.

[113] C.M. Walter, N.L. *Peterson, Isotope effect in self-diffusion in iron*, Phys. Rev. 178, 922, 1969.

[114] P. K. Gallagher, E. M. Gyorgy, and H. E. Bair, *An anomaly in the oxidation rate of magnetite at its Curie temperature*, The Journal of Chemical Physics, 71, 830-835, 1979**.**

[115] L Girifalco, *Activation energy for diffusion in ferromagnetics*, Journal of Physics and Chemistry of Solids, 23, 1171-1173, 1962**.**

[116] J. Yang and J.I. Goldstein, *Magnetic Contribution to the Interdiffusion Coefficients in Bcc (α) and Fcc (γ) Fe-Ni Alloys*, Metallurgical and materials transactions A, 35, 1681, 2004.

[117] B. Sundman, *An assessment of the Fe-O system*, J. Phase Equilibria, 12, 127, 1991.

[118] A.G. Nasibulin, S. Rackauskas, H. Jiang, Y. Tian, P. Reddy Mudimela, S.D. Shandakov, L. Nasibulina, J. Sainio, and E. I. Kauppinen: *Simple and rapid synthesis of α-Fe2O3 nanowires under ambient conditions*, Nano Res., 2, 373-379, 2009.

[119] T.L Cheng, and Y.H Wen: *Toward a Quantitative Understanding of the Electric Field in Thermal Metal Oxidation and a Self-Consistent Wagner Theory*, J. Phys. Chem. Lett., 5, 2289–2294, 2014**.**

[120] A. Jubb, H. Allen: *Vibrational Spectroscopic Characterization of Hematite, Maghemite, and*

Magnetite Thin Films Produced by Vapor Deposition, ACS Appl. Mater. Interfaces, 2, 2804, 2010.

[121] W. Feitknecht, K.J. Gallagher: *Mechanisms for the Oxidation of Fe_3O_4*, Nature, 548–549, 197, 1970.

[122] O. N. Shebanova, P. Lazor, *Raman study of magnetite (Fe_3O_4): laser-induced thermal effects and oxidation*, Journal of Raman Spectroscopy, 34, 845, 2003.

[123] D. Bersani, P. P. Lottic, Xing-Zhao Ding: *Phonon confinement effects in the Raman scattering by TiO2 nanocrystals*, Appl. Phys. Lett, , 72, 73, 1998.

[124] V. Swamy: *Size-dependent modifications of the first-order Raman spectra of nanostructured rutile TiO_2,* Physical Review B, 77, 195414, 2008.

[125] V. Swamy, B. Muddle, Q. Dai: *Size-dependent modifications of the Raman spectrum of rutile TiO_2*, Applied Physics Letters, 89, 3118, 2006.

[126] K.W. Adu, H.R. Gutiérrez, U.J Kim, G.U Sumanasekera, and P.C Eklund, *Confined Phonons in Si Nanowires*, Nano Letters, 5, 409, 2005.

[127] D. Caplan and M. Cohen: *Effect of cold work on the oxidation of iron from 400-650 °C*, Corrosion Science, 6, 321-335, 1966.

[128] S. Lian, E. Wang, L. Gao, Z. Kang, D. Wu, Y. Lan, L. Xu: *Growth of single-crystal magnetite nanowires from Fe_3O_4 nanoparticles in a surfactant-free hydrothermal process*, Solid State Communications, 132, 375–378, 2004.

[129] W. Friedrich, *The Verwey transition - a topical review*, J. Phys. Condens Matter, 14, 285–340, 2002.

[130] R.N. Bhowmik and A. Saravanan, *Surface magnetism, Morin transition, and magnetic dynamics in antiferromagnetic α-Fe_2O_3 (hematite) nanograins,* J. Appl. Phys., 107, 053916-053926, 2010.

[131] F. Ullrich, C. Bergeles, J. Pokki, O. Ergeneman, S. Erni, G. Chatzipirpiridis, S. Pané, C. Framme, B.J Nelson: *Mobility Experiments With Microrobots for Minimally Invasive Intraocular*, Invest. Ophthalmology Vis. Sci., 54, 2853–2863, 2013.

[132] G. Chatzipirpiridis, E. Avilla, O. Ergeneman, S. Pané: *Electroforming of Magnetic Microtubes for Microrobotic Applications*, IEEE transactions on magnetics, 50, 11, 2014.

[133] K. Sangwon, Q. Famin, K. Samhwan, A. Ghanbari, C. Moon, L. Zhang, J. Bradley, and C. Hongsoo: *Fabrication and Characterization of Magnetic Microrobots for Three-Dimensional Cell Culture and Targeted Transportation*, Adv. Mater., 25, 5863, 2013.

[134] B. D. Cullity, *Elements of X-Ray Diffraction*, Massachusetts, Addison-/Wesley publishing company, 1978.

[135] S.Sohilaa, M.Rajalakshmi, C.Ghosh, A.K.Arorab, C.Muthamizhchelvan, *Optical and Raman scattering studies on SnS nanoparticles*, Journal of Alloys and Compounds, 509,5843-5847, 2011.

[136] P.M Nikolic, P. Mihajlovic and B. Lavrencic, *Splitting and coupling of lattice modes in the layer compound SnS*, Journal of Physics C: Solid State Physics, 10, L289, 1977.

[137] Y. C. Cheng, C. Q. Jin, F. Gao, X. L. Wu, W. Zhong, S. H. Li and P.K. Chu, *Raman scattering study of zinc blende and wurtzite ZnS*, Journal of applied physics, 106, 1-123505, 2009.

[138] D. C. Agrawal and V. J. Menon: *Surface tension and evaporation: An empirical relation for water*, Physical Review A, 46, 2166-2169, 1992.

[139] K. Nogi, K. Ogino, A. Mclean, and W. A. Miller, *The Temperature Coefficient of the Surface Tension of Pure Liquid Metals*, Metallurgical Transactions B, 17, 163-170, 1986.

[140] Y.C Liang and H. Zhong, *Self-catalytic crystal growth, formation mechanism, and optical properties of indium tin oxide nanostructures*, Nanoscale Research Letters, 8, 358-364, 2013.

[141] P. Praus, L. Svoboda, J. Tokarsky, A. Hospodkova, V. Klemn, *Core/shell CdS/ZnS nanoparticles: Molecular modelling and characterization by photocatalytic decomposition of Methylene Blue*. Appl. Surf. Sci., 292, 813–822, 2014.

[142] P.K Bankar, S. Warule, S.R Jadkar, N.S Chaudhari and M.A More: *Nanostructured BiOI-GO composite: facile room temperature synthesis with enhanced multifunctionality in field emission and photocatalytic activity,* RSC Advances, 6 , 83084-83090, 2016.

[143] S.B Kokane, S.R Suryawanshi, R. Sasikala, M.A. More, S.D. Sartale: *Architecture of 3D $ZnCo_2O_4$ marigold flowers: Influence of annealing on cold emission and photocatalytic behavior,* Materials Chemistry and Physics, 194, 55-64, 2017.

[144] A. Houas, H. Lchheb, M. Ksibi, E. Elaloui, C. Guillard, J.-M. Herrmann: *Photocatalytic degradation pathway of methylene blue in water.* Appl. Catal. B Environ., 31, 145–157, 2001.

[145] H. Rao, Z. Lu, X. Liu, H. Ge, Z. Zhang, P. Zou, H. Heb and Y. Wang, *Visible light-driven photocatalytic degradation performance for methylene blue with different multi-morphological features of ZnS*. RSC Adv., 6, 46299, 2016.

[146] N. Soltani, E. Saion, M. Z Hussein, M. Erfani, A. Abedini, G. Bahmanrokh, M. Navasery and P. Vaziri, *Visible Light-Induced Degradation of Methylene Blue in the Presence of Photocatalytic ZnS and CdS Nanoparticles*. Int. J. Mol. Sci., 13, 12242-12258, 2012.

[147] N. Soltani, E. Saion, W. M Yunus, M. Navasery, G. Bahmanrokh, M. Erfani, M. R Zare, E. Gharibshahi, *Photocatalytic degradation of methylene blue under visible light using PVP-capped ZnS and CdS nanoparticles*, Solar Energy, 97, 147–154, 2013.

[148] F. Jamali-Sheini, R.Yousefi, N. Bakr, M. Cheraghizade, M. Sookhakian, N. Huang, *Highly efficient photo-degradation of methyl blue and band gap shift of SnS nanoparticles under different sonication frequencies*, Materials Science in Semiconductor Processing, 32, 172–178, 2015.

[149] A. J. Biacchi, D. Vaughn, and R. E. Schaak: *Synthesis and Crystallographic Analysis of Shape-Controlled SnS Nanocrystal Photocatalysts: Evidence for a Pseudotetragonal Structural Modification*. J. Am. Chem. Soc., 135, 11634−11644, 2013.

[150] J. Chao, Z. Wang, X. Xu, Q. Xiang, W. Song, G. Chen, J. Hu and D. Chen: *Tin sulfide nanoribbons as high performance photoelectrochemical cells, flexible photodetectors and visible-light-driven photocatalysts*. RSC Adv., 3, 2746–2753, 2013.

[151] J.H Li, A.H. Lu, F. Liu, L.Z Fan, *Synthesis of ZnS/dravite composite and its photocatalytic activity on degradation of methylene blue*. Solid State Ionics, 179, 1387–1390, 2008.

[152] D. Denzler, M. Olschewski, K. Sattler, *Luminescence studies of localized gap states in colloidal ZnS nanocrystals.* Journal of Applied Physics, 84, 2841–2845, 1998.

[153] J. Dai, X. Song, H. Zheng, C. Wu, *Excitonic photoluminescence and photoresponse of ZnS*

nanowires. Materials Chemistry and Physics, 174, 204–208, 2016**.**

[154] J. Henry, K. Mohanraj, S. Kannan, S. Barathan, G. Sivakumar, *Structural and optical properties of SnS nanoparticles and electron-beam-evaporated SnS thin films*, Journal of Experimental Nanoscience, 10, 78-85, 2015.